UNIVERSITÀ DELLA CALABRIA

UNIVERSITÀ DELLA CALABRIA

Dipartimento di Fisica

Dottorato di Ricerca in

Scienze e Tecnologie Fisiche, Chimiche e dei Materiali, in convenzione con il CNR

XXXI CICLO

A comparative study of reconstruction methods for Neutron Tomography

Settore Scientifico Disciplinare FIS/07

Coordinatore: Ch.mo Prof. Vincenzo Carbone

Firma oscurata in base alle linee guida del Garante della privacy

Supervisore: Ch.mo Prof. Giuseppe Gorini

Firma oscurata in base alle linee guida del Garante della privacy

Tutor: Dott. Triestino Minniti

Firma oscurata in base alle linee guida del Garante della privacy

Ch.mo Prof. Enrico Tassi

Firma oscurata in base alle linee guida del Garante della privacy

Dottorando: Dott. Davide Micieli

Firma oscurata in base alle linee guida del Garante della privacy

This thesis is dedicated to the memory of my father

Abstract

Neutron tomography is a well established technique to non-destructively investigate the inner structure of a wide range of objects. The main disadvantages of this technique are the time-consuming data acquisition, which generally requires several hours, and the low signal to noise ratio of the acquired images. One way for decreasing the total scan time is to reduce the number of radiographs. However, the *Filtered Back-Projection*, which is the most widely used reconstruction method in neutron tomography, generates low quality images affected by artifacts when the number of projections is limited or the signal to noise ratio of the radiographs is low.

This doctoral thesis is focused on the comparative analysis of different reconstruction techniques, aimed at finding the data processing procedures suitable for neutron tomography that shorten the scan time without reduction of the reconstructed image quality.

At first the performance of the algebraic reconstruction methods were tested using experimental neutron data and studied as a function of the number of projections and for different setups of the imaging system. The reconstructed images were quantitatively compared in terms of image quality indexes.

Subsequently, the recently introduced *Neural Network Filtered Back-Projection* method was proposed in order to reduce the acquisition time during a neutron tomography experiment. This is the first study which proposes and tests a machine learning based reconstruction method for neutron tomography. The *Neural Network Filtered Back-Projection* method was quantitatively compared to conventional reconstruction algorithms used in neutron tomography.

Finally, we present `NeuTomPy`, a new Python package for tomographic data processing and reconstruction. `NeuTomPy` is a cross-platform toolbox ready to work with neutron data. The first release of `NeuTomPy` includes pre-processing algorithms, a wide range of classical and state-of-the-art reconstruction methods and several image quality indexes, in order to evaluate the reconstruction quality. This software is free and open-source, hence researchers can freely use it and contribute to the project.

Sommario

La tomografia a neutroni è una tecnica ben consolidata per analizzare in maniera non distruttiva la struttura interna di una vasta gamma di oggetti. Gli svantaggi maggiori di questa tecnica sono la lenta acquisizione dati, che generalmente richiede diverse ore, e il basso rapporto segnale-rumore delle immagini acquisite. Un modo per ridurre il tempo totale di una scansione tomografica è quello di limitare il numero di radiografie da acquisire. Tuttavia l'algoritmo *Filtered Back-Projection*, ossia il metodo di ricostruzione maggiormente utilizzato in tomografia a neutroni, produce delle immagini di bassa qualità e affette da artefatti se il numero di proiezioni è limitato oppure se le radiografie sono caratterizzate da un basso rapporto segnale-rumore.

Questa tesi di dottorato è incentrata sull'analisi comparativa di diversi algoritmi di ricostruzione tomografica ed è finalizzata a determinare le procedure di elaborazione dati per la tomografia a neutroni che consentono di ridurre i tempi di acquisizione, ma senza compromettere la qualità delle immagini ricostruite.

In primo luogo, le performance dei metodi di ricostruzione algebrici sono state testate utilizzando dati sperimentali e studiate in funzione del numero di radiografie e per diversi setup del sistema di imaging. Le immagini ricostruite sono state comparate in maniera quantitativa utilizzando delle metriche di qualità delle immagini.

Successivamente, il recente metodo di ricostruzione *Neural Network Filtered Back-Projection* è stato proposto per accelerare i tempi di acquisizione degli esperimenti di tomografia a neutroni. Per la prima volta viene proposto e testato un metodo basato sul machine learning per la ricostruzione di dati acquisiti con tomografia a neutroni. Il metodo *Neural Network Filtered Back-Projection* è stato comparato in maniera quantitativa con algoritmi di ricostruzione comunemente utilizzati.

Infine presentiamo `NeuTomPy`, un nuovo pacchetto Python per l'elaborazione e ricostruzione di dati tomografici. `NeuTomPy` è un toolbox multi-piattaforma ed è predisposto per elaborare dati acquisiti mediante tomografia a neutroni. Il primo rilascio di `NeuTomPy` include algoritmi di pre-processing, una vasta gamma di metodi di ricostruzione classici e allo stato dell'arte, e alcune metriche di qualità delle immagini per valutare la qualità delle ricostruzioni. Questo software è open-source ed è rilasciato gratuitamente, pertanto i ricercatori possono liberamente utilizzarlo e sono invitati a contribuire al progetto.

List of publications

- Publications that are part of this thesis:

[1] **D. Micieli**, T. Minniti, and G. Gorini. "NeuTomPy toolbox, a Python package for tomographic data processing and reconstruction". In: *SoftwareX* 9 (Mar. 2019), pp. 260–264. DOI: 10.1016/j.softx.2019.01.005.

[2] **D. Micieli**, T. Minniti, Ll. Marc Evans, and G. Gorini. "Accelerating Neutron Tomography experiments through Artificial Neural Network based reconstruction". In: *Scientific Reports* 9 (Feb. 2019). DOI: 10.1038/s41598-019-38903-1.

[3] **D. Micieli**, T. Minniti, V. Formoso, W. Kockelmann, and G. Gorini. "A comparative study of reconstruction methods applied to Neutron Tomography". In: *Journal of Instrumentation* 13.06 (June 2018), p. C06006. DOI: 10.1088/1748-0221/13/06/c06006.

- Publications on the subject of Imaging that are not part of this thesis:

[1] **D. Micieli**, D. Di Martino, M. Musa, L. Gori, A. Kaestner, A. Bravin, A. Mittone, R. Navone, and G. Gorini. "Characterizing pearls structures using X-ray phase-contrast and neutron imaging: a pilot study". In: *Scientific Reports* 8.1 (Aug. 2018). DOI: 10.1038/s41598-018-30545-z.

[2] G. Vitucci, T. Minniti, D. Di Martino, M. Musa, L. Gori, **D. Micieli**, W. Kockelmann, K. Watanabe, A.S. Tremsin, and G. Gorini. "Energy-resolved neutron tomography of an unconventional cultured pearl at a pulsed spallation source using a microchannel plate camera". In: *Microchemical Journal* 137 (Mar. 2018), pp. 473–479. DOI: 10.1016/j.microc.2017.12.002.

[3] C. Andreani, F. Aliotta, L. Arcidiacono, M. Borla, D. Di Martino, F. Facchetti, E. Ferraris, G. Festa, G. Gorini, W. Kockelmann, J. Kelleher, D. Malfitana, **D. Micieli**, T. Minniti, E. Perelli Cippo, R. Ponterio, G. Salvato, R. Senesi, V. Turina, C. Vasi, and C. Greco. "A neutron study of sealed pottery from the grave-goods of Kha and Merit". In: *Journal of Analytical Atomic Spectrometry* 32.7 (2017), pp. 1342–1347. DOI: 10.1039/c7ja00099e.

[4] W. Kockelmann, T. Minniti, D. Pooley, G. Burca, R. Ramadhan, F. Akeroyd, G. Howells, C. Moreton-Smith, D. Keymer, J. Kelleher, S. Kabra, T. Lee, R. Ziesche, A. Reid, G. Vitucci, G. Gorini, **D. Micieli**, R. Agostino, V. Formoso, F. Aliotta, R. Ponterio, S. Trusso, G. Salvato, C. Vasi, F. Grazzi, K. Watanabe, J. Lee, A. Tremsin, J. McPhate, D. Nixon, N. Draper, W. Halcrow, and J. Nightingale. "Time-of-Flight Neutron Imaging on IMAT@ISIS: A New User Facility for Materials Science". In: *Journal of Imaging* 4.3 (Feb. 2018), p. 47. DOI: 10.3390/jimaging4030047.

- Publications on other topics that are not part of this thesis:

[1] **D. Micieli**, I. Drebot, E. Milotti, V. Petrillo, E. Tassi, and L. Serafini. "Matter from light-light scattering via Breit-Wheeler events produced by two interacting Compton sources". In: *Phys. Rev. Accel. Beams* 20 (4 Apr. 2017), p. 043402. DOI: 10.1103/PhysRevAccelBeams.20.043402.

[2] **D. Micieli**, I. Drebot, A. Bacci, E. Milotti, V. Petrillo, M. Rossetti Conti, A. R. Rossi, E. Tassi, and L. Serafini. "Compton sources for the observation of elastic photon-photon scattering events". In: *Phys. Rev. Accel. Beams* 19 (9 Sept. 2016), p. 093401. DOI: 10.1103/PhysRevAccelBeams.19.093401.

[3] I. Drebot, **D. Micieli**, V. Petrillo, E. Tassi, and L. Serafini. "ROSE: A numerical tool for the study of scattering events between photons and charged particles". In: *Nuclear Instruments and Methods in Physics Research Section B: Beam Interactions with Materials and Atoms* 402 (2017). Proceedings of the 7th International Conference Channeling 2016: Charged & Neutral Particles Channeling Phenomena, pp. 376–379. DOI: 10.1016/j.nimb.2017.02.076.

[4] I. Drebot, A. Bacci, **D. Micieli**, E. Milotti, V. Petrillo, M. Rossetti Conti, A.R. Rossi, E. Tassi, and L. Serafini. "Study of photon–photon scattering events". In: *Nuclear Instruments and Methods in Physics Research Section A: Accelerators, Spectrometers, Detectors and Associated Equipment* 865 (2017). Physics and Applications of High Brightness Beams 2016, pp. 9–12. DOI: 10.1016/j.nima.2016.07.039.

Contents

List of Figures

List of Abbreviations

ANN . . . . . . Artificial Neural Network
ART . . . . Algebraic Reconstruction Technique
BP . . . . Back Projection
CCD . . . . . . Charge-Coupled Device
CG . . . . Conjugate Gradient
CGLS . . . . . . Conjugate Gradient Least Squares
CMOS . . . . . Complementary Metal-Oxide Semiconductor
CNN . . . . . . Convolutional Neural Network
CNR . . . . . . Contrast to Noise Ratio
COR . . . . . . Centre Of Rotation
CPU . . . . Central Processing Unit
CT . . . . Computed Tomography
DL . . . . Deep Learning
FBP . . . . Filtered Back Projection
FFT . . . . Fast Fourier Transform
FOV . . . . Field Of View
FSIM . . . . . . Feature Similarity Index
FT . . . . Fourier Transform
FWHM . . . . . Full Width at Half Maximum
GMSD . . . . . Gradient Magnitude Similarity Deviation
GPU . . . . . . Graphics Processing Unit
MCP . . . . . . Microchannel Plate
ML . . . . Machine Learning
NI . . . . Neutron Imaging
NRMSE . . . . Normalized Root Mean Square Error

NT . . . . Neutron Tomography

ROI . . . . Region Of Interest

SART . . . . . . Simultaneous Algebraic Reconstruction Technique

SIRT . . . . . . Simultaneous Iterative Reconstruction Technique

SSIM . . . . . . Structural SIMilarity (SSIM) index

TOF . . . . Time Of Flight

TV . . . . Total Variation

1D, 2D, 3D . . One-, two-, three-dimensional

Introduction

Neutron tomography is a well established imaging technique which provides the three-dimensional map of the neutron attenuation coefficients within an object. It consists in acquiring radiographs of a sample, irradiated using a neutron beam, for several view angles. The three-dimensional map of the neutron attenuation coefficients is computed from the acquired radiographs by means of a mathematical reconstruction algorithm. Generally, neutron imaging is particularly well suited to study thick metals, hydrogenous materials and porous media, hence found application in biology, agriculture, archaeology, materials science and engineering. Neutron imaging provides complementary information to X-ray techniques and, in some cases, gives incomparable results.

However, the major drawback of neutron tomography is the limited particle flux of the existing neutron sources, several orders of magnitude lower compared to synchrotron X-ray sources. It follows that long scan times - generally several hours, depending on the sample and the desired spatial resolution - are required to perform neutron tomographic scans and the acquired radiographs are typically characterised by low signal-to-noise ratio. One way for decreasing the total scan time is to reduce the number of radiographs. However, the *Filtered Back-Projection*, which is the most widely used reconstruction method in neutron tomography, generates low quality images affected by artifacts when the number of projections is limited or the signal-to-noise ratio of the radiographs is low.

This doctoral thesis is focused on the comparative analysis of different reconstruction techniques, aimed at finding the data processing procedures suitable for neutron tomography that shorten the scan time without reduction of the reconstructed image quality. The aim of this work is also deploy a software for tomographic data processing, suitable for neutron datasets, including a wide range of reconstruction methods and image quality metrics for the quantitative evaluation of the reconstruction quality.

Tomographic reconstruction methods can be divided into two categories: analytical and iterative. Analytical methods are based on a continuous model with the assumption that noise-free projections are available for all view angles. However, this is clearly not feasible in practice, hence analytical formulas are approximated by discretized expressions. Consequently, the analytical methods, of which *Filtered Back-Projection* is the most widely used example, provide accurate reconstructions if the number of projections is sufficiently large and the signal-to-noise ratio of the radiographs is sufficiently high. If these conditions are not satisfied, analytical methods generate low quality images affected by noise and artifacts. Nevertheless, such methods are widely used, since they are computationally inexpensive and easy to handle.

Iterative reconstruction methods, unlike analytical ones, are based on a discrete model of the reconstruction problem which can include prior knowledge concerning the sample or the imaging system. Consequently, iterative methods outperform analytical ones in terms of reconstructed image quality when under-sampled or noisy datasets are available. Iterative reconstruction methods can be divided into two classes: algebraic methods and statistical methods. Concerning the first category, the reconstruction problem is described by a linear system which is solved by means of an iterative algorithm. Statistical reconstruction algorithms are based on statistical models describing the data acquisition process, hence the image reconstruction is fulfilled by minimizing a loss function using an iterative algorithm. However, the computational cost of such methods is several orders of magnitude higher than analytical methods. With the advancement of computer technology, the computational capacities of current workstations can efficiently support iterative methods, which have become a viable and reliable tool for tomographic reconstruction, allowing a reduction of the radiation dose without any loss of the reconstructed image quality. Iterative methods play an important role in the clinical use of the X-ray tomography, the positron-emission tomography (PET) and the single-photon emission computed tomography (SPECT). Conversely, the adaptability of iterative methods to neutron tomography has not been fully studied, hence their application in this field is still limited. In this work, we quantitatively compare the main algebraic reconstruction methods and the *Filtered Back-Projection* method in terms of several image quality indexes. The performance of the algorithms were tested using experimental data and studied as a function of the number of radiographs and for different setups of the imaging system.

In the last few years, new methods based on machine learning were proposed for tomography in order to improve the quality of the reconstruction of under-sampled or noisy datasets. In fact, nowadays machine learning based techniques have reached state-of-the-art performance for several applications of the image processing, for example classification, segmentation, deconvolution and image denoising. Such techniques are promising alternatives to iterative reconstruction algorithms. In fact, machine learning based methods 'learn' from data relevant information, called *features*, unlike iterative reconstruction methods, which generally exploit prior knowledge moulded ad hoc for the specific task. In this work we propose the *Neural Network Filtered Back-Projection* method in order to shorten the acquisition time during a neutron tomography experiment. This is the first study which proposes and tests a machine learning based reconstruction method for neutron tomography. The *Neural Network Filtered Back-Projection* method was quantitatively compared to classical reconstruction algorithms in terms of reconstructed image quality and computation times.

Finally, we present `NeuTomPy`, a new Python package for tomographic data processing and reconstruction. This tool was developed in order to support the demand of users to have freeware software suitable for neutron datasets, allowing to perform and compare different reconstruction methods. The first release of `NeuTomPy` includes pre-processing algorithms, a wide range of classical and state-of-the-art reconstruction methods and several image quality indexes, in order to evaluate the reconstruction quality. This software is free and open-source, hence researchers can freely use it and contribute to the project.

This thesis is divided into six chapters.

In Chapter 1, after an historical overview of tomography, we give a detailed description of the underlying physical model and the mathematical formulation of the reconstruction problem. In particular, we focus our attention on the main analytical and algebraic reconstruction methods.

The Chapter 2 is an overview on the neutron imaging. Initially we remind the history of the technique, then we recall the fundamental physical properties of the neutron and the production and moderation mechanisms involved in neutron sources for imaging applications. Afterwards, we describe in detail the neutron tomography, focusing our attention on the instrumentation, the data acquisition, the image processing and the main issues of the technique. Finally, we present the IMAT beamline located at the ISIS pulsed neutron spallation source (UK), where the tomographic data analysed and discussed in this thesis were acquired.

In Chapter 3 we present a comparative study involving the main algebraic reconstruction methods, described in Chapter 1, and the *Filtered Back-Projection*. For this purpose, a phantom sample was analysed by means of neutron tomography at the IMAT beamline and the acquired experimental data were used to test the performances of the reconstruction methods as a function of the number of radiographs and for different setups of the imaging system. The reconstructed images were quantitatively compared in terms of image quality indexes and the benefits of algebraic methods for the limited datasets are discussed.

In Chapter 4 we describe the mathematical formulation of the *Neural Network Filtered Back-Projection* method and we present a comparative study involving such method and classical reconstruction algorithms. We compared the reconstruction techniques in terms of the image quality indexes and computation times, then we demonstrated that *Neural Network Filtered Back-Projection* method allows to reduce scan time, reconstruction time and data storage providing high image quality for sparse-view neutron tomography. Finally, we give an overview of the potential applications of such method in neutron tomography.

In Chapter 5 we present the new toolbox for tomographic data reconstruction called `NeuTomPy`, describing in detail the software architecture, the main functionalities and some usage examples.

In Chapter 6 we summarize general conclusions about the research work presented in this doctoral thesis.

Introduzione

La tomografia a neutroni è una tecnica di imaging ben consolidata in grado di fornire la mappa tridimensionale dei coefficienti di attenuazione dei neutroni all'interno di un oggetto. Tale tecnica consiste nell'irraggiare un campione con un fascio di neutroni acquisendo delle radiografie ad angolazioni diverse. La mappa tridimensionale dei coefficienti di attenuazione dei neutroni per i materiali all'interno del campione viene calcolata a partire dalle radiografie acquisite mediante un algoritmo matematico di ricostruzione. In generale, le tecniche di imaging a neutroni sono particolarmente adatte per analizzare metalli, materiali contenenti idrogeno e materiali porosi, pertanto sono numerose le applicazione in scienze dei materiali, ingegneria, biologia, agricoltura e archeologia. L'imaging a neutroni fornisce informazioni complementari alle tecniche a raggi X e, in alcuni casi, offre risultati incomparabili.

La problematica maggiore della tomografia a neutroni è il modesto flusso di particelle generato dalle moderne sorgenti di neutroni, il quale risulta essere diversi ordini di grandezza inferiore al flusso delle sorgenti di raggi X. Di conseguenza, l'acquisizione dati richiede molto tempo - generalmente diverse ore, a seconda del campione e della risoluzione spaziale desiderata - e le radiografie prodotte sono caratterizzate da un modesto rapporto segnale-rumore. Un modo per ridurre il tempo totale di una scansione tomografica è quello di limitare il numero di radiografie da acquisire. Tuttavia l'algoritmo *Filtered Back-Projection*, ossia il metodo di ricostruzione maggiormente utilizzato in tomografia a neutroni, produce delle immagini di bassa qualità e affette da artefatti se il numero di proiezioni è insufficiente oppure se il rapporto segnale-rumore delle radiografie risulta modesto.

Questa tesi di dottorato è incentrata sull'analisi comparativa di diverse tecniche di ricostruzione tomografica ed è finalizzata a determinare le procedure di elaborazione dati per la tomografia a neutroni che consentono di ridurre i tempi di acquisizione, ma senza compromettere la qualità delle immagini ricostruite. Questo lavoro comprende inoltre lo sviluppo di un software per l'elaborazione e ricostruzione dati, particolarmente adatto per dati di tomografia a neutroni, che include una vasta gamma di metodi di ricostruzione e le principali metriche di qualità delle immagini usate in tomografia per valutare quantitativamente la qualità delle ricostruzioni.

I metodi di ricostruzione tomografica vengono generalmente suddivisi in due categorie: metodi analitici e metodi iterativi. I primi sono basati su un modello continuo in cui si assume che radiografie non affette da rumore siano ottenibili per ogni angolazione. Poiché in pratica ciò non è realizzabile, le formule analitiche vengono approssimate da espressioni discretizzate. Per questo motivo, l'algoritmo *Filtered Back-Projection* e in generale gli altri metodi analitici producono ricostruzioni accurate solo se il numero di radiografie e il rapporto segnale-rumore sono sufficientemente elevati. Se queste condizioni non sono soddisfatte, i metodi analitici producono delle immagini affette da rumore e artefatti. Nonostante ciò, i metodi analitici sono largamente utilizzati, poiché sono molto efficienti dal punto di vista computazionale e semplici da utilizzare.

I metodi iterativi sono basati invece su un modello discreto, che può includere informazioni a priori del campione o del setup sperimentale, e pertanto sono più accurati dei metodi analitici nel ricostruire datasets incompleti o affetti da rumore. I metodi iterativi possono essere distinti in due classi: metodi algebrici e metodi statistici. Nel caso dei metodi algebrici, il problema tomografico si traduce nella risoluzione di un sistema lineare tramite un algoritmo iterativo. Invece, i metodi statistici sono basati su modelli statistici che descrivono il processo di acquisizione dati e la ricostruzione delle immagini avviene minimizzando una funzione di perdita mediante un algoritmo iterativo. Il costo computazionale di tali metodi è in generale diversi ordini di grandezza più alto dei metodi analitici. Grazie al progresso della tecnologia informatica, la capacità computazionale delle attuali workstations è abbastanza elevata da supportare gli algoritmi iterativi e li rende una valida alternativa ai metodi analitici, in grado di ridurre la dose di radiazione senza deteriorare la qualità delle immagini ricostruite. I metodi iterativi hanno assunto un ruolo importante nell'uso clinico della tomografia a raggi X, della tomografia a emissione di positroni (PET) e della tomografia a emissione di fotone singolo (SPECT). Invece l'adattabilità di tali metodi alla tomografia a neutroni non è stata studiata completamente e le applicazioni in questo campo sono rare. Pertanto in questo lavoro i principali algoritmi algebrici sono stati comparati quantitativamente utilizzando delle metriche di qualità delle immagini. Le performance degli algoritmi sono state testate utilizzando dati sperimentali e studiate in funzione del numero di radiografie e per diversi setup del sistema di imaging.

Negli ultimi anni, nuovi metodi per tomografia basati sul *machine learning* sono stati proposti per migliorare la qualità delle ricostruzioni di datasets incompleti o caratterizzati da basso rapporto segnale-rumore. Infatti, oggi le tecniche di *machine learning* hanno raggiunto performance allo stato dell'arte in molte applicazioni dell'elaborazione digitale delle immagini, per esempio nei problemi di classificazione, segmentazione, deconvoluzione e riduzione del rumore. Tali tecniche risultano molto promettenti anche per la tomografia e rappresentano una valida alternativa ai metodi di ricostruzione iterativi. Infatti, i metodi basati sul *machine learning* 'apprendono' automaticamente dai dati informazioni caratteristiche (*features*, in inglese), a differenza degli algoritmi di ricostruzione iterativi, in cui informazioni a priori vengono modellate appositamente per la specifica applicazione. In questo lavoro proponiamo il metodo di ricostruzione *Neural Network Filtered Back-Projection* per ridurre i tempi di acquisizione degli esperimenti di tomografia a neutroni. Per la prima volta viene proposto e testato un metodo basato sul *machine learning* per la ricostruzione di dati acquisiti con tomografia a neutroni. Il metodo *Neural Network Filtered Back-Projection* è stato comparato in maniera quantitativa con classici algoritmi di ricostruzione in termini di qualità delle immagini e di tempo computazionale.

Infine, presentiamo `NeuTomPy`, un nuovo pacchetto Python per l'elaborazione e ricostruzione di dati tomografici. Questo software è stato sviluppato per soddisfare la richiesta di programmi gratuiti e multi-piattaforma, adatti per tomografia a neutroni e in grado di eseguire e comparare diversi metodi di ricostruzione. Il primo rilascio di `NeuTomPy` include algoritmi di pre-processing, una vasta gamma di metodi di ricostruzione classici e allo stato dell'arte, e alcune metriche di qualità delle immagini, per valutare la qualità delle ricostruzioni. Questo software è open-source ed è rilasciato gratuitamente, pertanto i ricercatori possono liberamente utilizzarlo e sono invitati a contribuire al progetto.

Questa tesi si articola in sei capitoli.

Nel Capitolo 1, dopo aver ripercorso i principali momenti storici della tomografia, descriviamo in dettaglio le basi fisiche e matematiche della tecnica. In particolare, concentreremo l'attenzione sui principali algoritmi di ricostruzione analitici e algebrici.

Il Capitolo 2 è dedicato all'imaging a neutroni. Dopo aver ricordato la storia della tecnica, richiamiamo brevemente le proprietà fisiche fondamentali dei neutroni e i meccanismi di produzione e moderazione utilizzati nelle sorgenti di neutroni per applicazioni di imaging. Successivamente presentiamo la tomografia a neutroni, descrivendo in dettaglio la strumentazione, l'acquisizione dati, l'elaborazione delle immagini e le principali problematiche della tecnica. Infine descriviamo la beamline IMAT situata presso la sorgente di neutroni ISIS (Regno Unito), una nuovo laboratorio dedicato all'imaging a neutroni dove sono stati acquisiti i dati sperimentali presentati in questa tesi.

Nel Capitolo 3 presentiamo uno studio comparativo degli algoritmi di ricostruzione algebrici, descritti nel Capitolo 1, e del metodo *Filtered Back-Projection*. A tale scopo un fantoccio è stato scansionato tramite tomografia a neutroni presso la beamline IMAT e i dati sperimentali sono stati utilizzati per testare gli algoritmi di ricostruzione in funzione del numero di radiografie e per diversi setup del sistema di acquisizione. Le immagini ricostruite sono state comparate quantitativamente utilizzando delle metriche di qualità delle immagini e i vantaggi dei metodi algebrici per la tomografia a neutroni sono stati discussi.

Nel Capitolo 4 descriviamo le basi matematiche del metodo di ricostruzione *Neural Network Filtered Back-Projection* e presentiamo uno studio comparativo che coinvolge tale metodo e gli algoritmi di ricostruzione classici. Dopo aver confrontato le tecniche in termini di qualità delle immagini e tempo computazionale, noi dimostriamo che il metodo *Neural Network Filtered Back-Projection* consente di ridurre i tempi di scansione e produce, in tempi più brevi rispetto agli algoritmi iterativi, ricostruzioni di buona qualità per datasets incompleti. Infine, mostriamo una panoramica sulle possibili applicazioni della tecnica in tomografia a neutroni.

Nel Capitolo 5 presentiamo il nuovo software per ricostruzione tomografica `NeuTomPy`, mostrandone l'architettura, le principali funzionalità e alcuni esempi di utilizzo.

Nel Capitolo 6 riassumiamo le conclusioni del lavoro di ricerca presentato in questa tesi di dottorato.

Young man, in mathematics you don't understand things.
You just get used to them.

— John von Neumann

1 Computed Tomography

Contents

In this chapter, we give an introduction to tomography. We cover the main historical developments of the technique, the underlying physical model and the mathematical formulation of the reconstruction problem. We describe the two main categories of CT reconstruction techniques: analytical and algebraic methods. Finally, we present a theoretical description of several standard reconstruction methods.

1.1 Introduction and historical overview

Computed Tomography (CT) is a powerful non-destructive imaging technique to visualize the inner structure of an objects. CT consists in collecting transmission or reflection data by irradiating an object from different directions with a kind of penetrating radiation probe. Fundamentally, the tomographic imaging problem relies on reconstructing an image from its *projections*, i.e. line integrals of the image evaluated for certain directions. The CT reconstruction task is performed through a computer implementation of a mathematical reconstruction algorithm. The X-ray CT has revolutionized the diagnostic medicine, since it has allowed doctors to visualize the internal organs. However, CT is widely used in several fields, such as astrophysics, archaeology, geophysics, material science and biology.

This thesis focuses on transmission Neutron Tomography (NT), where neutrons are used as penetrating waves and the transmitted neutrons are measured by a detector. The reconstructed images in NT represent the three-dimensional map of the linear neutron attenuation coefficients within an object. NT relies on the same algorithms, some of the scanning geometries and procedures involved in X-ray CT. However, NT has its peculiarities which are discussed in Chapter 2.

The history of tomography is closely linked to the development of X-ray techniques. X-radiation was discovered by the German physicist Wilhelm Röntgen (Figure 1.1a) in 1895, which received for this achievement the first Nobel Prize in Physics in 1901. At the time, it was not possible visualize a particular structure without considering the attenuation caused by the surrounding materials along the same path. The overlap of the structures is clearly visible in the famous radiograph representing the hand of Röntgen's wife (Figure 1.1b): the shadow of the ring overlaps the bony structure of the hand. The necessity to remove the impact of the overlapping structures led to the development of tomography.

The solution to the mathematical problem of how to reconstruct a function of two variables from its projections was found by the Austrian mathematician Johann Radon (1887-1956) in 1917 [1]. The importance of such result as a mathematical support

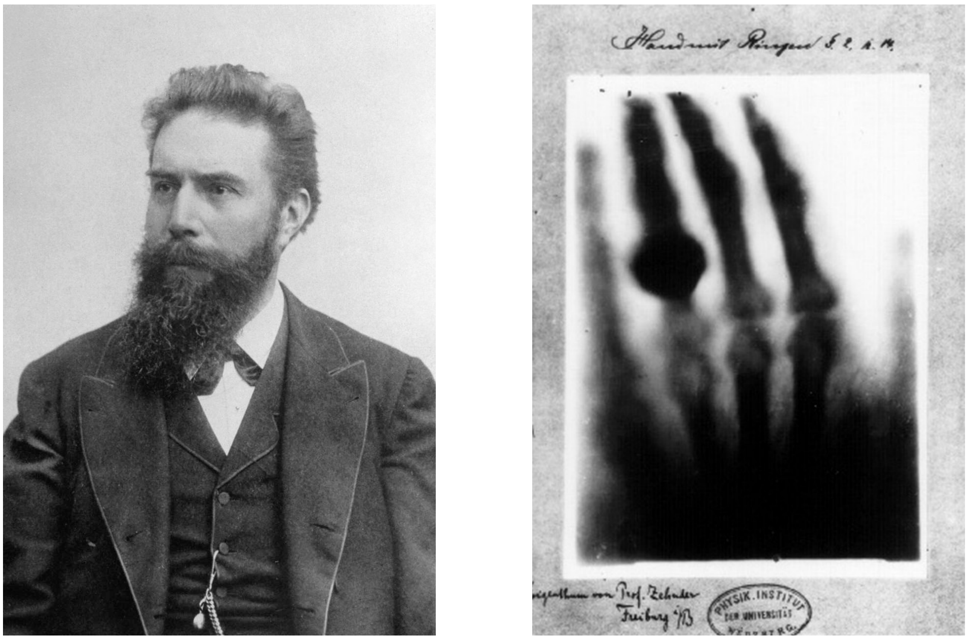

(a) (b)

Figure 1.1: (a) Wilhelm Röntgen (1845 -1923). (b) Radiograph of the hand of Anna Bertha Ludwig, Röntgen's wife.

for tomography was realized only much later. In fact, the problem was presented as a purely mathematical subject and no practical applications were proposed at the time. Furthermore, the paper was written in German language, which hindered a wide diffusion of the achievement. Only since the 1980s, two English translations have been made available [2, 3]. In 1956, Ronal Bracewell reconstructs a map of solar radiation from a set of radiation measurements across the solar surface [4]. It was the first practical application of tomography. The development of medical X-ray CT is generally credited to two physicists: Godfrey Hounsfield (1919-2004, Figure 1.2a) and Allan Cormack (1924-1998, Figure 1.2b) . The first CT scanner was built by the company EMI (Electric and Musical Industries Ltd.) in 1972. It is often claimed that revenues from the sales of The Beatles records helped funding the development of the first CT scanner at EMI, however this has recently been disputed [5]. For their pioneer work, Cormack and Hounsfield shared the Nobel Prize in Physiology and Medicine in 1979. A more detailed overview of the tomography history is reported in the books by Deans [3], Buzug [6] and Shaw [7].

(a) (b)

Figure 1.2: Inventors of X-ray CT: (a) Godfrey Hounsfield and (b) Allan Cormack.

1.2 Underlying physics

As already mentioned, the tomographic imaging is based on the image reconstruction from projections. In attenuation-based tomography the projections are obtained by radiating penetrating waves on a sample and measuring the transmitted intensity of the beam behind the sample. The goal of attenuation-based tomography is to determine the three-dimensional map of the linear attenuation coefficient within a sample. The linear attenuation coefficient (μ_T) is a characteristic of the material within the sample and it depends on the energy of the incoming beam (E). Furthermore, it can be expressed as sum of the absorption coefficient (μ_a) and the scattering coefficient (μ_s) for the coordinate $\boldsymbol{r}$, i.e.:

$$\mu_T(\boldsymbol{r}, E) = \mu_a(\boldsymbol{r}, E) + \mu_s(\boldsymbol{r}, E) \tag{1.1}$$

The attenuation coefficient has physical dimension $[\mu_T] = [L^{-1}]$ and generally is expressed in cm^{-1}. Assuming that the sample contains several attenuating species (elements or even different isotopes, in the case of NT) the equation Eq. 1.1 can be expressed as follows:

$$\begin{aligned}\mu_T(\boldsymbol{r},E) &= \sum_{i=1}^{N}\sigma_{a,i}(E)N_i(\boldsymbol{r}) + \sum_{i=1}^{N}\sigma_{s,i}(E)N_i(\boldsymbol{r}) = \\ &= \sum_{i=1}^{N}\left[\sigma_{a,i}(E)+\sigma_{s,i}(E)\right]N_i(\boldsymbol{r}) = \sum_{i=1}^{N}\sigma_{T,i}(E)N_i(\boldsymbol{r})\end{aligned} \tag{1.2}$$

where $N_i(\boldsymbol{r})$ is the number density of the i-th specie at the coordinate $\boldsymbol{r}$ and $\sigma_{a,i}$, $\sigma_{s,i}$, $\sigma_{T,i}$ are the associated microscopic absorption, scattering and total cross section, respectively.

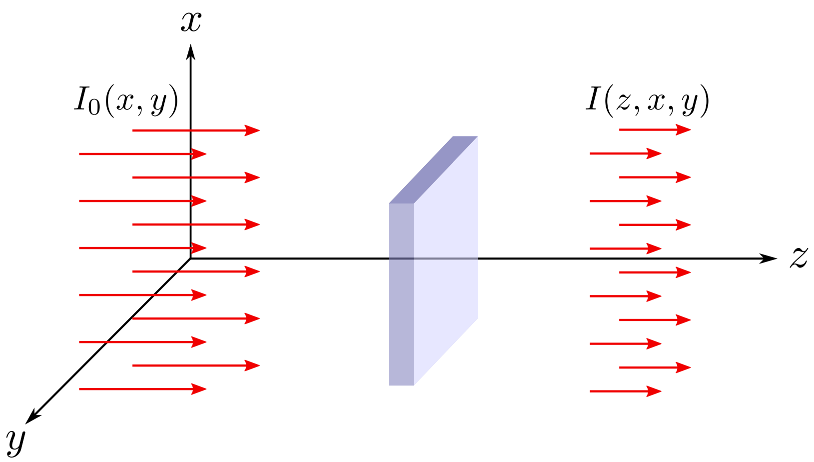

Figure 1.3: Illustration of the attenuation of an ideal beam by a slab.

Let's consider a collimated and mono-energetic beam which crosses a sample and a reference system where the propagation direction of the beam matches with the z-axis direction (Figure 1.3). The intensity of the beam component affected by absorption or scattering interaction is proportional to the intensity of the incoming beam and the extent of the attenuation domain. This statement can be expressed as the following differential expression:

$$dI(z) = -I(z)\mu_T(z)\,\mathrm{d}z \tag{1.3}$$

hence the linear attenuation coefficient μ_T is a proportionality constant (note that the x, y dependence is not expressed but is implicit in Eq. 1.3 and in the following equations). The minus sign in Eq. 1.3 implies a decrease in the beam intensity per unit positive increment $\mathrm{d}z$. By rearranging the Eq. 1.3 we obtain a first-order differential equation:

$$\frac{\mathrm{d}I}{I(z)} = -\mu_T(z)\,\mathrm{d}z \tag{1.4}$$

that we want to solve with the condition $I(z=0) = I_0$. The integration of Eq. 1.4 from $s = 0$ (position of the source) to $s = z$ leads to the following formula:

$$I(z) = I_0 e^{-\int_0^z \mu_T(s)\mathrm{d}s} \tag{1.5}$$

which is known as the *Beer-Lambert law*. The beam intensity $I(z)$ consists of the *uncollided component* which have not experienced either scattering or absorption interaction. We rename this component as $I_{unc}(z)$. However the intensity recorded by a detector placed behind the sample measures also an additional contribution due to the scattering, hence it can be expressed by the following sum:

$$I_T(z) = I_{\mathrm{unc}}(z) + I_{\mathrm{scat}}(z) \tag{1.6}$$

Now we define the *build-up function* by

$$B(\mu_s, z) = \frac{I_T(z)}{I_{\mathrm{unc}}(z)} \tag{1.7}$$

then the scattered component can be incorporated into the total intensity, by combining Eq. 1.7 with Eq. 1.5, as

$$I_T(x,y,z) = I_0(x,y)B(\mu_s,x,y,z)e^{-\int_0^z \mu_T(x,y,s)\mathrm{d}s}. \tag{1.8}$$

Note that the build-up factor is a value $B \geq 1$. It depends on the material composition and the specific geometry of the experiment, hence it is difficult to predict under typical experimental conditions. In the case of NT, the build-up is relevant for species with high scattering cross section, e.g. hydrogen compounds and elements such as silicon, nickel, copper and other highly scattering metals, and should be considered in these cases as a source of errors in quantitative analysis.

Up until now we assumed that the incoming beam is mono-energetic and the attenuation coefficient is specific for this wavelength. This assumption is acceptable for X-ray radiation produced by a synchrotron. In NT and in conventional medical CT scanner the source generates a beam characterized by a broader energy spectrum. In these cases the Beer-Lambert law (Eq. 1.5) is not valid, but we can modify it as follows:

$$\tilde{I}_T(E,x,y,z) = \tilde{I}_0(E,x,y)B(E,\mu_s,x,y,z)e^{-\int_0^z \mu_T(E,x,y,s)\mathrm{d}s} \tag{1.9}$$

where $\tilde{I}_T$ and $\tilde{I}_0$ are the spectral intensity of the incoming and outgoing beam respectively. Hence the total intensity measured behind the sample is:

$$\tilde{I}_T(x, y, z) = \int_0^{E_{max}} \tilde{I}_0(E', x, y) B(E', \mu_s, x, y, z) e^{-\int_0^z \mu_T(E', x, y, s) \mathrm{d}s} \, \mathrm{d}E' \tag{1.10}$$

This is a more accurate model for a poli-energetic beam, but in practice Beer-Lambert' s law is often used despite is conceptually wrong. In the following discussion we assume that the absorption is the dominant process and $I_s = 0$, hence $B \simeq 1$. In practice, the intensity of the generated beam and the signal recorded by the detector is affected by statistical fluctuation. It can be shown that ideally the detector counts follow Poisson distribution. However, related phenomena, such as scattering, beam-hardening and electronic noise, leads to non-Poissonian distribution.

1.3 The mathematics of Computed Tomography

In this section we present the mathematical foundations underlying the data acquisition and reconstruction in tomography. These arguments have been described in detail in the main textbooks about CT [6, 8, 9]. The scanned object is considered to comprise n_z slices with thickness Δz, which lie in planes parallel to the xy-plane and perpendicular to the z-axis. Our aim is to reconstruct the 2D map of the attenuation coefficient $\mu(x, y)$ for each slice from projection data. Each cross-section of the sample is moulded mathematically as a bounded and finite function defined in a given region and zero outside. In our dissertation we consider the *parallel beam geometry*, i.e. the projections are acquired for different angle views using a beam characterized by parallel rays. This geometry is shown in Figure 1.4. We define two Cartesian coordinate systems (x, y) and (η, ξ), which differ by a rotation of angle θ and share the same origin O as shown in Figure 1.5.

In our description we regard (x, y) as the fixed sample system and (η, ξ) as the rotated detector system. The choice of reference system follows the geometry of medical CT scanner, however it can be used also when the sample is rotated and the beam and the detector are fixed with respect to the laboratory reference system.

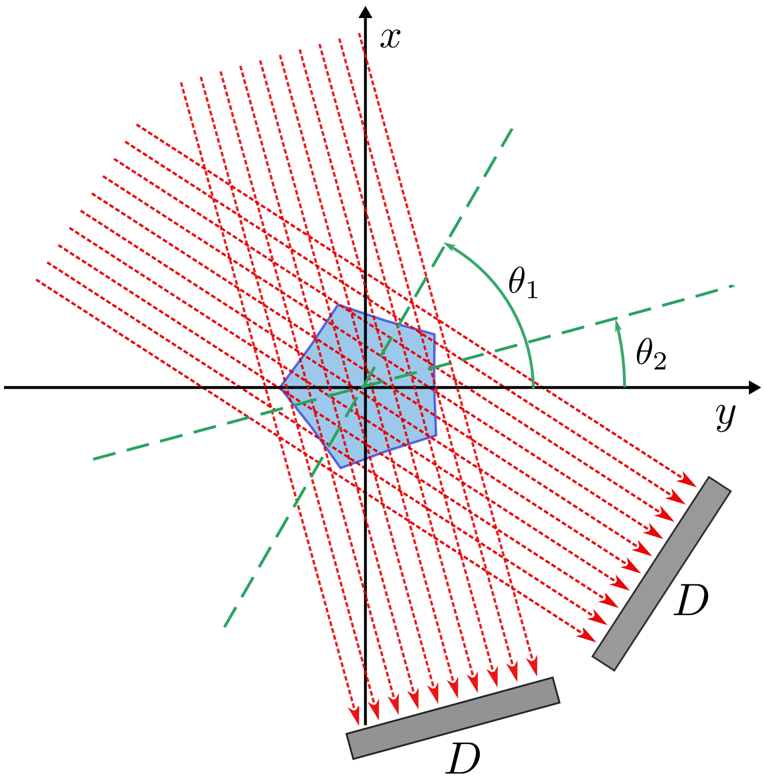

Figure 1.4: Schematic overview of the parallel beam geometry. The projections are acquired by the detector D along parallel lines for different view angles.

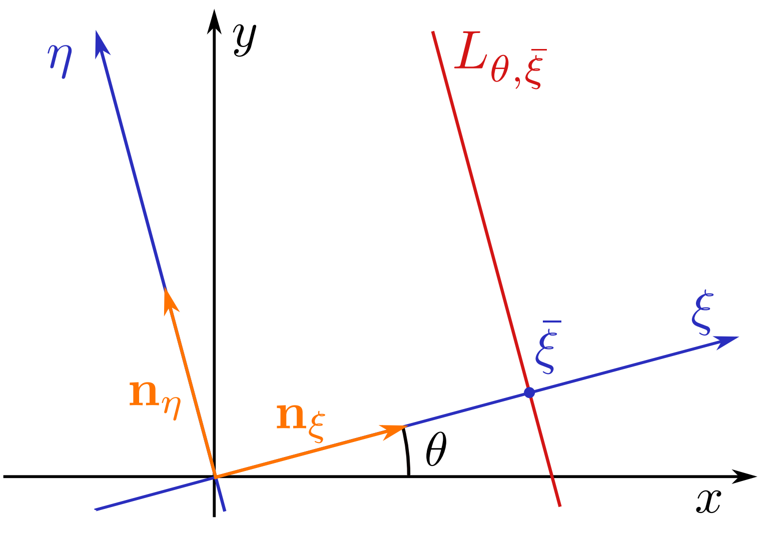

Figure 1.5: The coordinate systems (x, y) and (η, ξ). A projection line $L_{\theta,\bar{\xi}}$ is drawn for a particular value detector coordinate $\bar{\xi}$ and view angle θ.

The unit vectors $\boldsymbol{n}_\xi$ and $\boldsymbol{n}_\eta$ span the rotating (η, ξ) frame and they are defined respect the (x, y) coordinate system as:

$$\boldsymbol{n}_\xi = \begin{bmatrix} \cos\theta \\ \sin\theta \end{bmatrix} \quad (1.12a) \qquad \boldsymbol{n}_\eta = \begin{bmatrix} -\sin\theta \\ \cos\theta \end{bmatrix} \quad (1.12b) \qquad (1.12)$$

hence the coordinates of a point $\boldsymbol{r}$ can be transformed from (x, y) to (η, ξ) frames, and vice versa, by the following expressions:

$$\begin{cases} \xi = \boldsymbol{r} \cdot \boldsymbol{n}_\xi = x\cos\theta + y\sin\theta \\ \eta = \boldsymbol{r} \cdot \boldsymbol{n}_\eta = -x\sin\theta + y\cos\theta \end{cases} \tag{1.13}$$

$$\begin{cases} x = \boldsymbol{r} \cdot \boldsymbol{n}_x = \xi\cos\theta - \eta\sin\theta \\ y = \boldsymbol{r} \cdot \boldsymbol{n}_y = \xi\sin\theta + \eta\cos\theta \ . \end{cases} \tag{1.14}$$

The line parallel to the η-axis at rotation angle θ and crossing the position of a detector element ξ is described by:

$$L_{\theta,\xi} = \left\{ \boldsymbol{r} \in \mathbb{R}^2 | \boldsymbol{r} \cdot \boldsymbol{n}_\xi = x\cos\theta + y\sin\theta = \xi \right\} \tag{1.15}$$

The line integral $p_\theta(\xi)$ of the function $\mu(x, y)$ over the line $L_{\theta,\xi}$ is given by:

$$p_\theta(\xi) = \int_{\boldsymbol{r} \in L_{\theta,\xi}} \mu(\boldsymbol{r}) \, \mathrm{d}\boldsymbol{r} \tag{1.16}$$

and it can be related to the transmitted intensity $I_\theta(\xi)$ and the intensity of the incident beam I_0 by using the Beer-Lambert's law (Eq. 1.5):

$$\int_{\boldsymbol{r} \in L_{\theta,\xi}} \mu(\boldsymbol{r}) \, \mathrm{d}\boldsymbol{r} = -\log\left(\frac{I_\theta(\xi)}{I_0}\right). \tag{1.17}$$

The projection integral can be written also in the following forms using the Dirac Delta function $\delta(\cdot)$:

$$\begin{aligned} p_\theta(\xi) &= \int_{\mathbb{R}^2} \mu(\boldsymbol{r}) \delta(\boldsymbol{n}_\xi \cdot \boldsymbol{r} - \xi) \, \mathrm{d}\boldsymbol{r} = \\ &= \int_{-\infty}^{\infty} \int_{-\infty}^{\infty} \mu(x, y) \delta(x\cos\theta + y\sin\theta - \xi) \, \mathrm{d}x \, \mathrm{d}y = \\ &= \int_{-\infty}^{\infty} \mu(\xi\cos\theta - \eta\sin\theta, \xi\sin\theta + \eta\cos\theta) \, \mathrm{d}\eta \end{aligned} \tag{1.18}$$

note that the last identity is obtained by substitution of Eq. 1.14. From the mathematical point of view, the projection $p_\theta(\xi)$ represents the Radon Transform of the function $\mu(x, y)$, which is denotes by:

$$p_\theta(\xi) = (\mathcal{R}_2 \mu)(\theta, \xi) \tag{1.19}$$

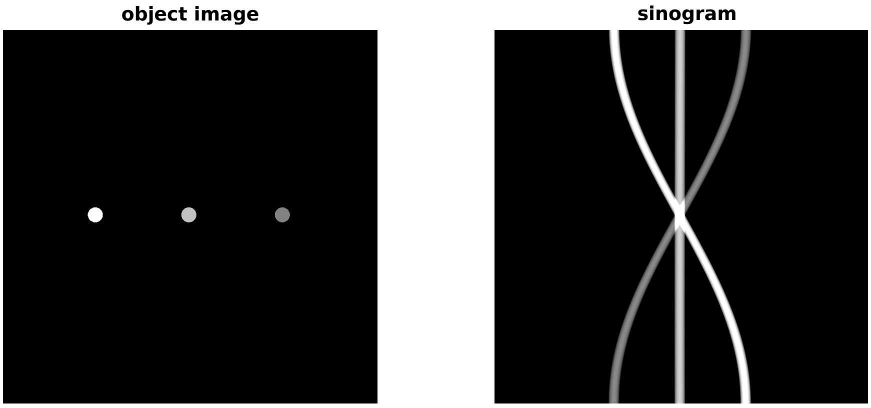

Figure 1.6: (left) A simple phantom image and (right) the corresponding sinogram.

and the Eq. 1.16 and Eq. 1.18 are equivalent expression to compute it. Typically, the projections values $p_\theta(\xi)$ are arranged in a Cartesian (ξ, θ) diagram. In this representation the projection values of points that lie outside the rotation centre produce a sinusoidal trace. For this reason, this graphical representation is often called *sinogram*. Conversely the rotation centre tracks a straight line. We provide an illustration of this behaviour in Figure 1.6, where a phantom image and the related sinogram are shown.

An important relation between the Radon transform (i.e. projections data) and the function $\mu(x, y)$ is provided by the Fourier Slice theorem, which is the underlying principle of the analytical reconstruction methods. We describe and demonstrate it in the following section.

1.3.1 Fourier slice theorem

The Fourier Slice Theorem states that the one-dimensional Fourier Transform (FT) $P_\theta(q)$ of a parallel projection $p_\theta(\xi)$ of a function $\mu(x, y)$ taken at angle θ gives a slice of the two-dimensional FT $F(u, v)$ subtending an angle θ with the u-axis.

To demonstrate this statement, we start from the 2D FT of the function $\mu(x, y)$:

$$M(u, v) = \int_{-\infty}^{\infty} \int_{-\infty}^{\infty} \mu(x, y) e^{-2\pi i (xu + yv)} \, \mathrm{d}x \, \mathrm{d}y \tag{1.20}$$

which using the polar coordinates (q, θ)

$$\begin{cases} u = q \cos\theta \\ v = q \sin\theta \end{cases} \tag{1.21}$$

can be written in this form:

$$M(u,v)\Big|_{\substack{u=q\cos\theta\\ v=q\sin\theta}} = \int_{-\infty}^{\infty}\int_{-\infty}^{\infty} \mu(x,y)e^{-2\pi i(xq\cos\theta+yq\sin\theta)}\,\mathrm{d}x\,\mathrm{d}y\,. \tag{1.22}$$

We can change the variable x and y by performing an arbitrary rotation using the Eq. 1.14 (note that the Jacobian determinant is 1 for each rotation angle). Hence we can choose the particular angle θ to obtain the new variables ξ and η, then the FT of $\mu(x,y)$ can be written as follows:

$$\begin{aligned} M(u,v)\Big|_{\substack{u=q\cos\theta\\ v=q\sin\theta}} &= \int_{-\infty}^{\infty}\int_{-\infty}^{\infty} \mu(\xi\cos\theta-\eta\sin\theta,\xi\sin\theta+\eta\cos\theta)\times \\ &\times e^{-2\pi i((\xi\cos\theta-\eta\sin\theta)q\cos\theta+(\xi\sin\theta+\eta\cos\theta)q\sin\theta)}\,\mathrm{d}\eta\,\mathrm{d}\xi = \\ &= \int_{-\infty}^{\infty}\int_{-\infty}^{\infty} \mu(\xi\cos\theta-\eta\sin\theta,\xi\sin\theta+\eta\cos\theta)e^{-2\pi iq\xi}\,\mathrm{d}\eta\,\mathrm{d}\xi\,. \end{aligned} \tag{1.23}$$

The function $e^{-2\pi iq\xi}$ does not depends on the variable η, hence we can separate the integration in this way:

$$M(u,v)\Big|_{\substack{u=q\cos\theta\\ v=q\sin\theta}} = \int_{-\infty}^{\infty}\left[\int_{-\infty}^{\infty} \mu(\xi\cos\theta-\eta\sin\theta,\xi\sin\theta+\eta\cos\theta)\,\mathrm{d}\eta\right] e^{-2\pi iq\xi}\,\mathrm{d}\xi\,. \tag{1.24}$$

Now it is clear from Eq. 1.18 that the inner integral is the projection $p_\theta(\xi)$:

$$M(u,v)\Big|_{\substack{u=q\cos\theta\\ v=q\sin\theta}} = \int_{-\infty}^{\infty} p_\theta(\xi)e^{-2\pi iq\xi}\,\mathrm{d}\xi \tag{1.25}$$

and finally the 1D FT of $p_\theta(\xi)$ is recognized at the right-hand side, hence we conclude that:

$$M(q\cos\theta,q\sin\theta) = P_\theta(q) \tag{1.26}$$

which is the theorem statement. Consequently, the FT of a parallel projection of an object obtained at angle θ equals a line of the two-dimensional FT of the object taken at the same angle, as shown schematically in Figure 1.7. The Fourier Slice theorem is the most important result for the analytical reconstruction methods, in particular it is the core of the Fourier-based methods.

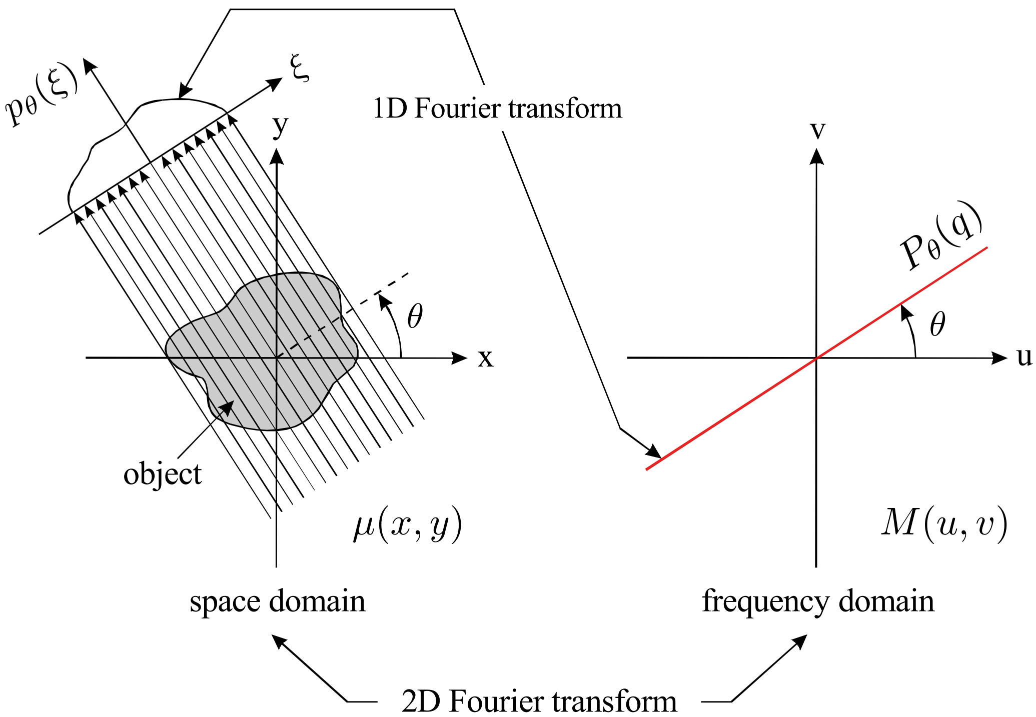

Figure 1.7: A schematic representation of the Fourier Slice Theorem. It relates the 1D FT of a projection at the angle θ to the 2D FT of the object along a radial line with direction θ.

1.3.2 Analytical reconstruction methods

The analytical methods, also known as *direct methods*, are the most popular reconstruction techniques for large scale tomography data. Analytical methods are based on a continuous representation of the problem with the assumption that noise-free projections are available for all view angles, which is clearly not possible in practice. Hence analytical formulas are approximated by discretized expressions. Analytical methods are generally computationally efficient and produce accurate reconstruction only if the number of projections and the signal-to-noise ratio are sufficiently high. When these conditions are not satisfied, direct methods produce image affected by artifacts, which make the analysis a challenging or impracticable task.

The most popular reconstruction algorithms which belongs to this category are the Filtered Back-Projection (FBP) method [6, 8, 9] and the *gridrec* method [10, 11].

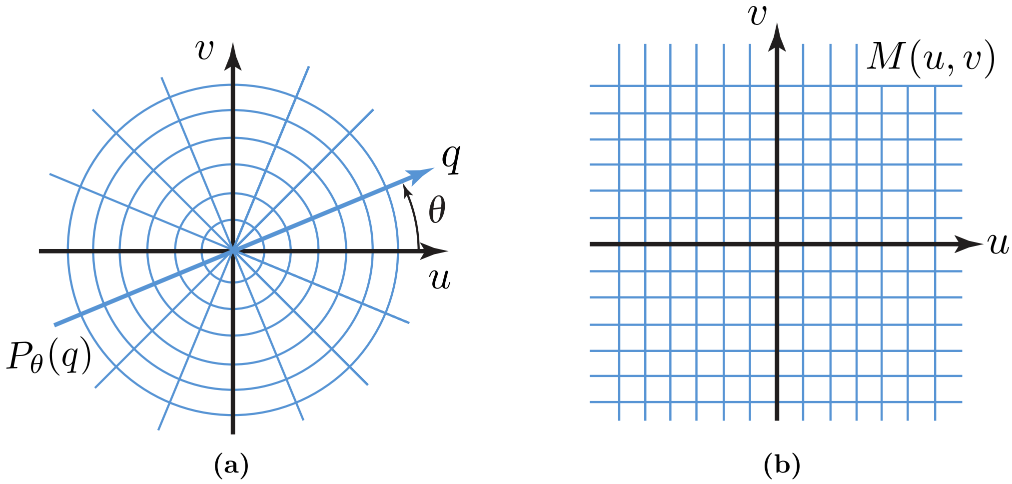

Figure 1.8: (a) The sampling of the function $P_\theta(q)$ on a polar grid and (b) the sampling of the function $M(u, v)$ on a Cartesian grid, required for direct Fourier reconstruction.

1.3.2.1 Fourier-based methods

Fourier-based reconstruction methods arise straightforwardly from the Fourier Slice theorem. The algorithms belong to the class reflect the following procedure to reconstruct $\mu(x, y)$:

1. Compute the 1D FT $P_\theta(q)$ of the projections obtained for a finite set of angles.

2. Arrange all the values of $P_\theta(q)$ on a polar grid as shown in Figure 1.8a. In order to recover the function $\mu(x, y)$ using an FFT algorithm, the 2D FT $F(u, v)$ is computed on a Cartesian grid (Figure 1.8b) from the polar configuration by means of an appropriate interpolation.

3. Compute the inverse FT of $M(u, v)$ to recover $\mu(x, y)$.

Since the density of spectral data on a polar grid decrease as one gets further away from the centre, the interpolation error also becomes larger. This implies that there is a greater error in the computation of high frequency components of an image than in low frequency ones. Such effect leads to a degradation of image quality, since high frequencies represent the image details.

A common Fourier-based reconstruction method is *gridrec* [10, 11]. It is more computationally efficient than the FBP method and provides similar reconstructed image quality when enough projections are available.

1.3.2.2 Filtered Back-Projection (FBP)

The FBP algorithm is the most used reconstruction method in CT. It can be derived as a clever result of a particular coordinate transformation. As a first step we derive a polar version of the 2D inverse FT via the Eq. 1.21 and the Fourier Slice Theorem:

$$\mu(x,y) = \int_{-\infty}^{\infty}\int_{-\infty}^{\infty} M(u,v)e^{2\pi i(ux+yv)}\,\mathrm{d}u\,\mathrm{d}v = \int_{0}^{\pi}\int_{-\infty}^{\infty} P_\theta(q)|q|e^{2\pi iq\xi}\,\mathrm{d}q\,\mathrm{d}\theta \tag{1.27}$$

then we define:

$$\widetilde{p}_\theta(\xi) = \int_{-\infty}^{\infty} P_\theta(q)|q|e^{2\pi iq\xi}\,\mathrm{d}q \tag{1.28}$$

therefore Eq. 1.27 becomes:

$$\mu(x,y) = \int_{0}^{\pi} \widetilde{p}_\theta(\xi)\,\mathrm{d}\theta\,. \tag{1.29}$$

where $\xi = x\cos\theta + y\sin\theta$, which represents detector coordinate. We conclude that the function $\mu(x,y)$ can be reconstructed by summing together the functions $\widetilde{p}_\theta(\xi)$ along their direction. This task is called *back-projection*. Furthermore $\widetilde{p}_\theta(\xi)$ is actually the high-pass filtered signal obtained from $p_\theta(\xi)$ with the filter $|q|$ in the frequency domain. This explains the name *filtered back-projection*.

Now we describe the technical implementation of the FBP method exploitable in computer programs for CT reconstruction. Since a real projection signal is discrete and also spatially limited, due to the limited number of detectors, the spectrum of the signal is repeated periodically as a result of the sampling process. The Nyquist-Shannon theorem states that a band-limited signal can be reconstructed without loss of information if the sampling interval satisfies the condition $\Delta\xi \leq 1/2q_{\max}$, where $q_{\max}$ is the highest frequency in the signal spectrum. In practice the energy contained in the Fourier transform components above a certain frequency is negligible, so for all practical purposes the projections may be considered to be band-limited. Hence the projections can be sampled at intervals $\Delta\xi = 1/2q_{\max}$:

$$p_\theta(j\Delta\xi) \quad \text{with} \quad j = -\frac{n_d}{2}, \ldots, 0, \ldots, \frac{n_d}{2} - 1 \tag{1.30}$$

where n_d is the number of sampling points, i.e. the number of detector elements. Furthermore, we assume that the projections are equal zero outside the detector, then the FT $P_\theta(q)$ can be discretized by

$$P_\theta(k\Delta q) = \Delta\xi \sum_{j=-n_d/2}^{n_d/2-1} p_\theta(j\Delta\xi) e^{-2\pi i (kj/n_d)} \tag{1.31}$$

where

$$\Delta q = \frac{2q_{\max}}{n_d} \ . \tag{1.32}$$

Since we assumed that the projections are band-limited the integral in Eq. 1.28 can be written as:

$$\widetilde{p}_\theta(\xi) \simeq \int_{-q_{\max}}^{q_{\max}} P_\theta(q)|q| e^{2\pi i q\xi} \,\mathrm{d}q \tag{1.33}$$

hence the filtered projection $\widetilde{p}_\theta(\xi)$ can be discretized and approximated by the *Riemann sum*:

$$\widetilde{p}_\theta(j\Delta\xi) \simeq \Delta q \sum_{k=-n_d/2}^{k=n_d/2} P_\theta(k\Delta q)|k\Delta q| e^{2\pi i (kj/n_d)} \ . \tag{1.34}$$

Finally, the image to reconstruct is given from the discrete approximation of the integral

$$\begin{aligned} \mu(x,y) &= \int_0^\pi \widetilde{p}_\theta(\xi)\,\mathrm{d}\theta \simeq \\ &= \frac{\pi}{N_{\text{proj}}} \sum_{i=1}^{N_{\text{proj}}} \widetilde{p}_{\theta_i}(x\cos\theta_i + y\sin\theta_i) \end{aligned} \tag{1.35}$$

where θ_i for $i = 1, 2, \ldots, N$ are the angles of the measured projections. Note that the value of $x\cos\theta_i + y\sin\theta_i$ in Eq. 1.35 may not correspond to the values $j\Delta\xi$ for which $\widetilde{p}_{\theta_i}$ is determined via Eq. 1.34. Hence $\widetilde{p}_{\theta_i}$ is approximated by a suitable interpolation; often linear interpolation is adequate.

In practice, it is not always useful to multiply frequency component of the projection with a linearly increasing function ($|q|$), since the linear weighting in the frequency domain increases the noise. Therefore the reconstructed images may finally be affected

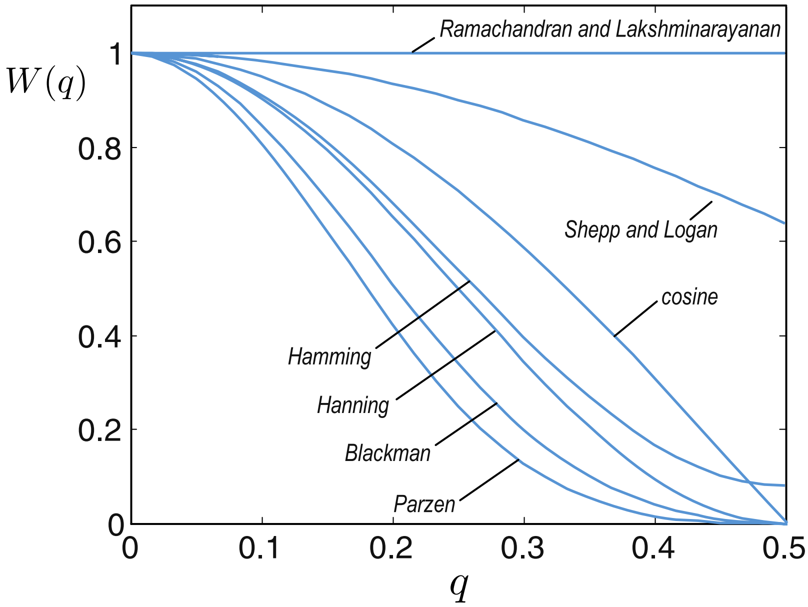

Figure 1.9: The main window functions used in FBP implementation, represented in the frequency domain. The sampling interval is set $\Delta\xi = 1$.

by strong noise. Superior results are usually obtained if one multiplies the filtered projection by a suitable window function. The purpose of the window function is to de-emphasize high frequencies which in many cases represent mostly observation noise. Consequently, the Eq. 1.34 can be modified taking into account the window function W in the frequency domain:

$$\tilde{p}_\theta(j\Delta\xi) \simeq \Delta q \sum_{k=-n_d/2}^{k=n_d/2} P_\theta(k\Delta q)|k\Delta q|W(k\Delta q)e^{2\pi i(kj/n_d)} \ . \tag{1.36}$$

There are several proposals concerning the analytic form of the window function. Here we mention some of them: Ramachandran-Lakshminarayanan (*ram-lak*), Shepp-Logan, cosine, Hamming, Hanning, Blackman and Parzen window functions. In Figure 1.9 we show these window function in the frequency domain. For brevity, we omit the related expressions in the spatial and frequency domain; a detailed description of such functions is provided by Buzug [6].

Minimum number of projections

How many projections are necessary to obtain accurate reconstruction with the FBP method? To answer this question, we consider the arrangement of spectral data points,

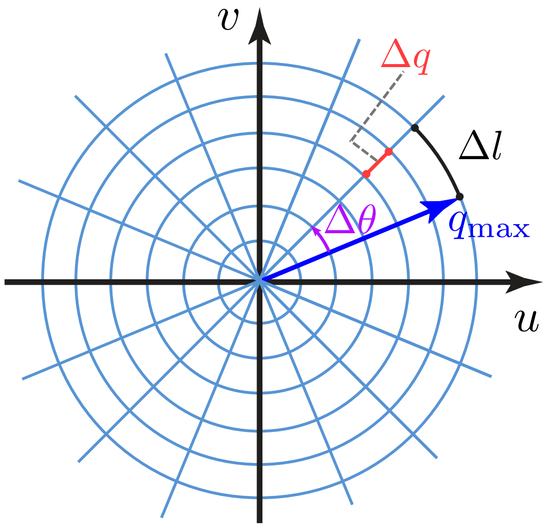

Figure 1.10: Geometrical arrangement of the sampling points in the frequency domain for projections uniformly distributed over 180°.

obtained via the Fourier Slice Theorem, represented in Figure 1.10. We note that distance between two consecutive sampling points moving in the azimuthal direction increases towards higher frequencies. The largest distance between samples in the azimuthal direction Δl is found at the radius $q_{\max}$:

$$\Delta l = q_{\max}\Delta\theta \tag{1.37}$$

where $\Delta\theta$ is the angular interval between two radial lines, therefore, if N_{proj} projections are uniformly distributed over 180°, it is given by:

$$\Delta\theta = \frac{\pi}{N_{\text{proj}}} \tag{1.38}$$

hence

$$\Delta l = \frac{\pi q_{\max}}{N_{\text{proj}}} \ . \tag{1.39}$$

Conversely, the distance between two consecutive point in the radial direction (Δq) is constant and it is given by:

$$\Delta q = \frac{2q_{\max}}{n_d} \ . \tag{1.40}$$

An adequate sampling is obtained if the distance between points in azimuthal and radial direction are almost the same, which means

$$\Delta q \simeq \Delta l \ . \tag{1.41}$$

By substituting Eq. 1.40 and Eq. 1.39 in the last expression we obtain:

$$\frac{2q_{\max}}{n_d} \simeq \frac{\pi q_{\max}}{N_{\text{proj}}} \tag{1.42}$$

which reduces to

$$N_{\text{proj}} \simeq \frac{\pi}{2} n_d \tag{1.43}$$

which implies that the number of projections should be roughly the same as the number of sampling points. When an insufficient number of projection is available the FBP produce streak artifacts due to the aliasing, known as Moiré patterns.

1.3.3 Algebraic reconstruction methods

Algebraic reconstruction methods, unlike analytical ones, are based on a fully discrete formulation of the tomographic reconstruction problem. In this approach the unknown continuous function is approximated by a linear combination of a finite number of basis functions. In our case, the map of the attenuation coefficients is approximated by

$$\mu(\boldsymbol{r}) \simeq \sum_{i=1}^{N} x_i b_i(\boldsymbol{r} - \boldsymbol{r}_i) \tag{1.44}$$

where N is the number of basis functions $b_i(\boldsymbol{r})$ and x_i with $i = \{1, \ldots, N\}$ are real coefficients. Note that each basis function $b_i(\boldsymbol{r})$ is centred at position $\boldsymbol{r}_i$. Once the basis function is fixed, $\mu(\boldsymbol{r})$ is completely described by the vector:

$$\boldsymbol{x} = (x_1, \ldots, x_N) \in \mathbb{R}^N \ . \tag{1.45}$$

The most common basis functions in imaging application are *pixels*, i.e. two-dimensional rectangular functions. In this case, each basis function is defined to have value 1 within a square domain and value 0 elsewhere. Clearly, in this representation x_j represents the average attenuation coefficient value inside the j-th pixel. Generally the function is approximated considering a square grid of $n \times n$ pixels, hence the dimension of the vector $\boldsymbol{x}$ is $N = n^2$.

Furthermore, the acquired projections represents a finite set of measurements that can be described by the vector:

$$\boldsymbol{p} = (p_1, \ldots, p_M) \in \mathbb{R}^M \quad \text{with} \quad M = N_{\text{proj}} n_d \tag{1.46}$$

where N_{proj} is the number of projection angles and n_d the number of detector elements. Using these definitions, the tomographic acquisition process can be described as a system of linear equations:

$$\sum_{j=1}^{N} a_{ij} x_j = p_i \quad \text{for} \quad i = 1, \dots, M \tag{1.47}$$

where a_{ij} is the integral along the i-th line of the j-th basis function. The last equations can be written in the matrix form:

$$\boldsymbol{Ax} = \boldsymbol{p} \tag{1.48}$$

where $\boldsymbol{A}$ is a $M \times N$ matrix, generally called *projection matrix*. The multiplication $\boldsymbol{Ax}$ is called *forward projection* of $\boldsymbol{x}$, while the multiplication $\boldsymbol{A}^T\boldsymbol{p}$ is called *backprojection* of $\boldsymbol{p}$.

The goal of CT is to solve $\boldsymbol{Ax} = \boldsymbol{p}$ for $\boldsymbol{x}$. However, the inverse of $\boldsymbol{A}$ does not exist generally. However, the problem can be solved in the least-square sense:

$$\boldsymbol{x}_{\text{LS}} = \arg\min_{\boldsymbol{x}} ||\boldsymbol{Ax} - \boldsymbol{p}||_2^2 = (\boldsymbol{A}^T\boldsymbol{A})^{-1}\boldsymbol{A}^T\boldsymbol{p} \tag{1.49}$$

where we used the Euclidean norm $||\boldsymbol{x}||_2 = (\boldsymbol{x} \cdot \boldsymbol{x})^{1/2}$. Unfortunately, the matrix $\boldsymbol{A}$ is so large that the solution in Eq. 1.49 is not feasible to compute on existing computers, even for reconstruction problem of modest size. For example, for an image of size 1000×1000 pixels and 1000 projections with 1000 detector elements we obtain $N = 10^6$ and $M = 10^6$, hence the size of the matrix $\boldsymbol{A}$ is $10^6 \times 10^6$. Such matrix can not be stored in computer memory. Hence iterative methods were used to solve approximate solution of Eq. 1.48. The projection operations can be computed on-the-fly using graphic processor units (GPUs), which reduce reconstruction times efficiently.

Since algebraic methods are based on a model of the tomographic reconstruction problem which includes a finite number of projection, unlike analytical methods assuming infinite number of projections, they tend to handle reconstruction from a limited number of projections better than direct methods. Furthermore, the effect of noise in projection data can be limited in most algebraic methods by stopping the iterative process early, which is a form of regularization.

One disadvantage of algebraic reconstruction methods is their high computational cost. Generally, the reconstruction of a full 3D volume computed on GPU using iterative methods requires some hours, depending on the number of iterations and the size of dataset. Conversely, the FBP method is able to reconstruct the same dataset with similar hardware in few minutes. For this reason, the application of algebraic methods to large-scale tomographic data is still limited.

In the following sections we describe the main algebraic reconstruction algorithms: the Algebraic Reconstruction Technique (ART) [12], Simultaneous Algebraic Reconstruction Technique (SART) [13], Simultaneous Iterative Reconstruction Technique (SIRT) [14, 15], and Conjugate Gradient Least Squares (CGLS) [16].

1.3.3.1 Algebraic Reconstruction Technique (ART)

ART was proposed to solve the image reconstruction problem by Gordon et al. [12] in 1970 but the same algorithm was known as *Kaczmarz method* [17] in numerical linear algebra since 1937. The ART was the method used by Hounsfield in 1972 for the first CT reconstruction.

The iterative procedure of the ART is based on the following update equation:

$$\boldsymbol{x}^{(k+1)} = \boldsymbol{x}^{(k)} + \lambda_k \frac{p_i - (\boldsymbol{a}_i \cdot \boldsymbol{x}^{(k)})}{||\boldsymbol{a}_i||_2^2} \boldsymbol{a}_i \quad \text{with} \quad i = (k \bmod M) + 1,\ k \geq 0 \tag{1.50}$$

where λ_k is is a real number, called *relaxation parameter*, $\boldsymbol{a}_i$ is the i-th row of the projection matrix $\boldsymbol{A}$ and $||\boldsymbol{x}||_2 = (\boldsymbol{x} \cdot \boldsymbol{x})^{1/2}$ is the Euclidean norm. The term $(\boldsymbol{a}_i \cdot \boldsymbol{x}^{(k)})$ is the forward projection of the image for the i-th ray, the difference in the numerator is the projection error, that is back-projected by multiplying the i-th row of the projection matrix $\boldsymbol{A}$.

The method can be explained through a simple geometrical description. The image to reconstruct can be represented by $(x_1, x_2, \ldots, x_N)$ which is a point in the N-dimensional space. Conversely each equation of the linear system in Eq. 1.47 represents an hyperplane. If a unique solution of the system exists, the intersection of all the hyperplanes is a single point representing the solution. To illustrate this concept we consider the case $M = 2$ and $N = 2$, which corresponds to solve a system of

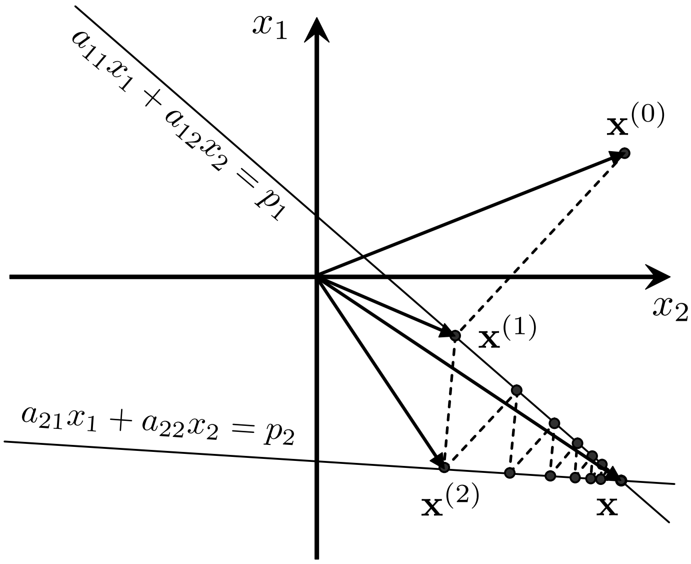

Figure 1.11: Illustration of the Kaczmarz method for a system of two linear equation with two unknowns.

two linear equation with 2 unknown variables. A geometrical representation of the problem is given in Figure 1.11. The computational procedure of Eq. 1.59 consists of choose an initial point, project it on the first line, projecting the resulting point on the second line and so forth. If a solution exists then sequence of point will converge to the line intersection which is the solution.

It is shown by Herman [18] that if the Eq. 1.48 has a solution at all and $x^{(0)}$ is selected to be the vector zero, using $\lambda_k = 1$ then the sequence $x^{(0)}, x^{(1)}, \ldots$ converges to the least-norm solution, i.e.:

$$\widetilde{\boldsymbol{x}} = \arg\min_{\boldsymbol{x}} ||\boldsymbol{x}||_2, \text{ s.t. } \boldsymbol{Ax} = \boldsymbol{p} \tag{1.51}$$

The optimal value of the relaxation parameter depends on the iteration step, the sinogram values and the sampling parameters. However, a small shift away from the value 1 can increase the convergence speed.

1.3.3.2 Simultaneous Iterative Reconstruction Technique (SIRT)

The procedure of SIRT is similar to ART but with one fundamental difference. In SIRT the image vector $\boldsymbol{x}^{(k)}$ is updated using simultaneously all equations, i.e. by performing a full forward projection, whereas in ART only a single row of the projection matrix is used for each step to update the image. Several variants of SIRT exist but all of them are described by the following iterative formula:

$$\boldsymbol{x}^{(k+1)} = \boldsymbol{x}^{(k)} + \lambda \boldsymbol{C}\boldsymbol{A}^T \boldsymbol{R}(\boldsymbol{p} - \boldsymbol{A}\boldsymbol{x}^{(k)}) \tag{1.52}$$

where λ is a relaxation parameter, $\boldsymbol{R}$ and $\boldsymbol{C}$ are symmetric positive definite matrix. The SIRT variants available in literature differs in the choice of these matrices.

In our discussion we consider the SIRT version where $\boldsymbol{R}$ and $\boldsymbol{C}$ are the diagonal matrix given by:

$$r_{kk} = \left(\sum_{l=1}^{N} a_{kl} \right)^{-1} \tag{1.53}$$

$$c_{ll} = \left(\sum_{k=1}^{M} a_{kl} \right)^{-1} \tag{1.54}$$

hence the diagonal elements of $\boldsymbol{R}$ are the inverse row sums of the matrix $\boldsymbol{A}$ and the the diagonal elements of $\boldsymbol{C}$ are the inverse column sums of the matrix $\boldsymbol{A}$. It has been shown [19, 20] that such algorithm converges to a solution of the weighted least-squares problem:

$$\widetilde{\boldsymbol{x}} = \arg\min_{\boldsymbol{x}} ||\boldsymbol{A}\boldsymbol{x} - \boldsymbol{p}||^2_{\boldsymbol{R}} \tag{1.55}$$

where it is used the norm $||x||_{\boldsymbol{R}} = \left(\boldsymbol{x}^T \boldsymbol{R}\boldsymbol{x}\right)^{1/2}$.

The SIRT method can be interpreted as a maximum likelihood algorithm. If we assume that projections can be described as Gaussian random variables, the likelihood function can be expressed as follows:

$$P(\boldsymbol{x}) = C \cdot \prod_i \exp\left\{ \frac{-\left(\sum_j a_{ij} x_j - p_i\right)^2}{2\sigma_i^2} \right\} \tag{1.56}$$

where C is a normalization constant and σ_i the standard deviation of the i-th projection. Taking the logarithm of the joint probability density function in Eq. 1.56, the original problem reduce to resolve the maximum log-likelihood problem:

$$\arg\max_{\boldsymbol{x}} \sum_i -\frac{\left(\sum_j a_{ij} x_j - p_i\right)^2}{2\sigma_i^2} \tag{1.57}$$

that can be written in matrix form:

$$\arg\min_x (\boldsymbol{Ax} - \boldsymbol{p})^T \boldsymbol{U} (\boldsymbol{Ax} - \boldsymbol{p}) \tag{1.58}$$

where $\boldsymbol{U}$ is a $M \times M$ diagonal matrix where $U_{ii} = \sigma_i^{-2}$. Note that the last equation and the optimization problem solved by SIRT (given in Eq. 1.55) are equivalent if one assume $\sigma_i^2 = \sum_l a_{il}$.

1.3.3.3 Simultaneous Algebraic Reconstruction Technique (SART)

SART can be considered a trade-off between ART and SIRT. In fact, ART suffers from salt and pepper noise, while SIRT produces more smooth images but at the expense of slower convergence. SART is a method designed to combine the best features of ART and SIRT. The iterative procedure is similar to SIRT but in SART the image vector $\boldsymbol{x}^{(n)}$ is updated using only the rows $\boldsymbol{a}_i$ of the projection matrix $\boldsymbol{A}$ related to a particular projection view. We can describe the iterative procedure of SART with the following update equation:

$$\boldsymbol{x}^{(k+1)} = \boldsymbol{x}^{(k)} + \lambda \boldsymbol{C}_\theta \boldsymbol{A}_\theta^T \boldsymbol{R}_\theta (\boldsymbol{p}_\theta - \boldsymbol{A}_\theta \boldsymbol{x}^{(k)}) \tag{1.59}$$

where $\boldsymbol{A}_\theta \in \mathbb{R}^{n_d \times N}$ contains the n_d rows corresponding to the view angle θ, p_θ contains the related n_d projection measurements, $\boldsymbol{R}_\theta \in \mathbb{R}^{n_d \times n_d}$ is diagonal and contains the inverse row sums:

$$r_{\theta_{kk}} = \left(\sum_{l=1}^{N} a_{kl} \right)^{-1} \quad \text{for } k \in S_\theta \tag{1.60}$$

while $\boldsymbol{C}_\theta \in \mathbb{R}^{N \times N}$ contains the inverse column sums restricted to the rows in S_θ

$$c_{\theta_{ll}} = \left(\sum_{k \in S_\theta}^{N} a_{kl} \right)^{-1} \quad \text{for } l = 1, ..., N \tag{1.61}$$

where S_θ is the set of the n_d indexes of the vector $\boldsymbol{p}$ associated to the view angle θ.

1.3.3.4 Conjugate Gradient Least Squares (CGLS)

Conjugate Gradient (CG) method is a popular iterative method for solving large system of linear equations of the type:

$$\boldsymbol{A}\boldsymbol{x} = \boldsymbol{b} \tag{1.62}$$

where $\boldsymbol{x}$ is an unknown vector, $\boldsymbol{b}$ is a known vector and $\boldsymbol{A}$ is a known, square, symmetric (i.e. $\boldsymbol{A}^T = \boldsymbol{A}$) and positive-definite (i.e. $\boldsymbol{x}^T\boldsymbol{A}\boldsymbol{x} > 0\ \forall \boldsymbol{x} \in \mathbb{R}^N$ s.t. $\boldsymbol{x} \neq \boldsymbol{0}$) matrix. However the CG methods can be exploited to solve the least square problem:

$$\arg\min_{\boldsymbol{x}} ||\boldsymbol{A}\boldsymbol{x} - \boldsymbol{b}||_2^2 \tag{1.63}$$

where in this case $\boldsymbol{A}$ is a general $M \times N$ matrix. In fact by setting the gradient of the squared norm to zero we obtain:

$$\boldsymbol{A}^T\boldsymbol{A}\boldsymbol{x} = \boldsymbol{A}^T\boldsymbol{b} \tag{1.64}$$

then letting $\widetilde{\boldsymbol{A}} = \boldsymbol{A}^T\boldsymbol{A}$ and $\widetilde{\boldsymbol{b}} = \boldsymbol{A}^T\boldsymbol{b}$, we obtain a linear system of the form shown in Eq. 1.62. Furthermore, it is trivial to prove that the new matrix $\widetilde{\boldsymbol{A}}$ is square, symmetric and positive-definite. Therefore the system in Eq. 1.64 can be solved via the CG method, and the least square solution can be computed at the same time. For this reason the method is called *Conjugate Gradient Least Squares*.

The computational procedure of CG is given in Algorithm 1. A detailed description of the CG method, along with meaningful illustrations is given by Shewchuk [21].

Algorithm 1 CG algorithm for solving $\boldsymbol{Ax} = \boldsymbol{b}$

$\boldsymbol{x}_0$ arbitrary
$\mathbf{r}_0 := \mathbf{b} - \mathbf{Ax}_0$
$\mathbf{p}_0 := \mathbf{r}_0$
$k := 0$
loop
    $\alpha_k := \frac{\mathbf{r}_k^\mathsf{T}\mathbf{r}_k}{\mathbf{p}_k^\mathsf{T}\mathbf{Ap}_k}$
    $\mathbf{x}_{k+1} := \mathbf{x}_k + \alpha_k \mathbf{p}_k$
    $\mathbf{r}_{k+1} := \mathbf{r}_k - \alpha_k \mathbf{Ap}_k$
  if r_{k+1} is sufficiently small **then**
    break
  end if
    $\beta_k := \frac{\mathbf{r}_{k+1}^\mathsf{T}\mathbf{r}_{k+1}}{\mathbf{r}_k^\mathsf{T}\mathbf{r}_k}$
    $\mathbf{p}_{k+1} := \mathbf{r}_{k+1} + \beta_k \mathbf{p}_k$
    $k := k + 1$
end loop
return $\mathbf{x}_{k+1}$

References

[1] J. Radon. “Über die Bestimmung von Funktionen durch ihre Integralwerte längs gewisser Mannigfaltigkeiten”. In: *Akad. Wiss.* 69 (1917), pp. 262–277.

[2] J. Radon. “On the determination of functions from their integral values along certain manifolds”. In: *IEEE Transactions on Medical Imaging* 5.4 (Dec. 1986), pp. 170–176. ISSN: 0278-0062. DOI: 10.1109/TMI.1986.4307775.

[3] S.R. Deans. *The Radon transform and some of its applications.* A Wiley-Interscience publication. Wiley, 1983. ISBN: 9780471898047.

[4] RN. Bracewell. “Strip Integration in Radio Astronomy”. In: *Australian Journal of Physics* 9.2 (1956). DOI: 10.1071/PH560198.

[5] Zeev V. Maizlin and Patrick M. Vos. “Do We Really Need to Thank the Beatles for the Financing of the Development of the Computed Tomography Scanner?” In: *Journal of Computer Assisted Tomography* 36.2 (2012), pp. 161–164. DOI: 10.1097/rct.0b013e318249416f.

[6] T.M. Buzug. *Computed Tomography: From Photon Statistics to Modern Cone-Beam CT.* Springer Berlin Heidelberg, 2008. ISBN: 9783540394082.

[7] C.C. Shaw. *Cone Beam Computed Tomography.* Imaging in Medical Diagnosis and Therapy. Taylor & Francis, 2014. ISBN: 9781439846261.

[8] A. C. Kak and M. Slaney. *Principles of computerized tomographic imaging.* Society for Industrial and Applied Mathematics, 2001.

[9] A. Rosenfeld and A.C. Kak. *Digital Picture Processing.* Computer Science and Applied Mathematics. Elsevier Science, 2014. ISBN: 9780323139915.

[10] F. Marone and M. Stampanoni. “Regridding reconstruction algorithm for real-time tomographic imaging”. In: *Journal of Synchrotron Radiation* 19.6 (Nov. 2012), pp. 1029–1037. DOI: 10.1107/S0909049512032864.

[11] Betsy A. Dowd, Graham H. Campbell, Robert B. Marr, Vivek V. Nagarkar, Sameer V. Tipnis, Lisa Axe, and D. P. Siddons. “Developments in synchrotron x-ray computed microtomography at the National Synchrotron Light Source”. In: *Developments in X-Ray Tomography II.* Ed. by Ulrich Bonse. SPIE, Sept. 1999. DOI: 10.1117/12.363725.

[12] Richard Gordon, Robert Bender, and Gabor T. Herman. “Algebraic Reconstruction Techniques (ART) for three-dimensional electron microscopy and X-ray photography”. In: *Journal of Theoretical Biology* 29.3 (1970), pp. 471–481. ISSN: 0022-5193. DOI: 10.1016/0022-5193(70)90109-8.

[13] A.H. Andersen and A.C. Kak. “Simultaneous Algebraic Reconstruction Technique (SART): A superior implementation of the ART algorithm”. In: *Ultrasonic Imaging* 6.1 (1984), pp. 81–94. ISSN: 0161-7346. DOI: 10.1016/0161-7346(84)90008-7.

[14] J. Gregor and T. Benson. “Computational Analysis and Improvement of SIRT”. In: *IEEE Transactions on Medical Imaging* 27.7 (July 2008), pp. 918–924. ISSN: 0278-0062. DOI: 10.1109/TMI.2008.923696.

[15] Peter Gilbert. “Iterative methods for the three-dimensional reconstruction of an object from projections”. In: *Journal of Theoretical Biology* 36.1 (1972), pp. 105–117. ISSN: 0022-5193. DOI: 10.1016/0022-5193(72)90180-4.

[16] M. R. Hestenes and E. Stiefel. “Methods of conjugate gradients for solving linear systems”. In: *Journal of research of the National Bureau of Standards* 49 (1952), pp. 409–436.

[17] S. Kaczmarz. “Angenäherte Auflösung von Systemen linearer Gleichungen”. In: *Bulletin International de l’Académie Polonaise des Sciences et des Lettres* 35 (1937), pp. 355–357.

[18] G.T. Herman. *Image Reconstruction from Projections: The Fundamentals of Computerized Tomography*. Computer Science and Applied Mathematics Series. Academic Press, 1980. ISBN: 9780123420503.

[19] A. van der Sluis and H.A. van der Vorst. “SIRT- and CG-type methods for the iterative solution of sparse linear least-squares problems”. In: *Linear Algebra and its Applications* 130 (1990), pp. 257–303. ISSN: 0024-3795. DOI: 10.1016/0024-3795(90)90215-X.

[20] Ming Jiang and Ge Wang. “Convergence of the simultaneous algebraic reconstruction technique (SART)”. In: *IEEE Transactions on Image Processing* 12.8 (Aug. 2003), pp. 957–961. ISSN: 1057-7149.

[21] Jonathan R Shewchuk. *An Introduction to the Conjugate Gradient Method Without the Agonizing Pain*. Tech. rep. Pittsburgh, PA, USA, 1994.

Only a fool makes no experiments.

— Charles Darwin

2 Neutron Imaging

Contents

In this chapter we provide an overview on neutron imaging. Initially, we cover the main historical developments of the technique, the fundamental physical properties of the neutron and its interaction with matter. Afterwards we provide a brief description of the neutrons production and moderation mechanisms involved in neutron sources for imaging applications. Subsequently, we describe in detail the Neutron Tomography focusing our attention on the instrumentation, the acquisition geometry and the data-processing, underlying the issues and trade-offs of the technique. Finally, we present the IMAT beamline of the ISIS pulsed neutron spallation source (UK), where the tomographic data analysed and discussed in this thesis were acquired. Hence, we provide a detailed description of the instruments and the potential imaging applications of such neutron beamline.

2.1 History of Neutron Imaging

The neutron was discovered in 1932 by the British physicist James Chadwick [1], which received the Nobel Prize in Physics for this achievement in 1935. The earliest experimental demonstration that neutrons were of relevance for imaging techniques was provided in a series of experiments by Kallman and Kuhn in the 1930's [2]. However, they obtained low quality images due the weak beam produced by a small accelerator neutron source, but these early experiments gave insight into some of the application of neutron radiography and the detection methods to produce neutron radiographs. During the Second World War there were important advances in nuclear reactor technology that increased the intensity of neutron fluxes by many orders of magnitude. The first radiograph using a beam of thermal neutrons produced by a reactor was obtained by Thewlis and Derbyshire [3] in 1956. They used the 6-MW graphite reactor BEPO at Harwell in England, producing neutron radiographs of better quality than those made previously by Kallmann. In the 1960s, the technique developed via several independent studies at different laboratories [4–6]. During this period the neutron radiography established itself as a feasible non-destructive inspection method. In the 1970s, several research reactors in Europe and America had facilities able to acquire neutron radiographs. By the mid-1980s, images were being digitized and stored on computers [7], allowing quantitative analysis of neutron images via imaging processing techniques [8].

In the last decades, the research in neutron imaging is focused on the increasing of the imaging system resolution via the enhancement of existing detectors, for example with thinner scintillation screens, and the development of new detectors, like the microchannel plate [9].

2.2 The neutron

The neutron (symbol n) is a subatomic particle with no net electric charge and mass slightly larger than that of the proton ($m_n = 1.675 \cdot 10^{-27}$ kg) . The neutron is a composite particle in the Standard Model because it is made of quarks. In fact, the neutron is composed of three valence quarks: two down quarks and one up quark. As a consequence, the neutron interacts primarily with nuclei via the strong interaction, which have effect only at short range (10^{-15} m).

Other physical properties of the neutron is its spin $s_n = 1/2$ and the associated magnetic moment $\mu_n = -0.9662 \times 10^{-26}$ J T^{-1}. Hence, neutrons can interact with external magnetic fields and with the magnetic moments of unpaired electrons in matter. Both strong and magnetic interaction probabilities are small, so neutrons generally are able to penetrate into the bulk of the sample under investigation.

The free neutron, i.e. a particle outside the nucleus and not influenced by external forces, is *unstable* because it decays into a proton, an electron and an anti-neutrino. The half-life of the neutron, i.e. the time required for the decaying quantity to fall to one half of its initial value, is $\tau_{\frac{1}{2}} = 611$ s (about ten minutes). Fortunately, this limitation is barely of significance for most neutron applications.

One important consequence of quantum mechanics is that the matter can be described as both wave and particle. In fact, a particle moving with linear momentum p can be described as a wave with the corresponding *de Broglie-wavelength* $\lambda = \frac{h}{p}$, where $h = 6.626 \times 10^{-34}$ Js is the Planck's constant. This also applies to neutrons, so the well known energy-wavelength relation for a free neutron is given by:

$$E = \frac{p^2}{2m_n} = \frac{h^2}{2m_n\lambda^2} \ . \tag{2.1}$$

Neutrons are generally produced by fission in nuclear reactors or by *spallation* nuclear reactions, in which a high-energy proton beam collides on heavy metal target and neutrons are produced from the resulting interaction with nuclei. In both cases the

Quantity	**Ultracold**	**Cold**	**Thermal**	**Epithermal**
Energy (meV)	$2.5 \cdot 10^{-4}$	1	25	1000
Temperature (K)	$2.9 \cdot 10^{-3}$	12	290	12000
Wavelength (Å)	570	9.0	1.8	0.29
Wave vector (Å^{-1})	0.011	0.7	3.5	22
Velocity (m/s)	6.9	440	2200	14000

Table 2.1: Neutron classification in terms of energy, temperature, wavelength, wave vector and velocity.

energy of emitted neutrons is of the order of magnitude of several MeV, which is too high to study condensed matter. In fact, for measurements of the static and dynamic distribution of atoms in solids, the wavelength must be in the range of the atomic distances, i.e. few Ångströms, equivalent to neutron energies of several tens of meV. Therefore, the neutron energy must be reduced from several MeV to several tens or hundred of meV. The produced neutrons are slowed down by passing the neutron beam through appropriate materials, often hydrogenous materials. The neutrons loose energy due the collision with atoms and molecules, until they reach the thermal equilibrium with the moderator medium. This process is called *moderation*, we discuss it in Section 2.6. Neutrons are generally classified in terms of the moderator temperatures, but there are different conventions in literature. We refer to the classification given in [10] which we report in Table 2.1. In particular, the thermal and cold neutron classes represent the energy ranges of interest in this thesis.

2.3 Neutron interaction with matter

Neutrons are not influenced by electric fields since they have no electric charge. However, they can only interact via the strong force or by means of magnetic interactions.

In neutron imaging applications, the neutron-matter interactions of interest are those that are able to attenuate a neutron beam. Particles are removed from the incoming beam by *absorption* or by *scattering*. The probability of physical process is described by quantum mechanics and it is represented in terms of a quantity called *cross section*, which has the dimension of an area and generally expressed in barns

(1 barn = 10^{-24} cm^2). The total cross section σ_T is given by the sum:

$$\sigma_T = \sigma_a + \sigma_s \tag{2.2}$$

where σ_a and σ_s are the absorption and scattering cross section, respectively.

The absorption occurs when a neutron is destroyed after a neutron-nucleus interaction. This process often leads to a unstable nucleus which decays with a particular lifetime. Hence, several secondary particles can be emitted, for example: an α-particle (two protons and two neutrons bound together), a β-particle (an energetic electron or positron) or γ-rays (high-energy photons). For the thermal and cold neutrons the absorption cross section decreases with the neutron energy and more precisely is inversely proportional to the incoming neutron velocity v. This energy range is often called the $1/v$ region.

The scattering occurs when a neutron is deviated from its original direction due to the interaction with the matter. The neutron scattering cross section varies irregularly across the periodic table and for different isotopes of the same element. In Figure 2.1 we show the scattering cross sections and the absorption cross sections for each bound atom of the periodic table as a function of the atomic number, derived from the data tabulation given by Sears [11]. In practice, the scattering cross sections are considered constant in the epithermal, thermal and cold neutron energy ranges. However there is a strong energy dependence for gadolinium and bound hydrogen.

Furthermore, we distinguish *coherent scattering* and *incoherent scattering*. In the first process neutron waves are scattered by different nuclei resulting in an interference pattern that depends on the relative location of the nuclei in the material. Incoherent scattering occurs when the sample includes more than one isotope or when are present isotopes with non-zero nuclear spin. In this cases no interference pattern is observed.

For each scattering process, the neutron may scatter *elastically*, i.e. maintaining its initial energy and exchanging no energy with atoms, or *inelastically*, i.e. losing or increasing its energy.

Elastic coherent scattering is exploited to obtain structural information on the arrangement of atoms in the materials. Inelastic coherent scattering gives information

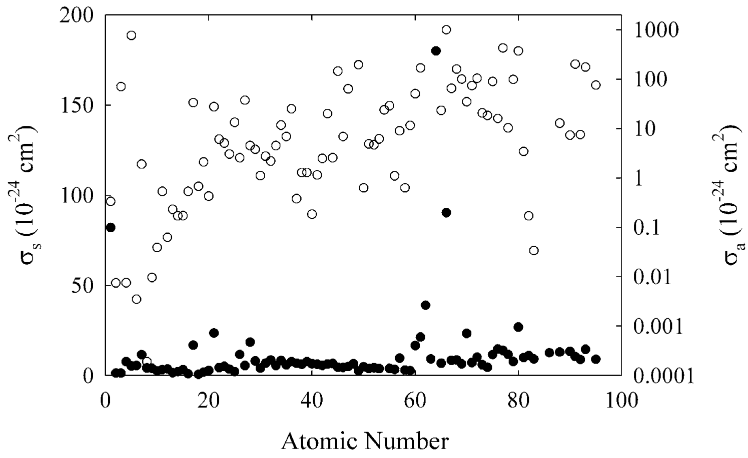

Figure 2.1: Scattering and absorption cross sections for thermal neutrons (v = 2200 m/s) for bound atoms as a function of the atomic number. Filled circles represent the scattering cross sections plotted on the linear scale placed on the left y-axis. Empty circles represents absorption cross sections on the logarithmic scale placed on the right y-axis.

on the collective excitations within the sample, such as phonons and spin waves. Inelastic incoherent scattering conveys information on single-particle excitations.

Finally, we remind that neutron carries magnetic moment which interacts with the magnetic field produced by unpaired electrons. Also in this case the neutrons were scattered. The interaction may be elastic, giving information on the magnetic order in a material, or inelastic, giving information on magnetic fluctuations.

2.4 Neutron vs X-ray for imaging application

The fundamental interactions of X-rays with matter are completely different from those of neutrons. In fact, X-rays interact primarily with the electron shell of the atoms via the electromagnetic force, while in contrast neutrons interact with the nuclei via the strong force. The main processes which lead to X-rays attenuation within matter are the photoelectric effect, the Compton scattering, and, at high energy, the pair production. The total cross sections of the X-rays increase with the atomic number and generally decrease with the energy. Conversely, as we already discussed in Section 2.3, the total cross sections for neutrons as a function of the atomic number exhibit an irregular and complex trend. In order to compare these different behaviours we report in Figure 2.2 the linear attenuation coefficients for thermal neutrons and

Attenuation coeffitients for thermal neutrons [cm⁻¹]

1a	2a	3b	4b	5b	6b	7b	8			1b	2b	3a	4a	5a	6a	7a	0
H 3.44																	He 0.02
Li 3.30	Be 0.79											B 101.60	C 0.56	N 0.43	O 0.17	F 0.20	Ne 0.10
Na 0.09	Mg 0.15											Al 0.10	Si 0.11	P 0.12	S 0.06	Cl 1.33	Ar 0.03
K 0.06	Ca 0.08	Sc 2.00	Ti 0.60	V 0.72	Cr 0.54	Mn 1.21	Fe 1.19	Co 3.92	Ni 2.05	Cu 1.07	Zn 0.35	Ga 0.49	Ge 0.47	As 0.67	Se 0.73	Br 0.24	Kr 0.61
Rb 0.08	Sr 0.14	Y 0.27	Zr 0.29	Nb 0.40	Mo 0.52	Tc 1.76	Ru 0.58	Rh 10.88	Pd 0.78	Ag 4.04	Cd 115.11	In 7.58	Sn 0.21	Sb 0.30	Te 0.25	I 0.23	Xe 0.43
Cs 0.29	Ba 0.07	La 0.52	Hf 4.99	Ta 1.49	W 1.47	Re 6.85	Os 2.24	Ir 30.46	Pt 1.46	Au 6.23	Hg 16.21	Tl 0.47	Pb 0.38	Bi 0.27	Po	At	Rn
Fr	Ra 0.34	Ac	Rf	Ha													
*Lanthanides	Ce 0.14	Pr 0.41	Nd 1.87	Pm 5.72	Sm 171.47	Eu 94.58	Gd 1479.04	Tb 0.93	Dy 32.42	Ho 2.25	Er 5.48	Tm 3.53	Yb 1.40	Lu 2.75			
**Actinides	Th 0.59	Pa 8.46	U 0.82	Np 9.80	Pu 50.20	Am 2.86	Cm	Bk	Cf	Es	Fm	Md	No	Lr			

Attenuation coeffitients for X-ray [cm⁻¹] (150kV)

1a	2a	3b	4b	5b	6b	7b	8			1b	2b	3a	4a	5a	6a	7a	0
H 0.02																	He 0.02
Li 0.06	Be 0.22											B 0.28	C 0.27	N 0.11	O 0.16	F 0.14	Ne 0.17
Na 0.13	Mg 0.24											Al 0.38	Si 0.33	P 0.25	S 0.30	Cl 0.23	Ar 0.20
K 0.14	Ca 0.26	Sc 0.48	Ti 0.73	V 1.04	Cr 1.29	Mn 1.32	Fe 1.57	Co 1.78	Ni 1.96	Cu 1.97	Zn 1.64	Ga 1.42	Ge 1.33	As 1.50	Se 1.23	Br 0.90	Kr 0.73
Rb 0.47	Sr 0.86	Y 1.61	Zr 2.47	Nb 3.43	Mo 4.29	Tc 5.06	Ru 5.71	Rh 6.08	Pd 6.13	Ag 5.67	Cd 4.84	In 4.31	Sn 3.98	Sb 4.28	Te 4.06	I 3.45	Xe 2.53
Cs 1.42	Ba 2.73	La 5.04	Hf 19.70	Ta 25.47	W 30.49	Re 34.47	Os 37.92	Ir 39.01	Pt 38.61	Au 35.94	Hg 25.88	Tl 23.23	Pb 22.81	Bi 20.28	Po 20.22	At	Rn 9.77
Fr	Ra 11.80	Ac 24.47	Rf	Ha													
*Lanthanides	Ce 5.79	Pr 6.23	Nd 6.46	Pm 7.33	Sm 7.68	Eu 5.66	Gd 8.69	Tb 9.46	Dy 10.17	Ho 10.91	Er 11.70	Tm 12.49	Yb 9.32	Lu 14.07			
**Actinides	Th 28.95	Pa 39.65	U 49.08	Np	Pu	Am	Cm	Bk	Vf	Es	Fm	Md	No	Lr			

Figure 2.2: The linear attenuation coefficients, expressed in cm^{-1}, for thermal neutrons (top) and X-rays at 150 keV (bottom) reported for each element in the periodic table [12]. The colour of each cell indicates the attenuation strength of the corresponding element. Darker grey levels indicate stronger attenuation levels.

X-rays at 150 keV of each element in the periodic table [12]. The energy of interest for imaging applications is typically of the order of meV for neutrons (i.e. thermal and cold neutrons), while of the order of tens to several hundreds of keV for X-rays.

Hence, considering the interactions of both particles and the comparison shown in Figure 2.2 we deduce the following statement:

- neutrons are very sensitive to light elements such as H, Li and B, therefore neutron imaging provides good image contrast for them. Conversely, X-rays interacts weakly with light elements, resulting in low image contrast in X-ray imaging.
- neutrons are able to penetrate metals such as Fe, Pb and Cu. On the other hand, X-rays are strongly attenuated by metals also at high energies.

- neutrons allow to distinguish isotopes of the same element and neighbour elements in the periodic table. X-rays can not provide good image contrast in this cases, since the total cross sections depend on the atomic number.

- neutrons interact strongly with magnetic moments. Conversely, this interaction is weak for X-rays. Therefore neutrons can be used to study the magnetic domain distribution and magnetic fields within materials.

In order to underline the differences between neutron and X-ray imaging, we show a neutron radiograph and an X-ray radiograph of a camera [12] in Figure 2.3. We observe in the neutron radiograph that the metallic parts appear as nearly transparent and the plastic parts (containing hydrogen) such as the film cassette are clearly visible. On the other hand, in the X-ray radiograph the metallic parts appear dark, due the high attenuation strength of metals, while the plastic parts are nearly transparent. This example demonstrate why X-ray and neutron imaging are regarded as complementary techniques.

(a) Neutron **(b)** X-ray

Figure 2.3: Comparison between radiographs [12] obtained with neutrons (a) and X-rays (b).

The main drawbacks of neutron imaging are related to limited flux of the existing neutron sources, several order of magnitude lower compared to X-ray sources. For this reason, long acquisition time are required to perform neutron measurements and spatial resolutions are still lower than achieved by X-ray imaging. In fact, a neutron tomographic scan takes several hours, conversely X-ray CT scan is generally of the order of tens of seconds. Furthermore, X-ray sources are able to image materials with micro- and nanometre size spatial resolution while neutron imaging provides spatial resolution of the order of tens of microns.

Neutron imaging is an established technology but it is still less applied than X-ray imaging, since the neutron production costs are higher. Hence, nowadays a smaller number of facilities are dedicated to neutron imaging.

2.5 Neutron Production

There are two main kinds of neutron sources for imaging applications: nuclear reactors and proton accelerator-based sources, which are respectively based on nuclear fission and nuclear spallation reactions. We discuss them separately in the following paragraphs.

2.5.1 Reactor sources

The fission of the uranium isotope ${}^{235}_{92}$U by slow neutron capture is the most frequently used reaction in nuclear reactors. At first, a thermal neutron interacts with an isotope ${}^{235}_{92}$U causing the formation of unstable nucleus ${}^{236}_{92}$U*, which disintegrates into two unequal mass fragments. Very often a neutron is emitted directly during such process, but mostly the neutrons are emitted by the fragments. The fission reaction described can be expressed as follows:

$$\mathrm{n} + {}^{235}_{92}\mathrm{U} \longrightarrow {}^{236}_{92}\,\mathrm{U}^* \longrightarrow \mathrm{n} + {}^{96}_{39}\mathrm{Y}^* + {}^{139}_{53}\mathrm{I}^*$$

where the asterisk denotes an unstable atom, Y and I are fission fragments. The reaction can be made self-sustaining because it is exothermal and releases more neutrons per fission than are needed to initiate the process.

The total energy released during the reaction is about 193 MeV, which is distributed between fission fragments (83.1 %), neutrinos (5.6 %), γ-rays (5.6 %), neutrons (3.1 %) and β-particles (2.6 %) [13]. The energy spectrum of the emitted neutrons is asymmetric. In fact, the energy distribution has a mean value of 2 MeV, but it extends up to 17 MeV.

The average number of neutrons produced by nuclear fission is about 2.5 neutrons per absorbed thermal neutron. In particular, one of these neutrons is needed to sustain the chain reaction, $\sim$ 0.5 is lost and one is available for external use.

Nuclear reactors produce a stable and continuous neutron flux, which enable tomographic acquisition with long exposure times.

Finally, we mention some important neutron facilities based on nuclear reactors: the High-Flux Reactor (HFR) at the Institute Laue-Langevin (ILL) in Grenoble, FRM-II in Munich and OPAL at the Australian Nuclear Science and Technology Organisation.

2.5.2 Accelerator-based sources

The accelerator-based sources rely on the so-called *spallation* reaction. This phenomenon is a sequence of nuclear events that take place if heavy nuclei are bombarded using particles with a Broglie wavelength which is shorter than the dimension of the nucleus (1-10 fm). The emitted high-energy neutrons, pions and spalled nuclei cause inter-nuclear cascades followed by the emission of low energy neutrons from the excited nuclei. Generally the particles used as projectiles are protons. Spallation reactions occurs for proton energies above 100 MeV. As figure of merit, protons with energy of 1 GeV impinging on a lead target produce about 25 neutrons, with an heat deposition lower than the heat to dissipate in a fission reaction producing a similar neutron flux.

The energy distributions of the neutrons emitted by spallation and by fission are quite similar in the low-energy range. In fact, both energy spectra show a distinctive peak around 2 MeV. Since the neutrons produced in spallation reaction can reach the energy of the incoming proton, a discrepancy is observed between the distributions in the high energy range.

In order to produce neutrons efficiently, as many protons as possible should produce high-energy collisions with nuclei. The neutron production efficiency become close to 100% if the proton energy is 1 GeV or higher.

Most accelerator based neutron sources deliver a pulsed beam that is suitable for time-of-flight (TOF) and energy-dispersive measurements. In pulsed source the heat is dissipated slowly in the period between pulses, hence the instantaneous power and neutron flux is very high.

Finally, we mention some important neutron facilities based on spallation reactions: SINQ at the Paul Scherrer Institute (Switzerland), ISIS at the Rutherford Appleton Laboratory (United Kingdom), Spallation Neutron Source (SNS) at the Oak Ridge National Laboratory (USA) and the Japan Proton Accelerator Research Complex (J-PARC).

The interest in spallation reaction is increasing, in fact new spallation sources are under construction worldwide.

2.6 Moderation Mechanism

The energy spectrum of the neutrons produced in both sources described above is in the MeV range. However, an energy shift of several orders of magnitude is necessary to accomplish imaging and scattering experiment. Hence, some substances with low neutron absorption cross section (to maximize the flux) and high scattering cross section (to maximize the energy loss) are used to 'slow down' the neutrons to lower energies. These materials are called *moderators* and the often used ones are water, heavy water, hydrogen, methane, graphite, beryllium and polyethylene. The energy distribution of neutrons can be tailored by controlling the temperature of the moderator.

In the following paragraphs we describe briefly the moderation mechanisms in reactor sources and in pulsed spallation sources.

2.6.1 Reactor sources

The cross section of the neutron-induced fission is much higher for thermal neutrons than for fast neutrons. In order to maintain a self-sustaining reaction using a small quantity of fissile material and obtain a suitable neutron flux for imaging applications, the fast neutrons in the core must be moderated. Furthermore, the moderating medium may be surrounded by 'reflector' materials, which scatter or reflect fast neutrons back into the moderator to gain the flux of thermalized neutron in output.

The neutron energy distribution can be altered by placing special moderators, shifting the spectrum to slightly higher or lower energies. Hence, special moderators expand the research applications of the reactor facilities.

2.6.2 Pulsed spallation sources

The moderator in a spallation source should be located as close as possible to the fast neutron source. Furthermore, for pulsed sources the temporal width of the neutron pulses coming out from the moderator must be as short as achievable. The pulse width can be reduced by surrounding the moderator with an absorbing material, called *decoupler*, such as cadmium, on all sides excepts on the output side where the neutron beam emerges. Further reduction of the pulse width can be obtained by placing an absorbing material, such as cadmium or gadolinium, in the moderator. This technique is called *poisoning* of the moderator. However, decoupling and poisoning lead to a reduced intensity of the neutron pulse. If no absorbing materials are used, the moderator is said *coupled*. In this case, the highest intensity is achieved but at the expense of broader pulse width.

2.7 Neutron Tomography

Similarly to other tomographic techniques, Neutron Tomography (NT) provides the three-dimensional map of the neutron attenuation coefficient within a sample. Data acquisition in NT consists in collecting a set of transmission radiographs at different angular views of the sample by rotating it over 180 or 360 degrees. Although NT involves the same reconstruction algorithms, procedures and scanning geometries of X-ray CT, several peculiarities should be addressed. Hence, in the following paragraphs we discuss such details of NT. In particular we focus our attention on the instrumentation, the acquisition geometry and data-processing, underling the issues and trade-offs of the technique.

2.7.1 Acquisition geometry

Instruments for NT are located at large-scale neutron facilities where the requirements for high intensity and good beam definition can be fulfilled.

A schematic diagram of a typical setup for NT is shown in Figure 2.4. The produced neutrons are generally collimated by slits, apertures or collimator systems to restrict

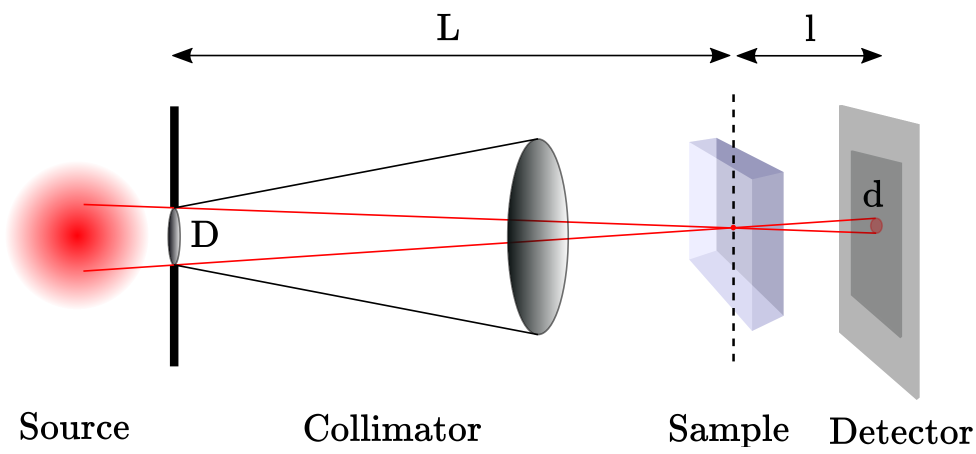

Figure 2.4: Simplified geometry of a neutron absorption tomography experiment.

the range of the radiation propagation directions. In fact, each point in a sample appears enlarged at the detector position as a result of the beam divergence and the finite size of the source. More precisely, the maximum blur d observed in the image (Figure 2.4) for a point of the sample placed at distance L from the source and at distance l from the detector is given by:

$$d = \frac{D}{L} l = \frac{l}{(L/D)} \; . \tag{2.3}$$

Hence, in order to obtain quasi point-to-point and sharp images the source size D should be small in comparison to the source-sample distance L. In this way the quality of the neutron radiographs highly depends on the ratio L/D, being the main parameter to characterize the performance of the imaging facility. A larger L/D ratio leads to better spatial resolution. Most of the neutron imaging facilities worldwide are equipped with an aperture changer, which allows to set different aperture diameters and hence different L/D ratios. However, every reduction of the aperture diameter D improves the image resolution but, on the other hand, leads to a reduction of the neutron flux (which means lower image signal-to-noise ratio), and vice versa. Hence the L/D ratio should be chosen depending on the application requirements.

2.7.2 Imaging system

In NT the data are acquired by means a digital detection system which is fixed during the inspection. The neutrons have no electric charge, so the only way to reveal them is to detect charged particles produced by the neutron-matter interaction. The most important detection reactions for thermal and cold neutrons are the following:

$$
\begin{gathered}
{}^{3}\mathrm{He} + \mathrm{n} \rightarrow {}^{3}\mathrm{H} + {}^{1}\mathrm{p} + 0.77\ \mathrm{MeV} \\
{}^{6}\mathrm{Li} + \mathrm{n} \rightarrow {}^{3}\mathrm{H} + {}^{4}\mathrm{He} + 4.79\ \mathrm{MeV} \\
{}^{10}\mathrm{B} + \mathrm{n} \rightarrow {}^{7}\mathrm{Li} + {}^{4}\mathrm{He} + 2.78\ \mathrm{MeV} \\
{}^{10}\mathrm{B} + \mathrm{n} \rightarrow {}^{7}\mathrm{Li}^{*} + {}^{4}\mathrm{He} + 2.30\ \mathrm{MeV} + \gamma\ (0.48\ \mathrm{MeV}) \\
{}^{155}\mathrm{Gd} + \mathrm{n} \rightarrow {}^{156}\mathrm{Gd} + \gamma + \text{conversion e}^{-}\ (7.9\ \mathrm{MeV}) \\
{}^{157}\mathrm{Gd} + \mathrm{n} \rightarrow {}^{158}\mathrm{Gd} + \gamma + \text{conversion e}^{-}\ (8.5\ \mathrm{MeV}) \\
{}^{113}\mathrm{Cd} + \mathrm{n} \rightarrow {}^{114}\mathrm{Cd} + \gamma + \text{conversion e}^{-}\quad .
\end{gathered}
$$

In a neutron imaging detector, the amount of electric charge produced by nuclear reactions is often not measured directly but converted into light by means of scintillator screens. The standard scintillators used for converting the neutrons to a visible light are ^{6}LiF/ZnS:Ag and 6LiF/ZnS:Cu screens. The thickness of the scintillator material is another fundamental parameter for imaging. In fact, a thicker scintillator material provides higher light-output efficiency (which leads to higher SNR of radiographs) but at the expense of lower image resolution.

To produce and record the radiographs, the scintillator is coupled to a camera. In the following discussion, the two most common neutron imaging systems used for tomography are presented.

CCD cameras Specific CCD (Charge-Coupled Device) camera are often used for NT [14]. Since the CCD chip is extremely light sensitive, all components of the detection system (i.e. scintillator, mirror, shielding and camera) are mounted inside a light-tight box. An example of such equipment is shown in Figure 2.11 (a), which illustrates one of the detection systems in use at the IMAT beamline, described in detail in Section 2.8. The CCD camera is placed at the top of the box and outside the beam direction to prevent radiation damage. A glass mirror is mounted within the box, placed at 45° from the scintillator, and reflects the light towards the CCD camera. Due to the limited neutron flux, the exposure time per radiograph should be maximized in order to obtain better image quality. Long exposure is feasible with CCD cameras cooled either by Peltier elements or liquid nitrogen, able to minimize thermal noise. The majority of NT instruments worldwide use CCD cameras from the Andor Technology [15].

Flat panels Another detection system consists of an amorphous silicon (a-Si) flat panel coupled to a scintillator. The flat panel is an array of photodiodes coupled with active thin-film transistors (TFTs) readout matrix per pixel. The scintillator is placed in contact with the semiconductor, in fact the amorphous Si bear the neutrons and γ-ray exposure better than CCD chip. Furthermore the scintillator-diode array coupling in this geometry is more efficient compared to a CCD coupled to lens and scintillator. The exposure-readout-erase process is continuously running, so the frames are produced in a continuous mode with a settable frame rate. Flat panel devices are faster in data acquisition than CCD systems. The main drawbacks of a-Si panels are the lower dynamic range and the lower SNR compared to CCD cameras.

2.7.3 Data acquisition and processing

Data acquisition and processing of a NT experiment can be summarized by the following steps:

- the sample is placed on the rotation stage as close as possible to the detector in order to reduce the geometrical blurring;
- several radiographs were acquired by rotating the sample generally with equal angular steps over 360 °;
- some *open-beam* (beam on, sample removed) and *dark-current* (beam off) images are acquired before or after the tomographic scan of the sample;
- image filters are used to suppress outlier pixels caused by damaged detector elements or by hits of γ-rays on the detector.

- the projections are normalized with respect to dark-field images, open-beam images and radiation dose, using the following formula:

$$p = -\log\left(\frac{D_{\text{flat}}}{D} \cdot \frac{I - I_{\text{dark}}}{I_{\text{flat}} - I_{\text{dark}}}\right) \tag{2.4}$$

  where I is the raw projection image, I_{dark} and I_{flat} are the mean of the dark and flat images, respectively, while D and D_{flat} are the median computed within a ROI free of sample in the projections and flat images, respectively.

- outlier pixels not yet removed appearing in most of all projections are suppressed by de-striping filters [16, 17] applied in the sinogram domain.

- a reconstruction algorithm, generally the FBP method, for parallel beam geometry is used to compute the 2D map of the attenuation coefficient for each slice of the volume. Hence, it is assumed a parallel beam geometry which is a fair approximation for neutron beams characterized by an high L/D ratio.

However, the CT reconstructed images often differs from the true images of the sample because of the non-ideal acquisition process. The unwanted features generated in the reconstructed images are called *artifacts*. In the following dissertation we describe briefly the most common image artifacts arising in NT.

Zinger artifact *Zingers* are the bright pixels occurring at random position in a projection and caused by γ-rays hitting the detector. A spot of bright pixels in a sinogram leads to a line artifact in the corresponding reconstructed image, as a result of the back-projection. An example is shown in Figure 2.5. Several image filters have been proposed in literature in order to suppress such artifact [17–20].

Ring artifact Outlier pixels occurring at the same coordinates in almost all projections lead to a ring artifact in the reconstructed image. This results in a vertical stripe in the sinogram domain. An example is shown in Figure 2.6. Generally, bad pixels in the camera or non-linearities in the detector response cause such artifact. Rings are partially suppressed by means of data normalization and outlier removal,

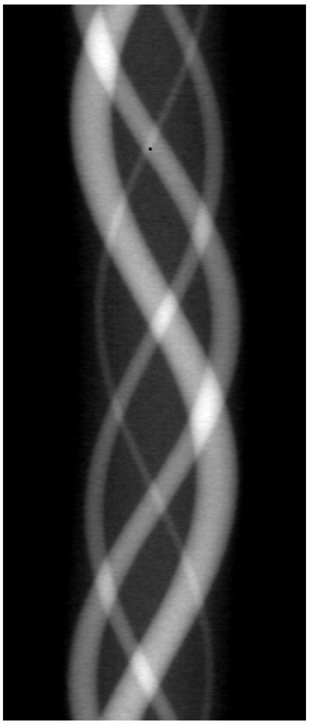

(a) Sinogram

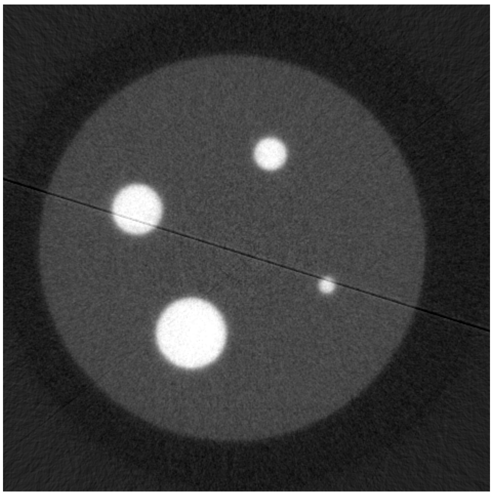

(b) Reconstructed slice

Figure 2.5: A sinogram containing a single outlier pixel (a) and the corresponding reconstructed slice (b), clearly affected by a line artifact.

but often an additional filtering is needed. Hence, several specific filters were proposed in literature for the suppression of the ring artifacts [16, 17, 21–24].

Scattering artifact In the tomographic reconstruction problem it is assumed that the detector measures the neutrons which have experienced neither absorption nor scattering. However, in practice there is a certain probability that scattered neutrons reach the detector and contribute to the estimate of the transmission. This causes a strong deformation in the reconstructed images for samples containing materials with high neutron scattering cross section. An example is shown in Figure 2.7. A correction algorithm named `QNI` was proposed by Hassanein [25]. The core of this method is the estimation, via Monte Carlo simulations, of the so-called *point scattered function* (PScF) which describes the scattering contribution for each point of the sample. However, the correction of scattering artifacts is non-trivial and even nowadays remains a challenge.

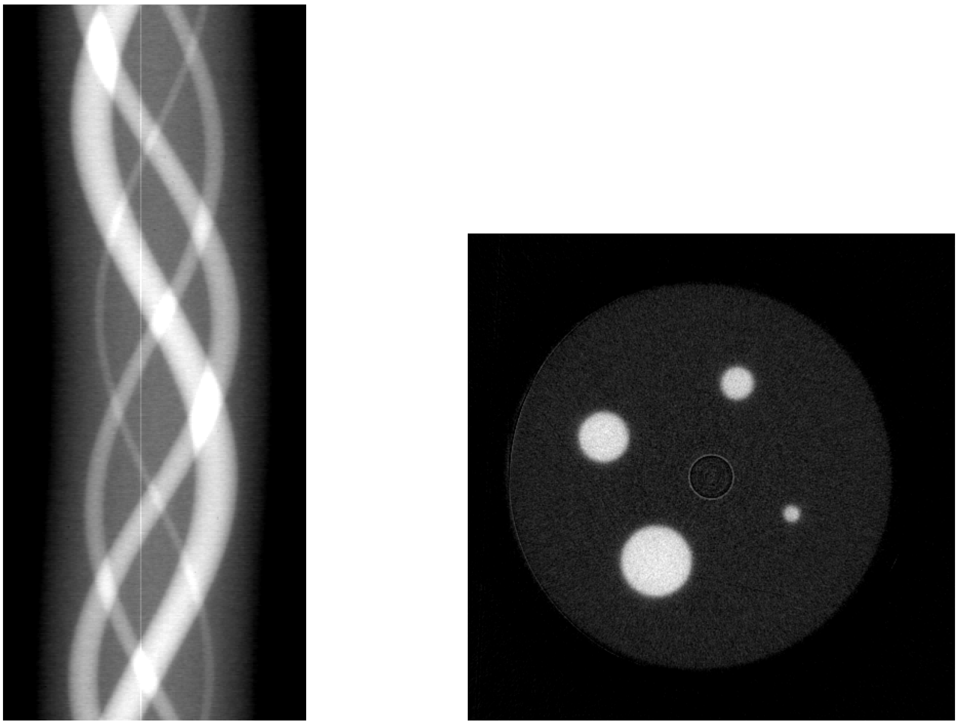

(a) Sinogram

(b) Reconstructed image

Figure 2.6: A sinogram contaminated by a vertical stripe (a) and the corresponding reconstructed slice (b), clearly affected by a ring artifact.

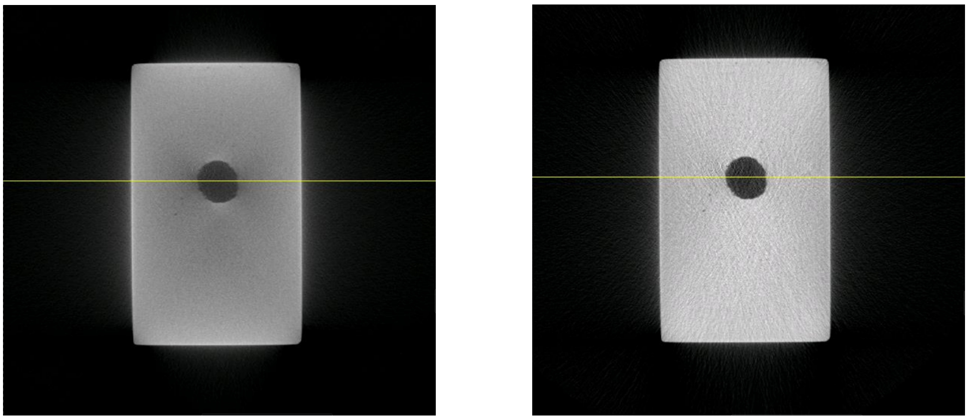

(a)

(b)

Figure 2.7: Reconstructed image of a slab affected by scattering artifact (a) and the corresponding corrected image (b).

2.8 The IMAT beamline

All the tomographic data analysed and discussed in thesis were acquired at the IMAT (Imaging and MATerials science) beamline of the ISIS pulsed neutron spallation source (UK) [26].

IMAT enables white-beam neutron radiography and tomography as well as energy-dependent neutron imaging. The latter takes advantage of TOF analysis techniques available at an accelerator-based pulsed neutron source like ISIS. In fact, narrow energy bands can be selected and analysed since time-resolving cameras are able to discriminate quasi-monochromatic neutron channels. In other words, every pixel of the imaging camera provides the transmission as a function of the neutron energy (transmission spectrum) for particular directions. In Figure 2.8 we illustrate schematically the basic imaging process in a pulsed-source instrument like IMAT. Pulses of polychromatic neutrons go through the beamline in an evacuated neutron guide and flight tube system. Obviously, faster neutrons travel ahead and the slower neutrons lag behind.

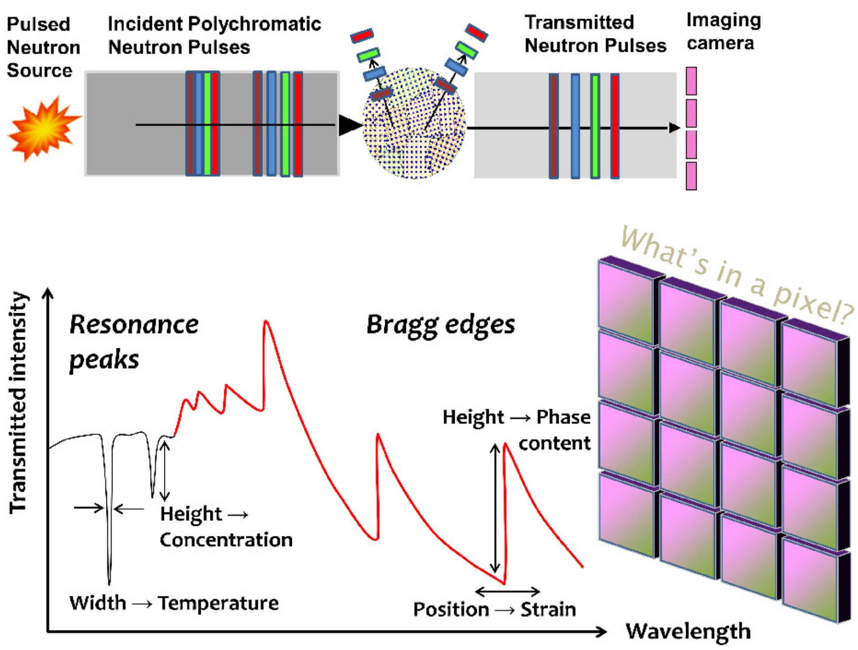

Figure 2.8: Schematic drawing representing the imaging setup of a pulsed neutron source and the measured signal by a detector in energy-selective imaging.

The neutrons that are not absorbed or scattered by the sample are recorded by the imaging detector. In white-beam acquisition mode each pixel records a grey value which is proportional to the neutron beam intensity, without energy discrimination. Conversely, in energy-dispersive acquisition mode each pixel of the imaging detector measures a neutron TOF spectrum, represented schematically in Figure 2.8. If Bragg diffraction occurs at particular neutron wavelengths then neutrons are removed from the incident beam, producing edges (Bragg edges) in the transmitted intensity. The Bragg edge transmission analysis provide phase, strain and texture parameters of materials [27–30]. Hence, neutron radiography and tomography can provide, respectively, the 2D and 3D maps of these parameters.

IMAT will be available for a wide range of materials science applications with a main emphasis on engineering studies. The facility offers a spatial resolution down to 50 μm for a field of view of up to 400 cm^2.

In the next paragraphs we present the structure and the instrumentations of the beamline following the latest reports about IMAT [31–33]. Finally, we present briefly the potential scientific and technological applications of this imaging facility.

2.8.1 Outline design and instrument parameters

IMAT is installed on a 'broad pulse' liquid hydrogen moderator on the 'West 5' (W5) beam port on the ISIS second target station (TS2), a low-power pulsed source of about 50 kW. The moderator receives neutron pulses from a tungsten target and a Be reflector assembly, slows the neutrons down, and then delivers polychromatic pulses of neutrons to the beamline with a repetition rate of 10 Hz.

This means, in the time of 0.1 s between two pulses (constituting a 'frame') neutrons of one pulse travel down the instrument and some of them are registered in the imaging camera. A long flight path of 56 m to the sample position ensures good time-of-flight resolution while retaining a wide neutron energy bandwidth.

In Figure 2.9 we shows the outline of the IMAT instrument on ISIS TS-2. In Table 2.2 we report the instrument parameters which are based on a number of design considerations [34] and on McStas simulations [35].

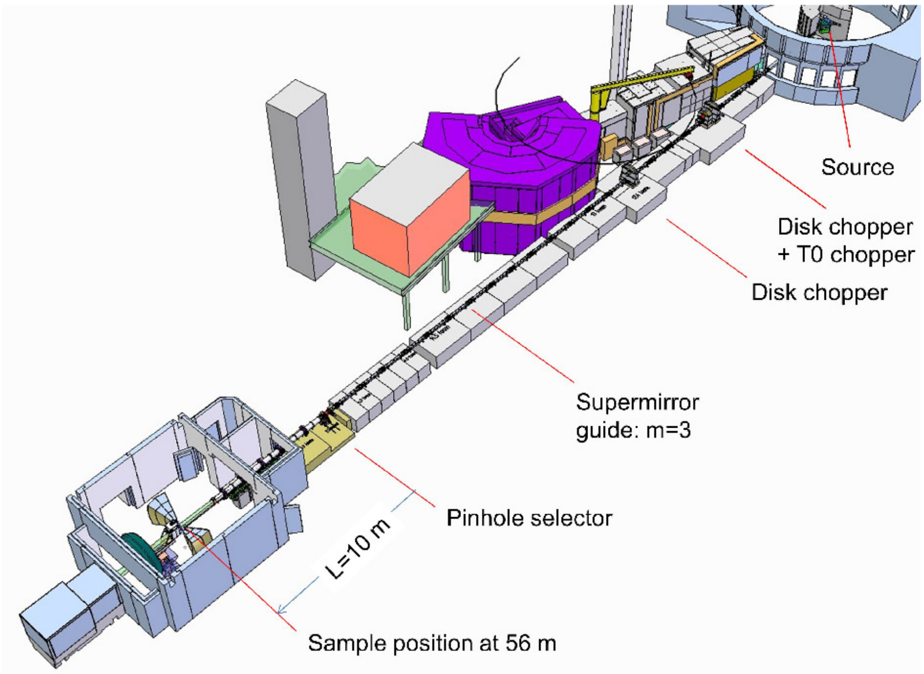

Figure 2.9: Outline design of the IMAT instrument.

General	Single frame bandwidth	1-7 Å max. flux at 3 Å
	Flight path to sample	56 m
Imaging	L: distance pinhole-sample	10 m
	D: aperture diameter	5, 10, 20, 40, 80 mm
	L/D	2000, 1000, 500, 250, 125
	Best spatial resolution	50 μm
	Max Field of View	200 $\times$ 200 mm^2
	Wavelength resolution	$\Delta\lambda/\lambda = 0.7\%$ (at 3 Å)
	Time-integrated neutron flux	$4{\times}10^7$ n cm^{-2}s^{-1}(L/D: 250)
Diffraction at 90°	Secondary flight path	2.0 m
	Detector coverage (each)	30 $\times$ 45 degrees
	Diffraction resolution	$\Delta d/d = 0.7$ % (at 3 Å)
	Minimum gauge volume	$1 \times 1 \times 1$ mm^3

Table 2.2: The main IMAT instrument parameters.

A two meter long shutter in the target station monolith is lowered into and blocks the neutron beam when entrance to the experimental area is required. A square, straight, evacuated 44 m long neutron guide starting at the upstream end of the shutter transports the neutrons to a pinhole selector at 46 m from where they are guided in evacuated ‘flight tubes’ to the sample position. There is a continuous vacuum system from the shutter to the sample area thus minimizing undesired air scattering. A 20 Hz

T0 chopper with inconnel as main absorbing material serves as fast neutron and gamma filter. Two 10 Hz double-disk choppers are used to define wide (e.g. 6 Å) or narrow (e.g. 0.5 Å) wavelength bands but also to prevent frame-overlap of neutrons between successive time frames. The choppers can be run at half-frequency to access the second frame, thereby doubling the neutron wavelength bandwidth to 12 Å. Three TOF monitors for beam diagnostics are installed in the guide section up and downstream of the choppers. The pinhole selector allows to choose five circular apertures for the imaging mode, each defining a different L/D ratio (see Table 2.2), and one large square aperture of the size of the neutron guide (95×95 mm^2) for the beam to pass through for diffraction experiments. The neutron beam travels in evacuated flight tubes from the pinhole selector to the sample area thus reducing air scattering. Downstream from the sample and camera position the beam enters a large-diameter evacuated flight tube and a 'beamstop" where the neutron beam is absorbed by a combination of B_4C materials, steel and borated wax. A large experimental area of more than 50 m^2 provides space for instrument equipment, samples and sample environment equipment. Crane access through the blockhouse roof shielding is available to lift samples and equipment into the experimental area.

The beamline components in the experimental area, represented in Figure 2.10, includes:

- sample positioning system (maximum weight: 1.5 tonnes) with a tomography rotation stage;
- fast acting attenuator to minimize activation of the sample when no data are collected (not shown);
- retractable TOF neutron beam monitor on a remote-controlled translator. Such monitor provides an incident beam spectrum for normalisation of diffraction data (not shown);
- sets of five beam delimiters, each set with four 10 mm thick sintered B_4C blades;

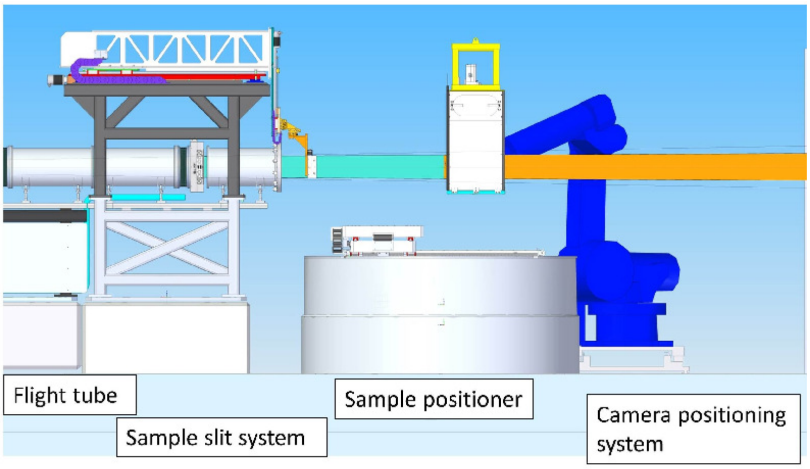

Figure 2.10: Outline design of the IMAT sample area. The imaging camera box at the sample position at about 10 m from the pinhole selector is carried by a robotic camera positioning system.

- remote-controlled retractable sample slits made of four 3 mm thick, sintered B-10 blades, for the beam size in front of the sample to be adjusted from 50 × 50 mm^2 to 1 × 1 mm^2;
- imaging camera, supported and aligned using a robotic arm able to translate the camera along the beam direction;
- evacuated flight tubes with B_4C baffles.

2.8.2 Imaging cameras

The imaging systems of IMAT will exploit TOF information for energy-resolved imaging where possible. The three detector systems developed for IMAT will be interchangeable. In Figure 2.11 we show photos of the cameras systems and their parameters are summarized in Table 2.3.

The main imaging system of IMAT consists of a light-tight box, made of black anodized aluminium, coupled with a CCD camera [36]. An interchangeable scintillator screen is placed in the front side of the box. At present ^{6}LiF/ZnS based scintillators are envisaged, with thicknesses varying from 50 μm to 400 μm. Such scintillators, when interacting with neutrons, emit visible light with wavelengths in the 450-520 nm range. A glass mirror mounted within the box, placed at 45° from the scintillator,

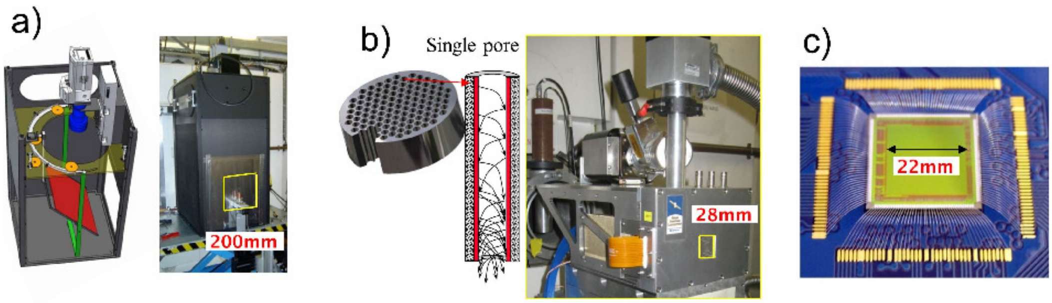

Figure 2.11: (a) the CCD/CMOS camera box; maximum sensitive detector (yellow square) of side length 200 mm; (b) the MCP system; 28 mm; (c) the GP2 system; 22 mm.

Feature	CCD/CMOS	MCP	GP2
Sensitive area [mm^2]	200×200	28×28	22×22
Number of pixel (row)	1024/2048	512	324
Spatial resolution [μm]	50	55	70
Timing resolution [ns]	–	$\sim$ 10	$\sim$ 12.5
Time slices per pulse	1/0	3000	2^{12}
Dimensions W×D×H [cm]	45×50×85	25×40×20	20×10×20
R&D	CNR Messina, Italy [36]	University of California at Berkeley, U.S.A. [37]	Oxford University, STFC, U.K. [38]

Table 2.3: The IMAT imaging detectors.

and reflects the light towards the CCD camera. This imaging system is shown in Figure 2.11 (a). A series of optical lenses allows to set different magnification ratios and hence several FOVs. The focal lengths of such lenses range from 50 mm to 135 mm while the f-numbers vary from 1.2 to 2.0. The spatial resolution depends on both the chosen focal length and the spatial density of pixels of the used CCD camera. We chose for this imaging system a FOV of 200×200 mm^2, for white beam imaging with an integrating CCD/CMOS, or for energy scans with a CCD coupled to an image intensifier which enables fast gating. It is worth mentioning that the camera has a built-in optical autofocus system [36]. This system allows to perform white-beam and energy-selective radiography and tomography measurements.

The second option is the microchannel plate system (MCP) [37]. It utilizes neutron absorption by ^{10}B atoms impregnated into the MCP glass followed by the generation of secondary electrons and signal amplification within the pores of the MCP (Figure 2.11 (b)) localized to a $\sim$ 10 μm area. The FOV is 28×28 mm^2 and the detector with 512×512 pixels is capable of providing a TOF spectrum for each pixel (of size 55×55

μm^2). The camera is placed directly in the neutron beam. The spatial resolution limit of 55 μm is given by the Timepix readout chip, but it has been shown that the resolution can be improved by event centroiding [39].

The third option for IMAT is an active pixel sensor (GP2) [38], shown in Figure 2.11 (c), which uses the PImMS-2 CMOS. A gadolinium sheet is used for converting neutrons to electrons which are then counted by a CMOS sensor with a pixel size of 70 μm. Up to 4096 times slices can be used and the timing resolution is better than 12 ns. Additionally, PImMS has four 12-bit registers per pixel.

2.8.3 IMAT imaging applications

The applications of neutron imaging techniques at the IMAT beamline range from non-destructive testing of industrial components to scientific investigations in various fields such as materials science, biology, geology and archaeology.

Here we provide some potential applications:

- fuel and fluid cell technology: e.g. functioning and in-situ testing of gas pressure flow cells / fluid cells; water / lithium distributions in fuel cells/batteries; blockages, sediments;
- earth sciences: e.g. deformation mechanisms in polymineralic rocks; water flow in porous media, mantle rheology, rock mechanics, spatial distribution of minerals;
- biomaterials and soft matter, e.g. agriculture: water uptake in plants and soil; water and hydrogen distributions in polymers and porous media;
- archaeology and cultural heritage: e.g. inorganic materials characterisation; non-destructive characterisation and multi-component analysis of archaeological objects and objects of art; ancient fabrication techniques;
- aerospace and transportation: e.g. structural integrity; lifetime and failure analysis; novel welding technology, fatigue properties; novel joining methods; composite reinforcements;

- civil engineering: e.g. integrity of load-bearing structures, reinforced concrete; water repellent agents / rising of liquids in concrete; void and density distributions in concrete.

References

[1] J. Chadwick. "Possible Existence of a Neutron". In: *Nature* 129 (1932), p. 312. DOI: 10.1038/129312a0.

[2] H. Kallmann. "Neutron radiography". In: *Research; a journal of science and its applications* 1.6 (1948), pp. 254–260.

[3] J. Thewlis and R.T.P. Derbyshire. *Report AERE M/TN 37, U. K. Atomic Energy Research Establishment*. 1956.

[4] H. Berger. *Neutron radiography: methods, capabilities and applications*. Elsevier Pub. Co., 1965.

[5] H.V. Watts. *Report ARF 1164-6*. Armour Research Foundation, 1960.

[6] E.L. Criscuolo and D. Polansky. *Proceedings Missiles and Rockets Symposium*. Concord, 1961.

[7] J. S. Brenizer, B. Hosticka, R. W. Jenkins, and D. D. McRae. "An Advanced Video System for Real-Time Neutron Radiography". In: *Neutron Radiography*. Springer Netherlands, 1987, pp. 571–578. DOI: 10.1007/978-94-009-3871-7_70.

[8] R. Polichar and D. Shreve. "Processing Of Real-Time Images for Quantitative Neutron Radiography". In: *Neutron Radiography*. Springer Netherlands, 1987, pp. 587–593. DOI: 10.1007/978-94-009-3871-7_72.

[9] Anton S. Tremsin, W. Bruce Feller, and R. Gregory Downing. "Efficiency optimization of microchannel plate (MCP) neutron imaging detectors. I. Square channels with 10B doping". In: *Nuclear Instruments and Methods in Physics Research Section A: Accelerators, Spectrometers, Detectors and Associated Equipment* 539.1 (2005), pp. 278–311. ISSN: 0168-9002. DOI: 10.1016/j.nima.2004.09.028.

[10] D.L. Price and F. Fernandez-Alonso. *Neutron Scattering – Fundamentals: Chapter 1. An Introduction to Neutron Scattering*. Experimental Methods in the Physical Sciences. Elsevier Science, 2013. ISBN: 9780128066478.

[11] Varley F. Sears. "Neutron scattering lengths and cross sections". In: *Neutron News* 3.3 (Jan. 1992), pp. 26–37. DOI: 10.1080/10448639208218770.

[12] *The Paul Scherrer Institute (PSI) - Neutron Imaging and Activation Group (NIAG)*. URL: https://www.psi.ch/niag/comparison-to-x-ray.

[13] J. Byrne. *Neutrons, Nuclei, and Matter: An Exploration of the Physics of Slow Neutrons*. Institute of Physics Pub., 1994. ISBN: 9780750302647.

[14] Helena Pleinert, Eberhard Lehmann, and Sonja Körner. "Design of a new CCD-camera neutron radiography detector". In: *Nuclear Instruments and Methods in Physics Research Section A: Accelerators, Spectrometers, Detectors and Associated Equipment* 399.2 (1997), pp. 382–390. ISSN: 0168-9002. DOI: 10.1016/S0168-9002(97)00944-3.

[15] *Andor Technology*. URL: https://andor.oxinst.com/.

[16] B. Münch, P. Trtik, F. Marone, and M. Stampanoni. "Stripe and ring artifact removal with combined wavelet-Fourier filtering". In: *Optics Express* 17.10 (2009), p. 8567. ISSN: 1094-4087. DOI: 10.1364/OE.17.008567.

[17] M. Rivers. *Tutorial Introduction to X-ray Computed Microtomography Data Processing*. University of Chicago. 1998. URL: https://www.mcs.anl.gov/research/projects/X-ray-cmt/rivers/tutorial.html.

[18] Anders P. Kaestner. "MuhRec—A new tomography reconstructor". In: *Nuclear Instruments and Methods in Physics Research Section A: Accelerators, Spectrometers, Detectors and Associated Equipment* 651.1 (2011), pp. 156–160. ISSN: 0168-9002. DOI: 10.1016/j.nima.2011.01.129.

[19] Hongyun Li, Burkhard Schillinger, Elbio Calzada, Liu Yinong, and Martin Muehlbauer. "An adaptive algorithm for gamma spots removal in CCD-based neutron radiography and tomography". In: *Nuclear Instruments and Methods in Physics Research Section A: Accelerators, Spectrometers, Detectors and Associated Equipment* 564.1 (Aug. 2006), pp. 405–413. DOI: 10.1016/j.nima.2006.04.063.

[20] J.C.E. Mertens, J.J. Williams, and Nikhilesh Chawla. "A method for zinger artifact reduction in high-energy x-ray computed tomography". In: *Nuclear Instruments and Methods in Physics Research Section A: Accelerators, Spectrometers, Detectors and Associated Equipment* 800 (Nov. 2015), pp. 82–92. DOI: 10.1016/j.nima.2015.08.012.

[21] Sofya Titarenko, Philip J. Withers, and Anatoly Yagola. "An analytical formula for ring artefact suppression in X-ray tomography". In: *Applied Mathematics Letters* 23.12 (Dec. 2010), pp. 1489–1495. DOI: 10.1016/j.aml.2010.08.022.

[22] Mirko Boin and Astrid Haibel. "Compensation of ring artefacts in synchrotron tomographic images". In: *Optics Express* 14.25 (2006), p. 12071. DOI: 10.1364/oe.14.012071.

[23] Jan Sijbers and Andrei Postnov. "Reduction of ring artefacts in high resolution micro-CT reconstructions". In: *Physics in Medicine & Biology* 49.14 (2004), N247.

[24] Carsten Raven. "Numerical removal of ring artifacts in microtomography". In: *Review of Scientific Instruments* 69.8 (Aug. 1998), pp. 2978–2980. DOI: 10.1063/1.1149043.

[25] R. Hassanein. "Correction methods for the quantitative evaluation of thermal neutron tomography". Ph. D. thesis. ETH Zurich, 2006.

[26] *ISIS Neutron and Muon Source, Science & Technology Facilities Council*. URL: https://www.isis.stfc.ac.uk.

[27] J. R. Santisteban, L. Edwards, A. Steuwer, and P. J. Withers. "Time-of-flight neutron transmission diffraction". In: *Journal of Applied Crystallography* 34.3 (May 2001), pp. 289–297. DOI: 10.1107/s0021889801003260.

[28] Anton S. Tremsin, Supriyo Ganguly, Sonia M. Meco, Goncalo R. Pardal, Takenao Shinohara, and W. Bruce Feller. "Investigation of dissimilar metal welds by energy-resolved neutron imaging". In: *Journal of Applied Crystallography* 49.4 (June 2016), pp. 1130–1140. DOI: 10.1107/s1600576716006725.

[29] J.R. Santisteban, M.A. Vicente-Alvarez, P. Vizcaino, A.D. Banchik, S.C. Vogel, A.S. Tremsin, J.V. Vallerga, J.B. McPhate, E. Lehmann, and W. Kockelmann. "Texture imaging of zirconium based components by total neutron cross-section experiments". In: *Journal of Nuclear Materials* 425.1 (2012). Microstructure Properties of Irradiated Materials, pp. 218–227. ISSN: 0022-3115. DOI: 10.1016/j.jnucmat.2011.06.043.

[30] G. Vitucci, T. Minniti, D. Di Martino, M. Musa, L. Gori, D. Micieli, W. Kockelmann, K. Watanabe, A.S. Tremsin, and G. Gorini. "Energy-resolved neutron tomography of an unconventional cultured pearl at a pulsed spallation source using a microchannel plate camera". In: *Microchemical Journal* 137 (Mar. 2018), pp. 473–479. DOI: 10.1016/j.microc.2017.12.002.

[31] T. Minniti, W. Kockelmann, G. Burca, J.F. Kelleher, S. Kabra, S.Y. Zhang, D.E. Pooley, E.M. Schooneveld, Q. Mutamba, J. Sykora, N.J. Rhodes, F.M. Pouzols, J.B. Nightingale, F. Aliotta, L.M. Bonaccorsi, R. Ponterio, G. Salvato, S. Trusso, C. Vasi, A.S. Tremsin, and G. Gorini. “Materials analysis opportunities on the new neutron imaging facility IMAT@ISIS”. In: *Journal of Instrumentation* 11.03 (Mar. 2016), pp. C03014–C03014. DOI: 10.1088/1748-0221/11/03/c03014.

[32] Winfried Kockelmann, Triestino Minniti, Daniel E. Pooley, Genoveva Burca, Ranggi Ramadhan, Freddie A. Akeroyd, Gareth D. Howells, Chris Moreton-Smith, David P. Keymer, Joe Kelleher, Saurabh Kabra, Tung Lik Lee, Ralf Ziesche, Anthony Reid, Giuseppe Vitucci, Giuseppe Gorini, Davide Micieli, Raffaele G. Agostino, Vincenzo Formoso, Francesco Aliotta, Rosa Ponterio, Sebastiano Trusso, Gabriele Salvato, Cirino Vasi, Francesco Grazzi, Kenichi Watanabe, Jason W. L. Lee, Anton S. Tremsin, Jason B. McPhate, Daniel Nixon, Nick Draper, William Halcrow, and Jim Nightingale. “Time-of-Flight Neutron Imaging on IMAT@ISIS: A New User Facility for Materials Science”. In: *Journal of Imaging* 4.3 (2018). ISSN: 2313-433X. DOI: 10.3390/jimaging4030047.

[33] Winfried Kockelmann, Genoveva Burca, Joe F. Kelleher, Saurabh Kabra, Shu-Yan Zhang, Nigel J. Rhodes, Erik M. Schooneveld, Jeff Sykora, Daniel E. Pooley, Jim B. Nightingale, Francesco Aliotta, Rosa C. Ponterio, Gabriele Salvato, Dario Tresoldi, Cirino Vasi, Jason B. McPhate, and Anton S. Tremsin. “Status of the Neutron Imaging and Diffraction Instrument IMAT”. In: *Physics Procedia* 69 (2015), pp. 71–78. DOI: 10.1016/j.phpro.2015.07.010.

[34] W. Kockelmann, S.Y. Zhang, J.F. Kelleher, J.B. Nightingale, G. Burca, and J.A. James. “IMAT – A New Imaging and Diffraction Instrument at ISIS”. In: *Physics Procedia* 43 (2013), pp. 100–110. DOI: 10.1016/j.phpro.2013.03.013.

[35] G Burca, W Kockelmann, J A James, and M E Fitzpatrick. “Modelling of an imaging beamline at the ISIS pulsed neutron source”. In: *Journal of Instrumentation* 8.10 (Oct. 2013), P10001–P10001. DOI: 10.1088/1748-0221/8/10/p10001.

[36] V. Finocchiaro, F. Aliotta, D. Tresoldi, R. C. Ponterio, C. S. Vasi, and G. Salvato. “The autofocusing system of the IMAT neutron camera”. In: *Review of Scientific Instruments* 84.9 (Sept. 2013), p. 093701. DOI: 10.1063/1.4819793.

[37] A.S. Tremsin, J.V. Vallerga, J.B. McPhate, and O.H.W. Siegmund. “Optimization of high count rate event counting detector with Microchannel Plates and quad Timepix readout”. In: *Nuclear Instruments and Methods in Physics Research Section A: Accelerators, Spectrometers, Detectors and Associated Equipment* 787 (July 2015), pp. 20–25. DOI: 10.1016/j.nima.2014.10.047.

[38] Claire Vallance, Mark Brouard, Alexandra Lauer, Craig S. Slater, Edward Halford, Benjamin Winter, Simon J. King, Jason W. L. Lee, Daniel E. Pooley, Iain Sedgwick, Renato Turchetta, Andrei Nomerotski, Jaya John John, and Laura Hill. “Fast sensors for time-of-flight imaging applications”. In: *Phys. Chem. Chem. Phys.* 16.2 (2014), pp. 383–395. DOI: 10.1039/c3cp53183j.

[39] Anton S. Tremsin, Jason B. McPhate, John V. Vallerga, Oswald H.W. Siegmund, W. Bruce Feller, Eberhard Lehmann, Anders Kaestner, Pierre Boillat, Tobias Panzner, and Uwe Filges. “Neutron radiography with sub-15μm resolution through event centroiding”. In: *Nuclear Instruments and Methods in Physics Research Section A: Accelerators, Spectrometers, Detectors and Associated Equipment* 688 (Oct. 2012), pp. 32–40. DOI: 10.1016/j.nima.2012.06.005.

Alles Gescheite ist schon gedacht worden.
Man muss nur versuchen, es noch einmal zu denken.

All intelligent thoughts have already been thought;
what is necessary is only to try to think them again.

— Johann Wolfgang von Goethe

3
Comparison of Algebraic Reconstruction Methods for Neutron Tomography

Contents

This chapter is based on:

D. Micieli, T. Minniti, V. Formoso, W. Kockelmann and G. Gorini. “A comparative study of reconstruction methods applied to Neutron Tomography”. In: *Journal of Instrumentation* 13.06 (Jun. 2018), p. C06006.

DOI: 10.1088/1748-0221/13/06/c060065.

3.1 Introduction

NT has been used in several areas such as material science, engineering, geology, cultural heritage, archaeology and industrial applications. As we already discussed in Chapter 2, NT provides complementary information to X-ray CT and in some cases offers incomparable results. However, the major drawback of NT is the limited particle flux of the existing neutron sources, several orders of magnitude lower compared to synchrotron X-ray sources. It follows that long scan times - generally several hours, depending on the sample and the desired spatial resolution - are required to perform NT scans. In the NT field there is great interest in the reduction of scan time, dictated by the high neutron production cost, aimed at optimizing the beamtime usage at neutron imaging beamlines.

The total scan time can be reduced by limiting the number of projections. As we already discussed in Chapter 1, analytical reconstruction methods, such as the widely used Filtered Back-Projection (FBP), lead to aliasing artefacts in the reconstructed images when only a small number of projections is available [1]. In fact, they are based on the assumption that projections are available for all angles in the interval $[0, \pi)$, or $[0, 2\pi)$, that is not possible in practice. In the finite case, an analytical formula is approximated by a discretized expression. This approximation becomes poor when the number of projections does not satisfy the Nyquist-Shannon condition. The resulting artefacts in the CT images make the analysis and the segmentation a challenging or impracticable task.

On the other hand, iterative reconstruction methods have advantages over the analytical ones when data are noisy and limited [2]. However, the computational cost is several orders of magnitude higher than analytical methods, so they were not feasible in the past. Nowadays, the availability of large computational power in standard workstation and the highly optimized implementations on Graphics Processor Units (GPUs) [3] make iterative methods a feasible tool for CT reconstruction.

For different tomographic techniques, some experimental and practical constraints may impose a reduction of the number of projections. For example, in medical imaging the radiation dose for patients can be minimized by limiting the numbers of angles [4]. In electron tomography, the same strategy is necessary to prevent the damage of the sample [5]. The reduction of the total scan time in industrial tomography and in the luggage inspection at airports can be only achieved by limiting the number of projections [6, 7]. Therefore, similar problems were treated and the mathematical tools were developed, but the adaptability of such methods in NT has not been fully studied, therefore their application to NT is still limited.

In this chapter, we present a comparative study of all the algebraic methods described in Subsection 1.3.3 and the FBP algorithm applied to NT reconstruction of under-sampled datasets. For this purpose, a phantom sample was analysed by means of white beam NT performed at the IMAT beamline, ISIS Neutron Source, UK. Experimental data were used to test the performances of FBP algorithm and the algebraic reconstruction methods as a function of the number of projections and for different setups of the imaging system. After a brief overview of the relevant image quality indexes for tomography, we quantitatively compare the reconstructed images in terms of such indexes and the benefits of algebraic methods for the limited datasets are discussed.

3.2 The experiment

3.2.1 Sample description

A phantom sample characterized by a simple geometric shape was built and scanned by means of NT in order to test the performances of different reconstruction techniques. The phantom is an aluminium cylinder, with diameter of 24 mm and height of 20 mm, containing 4 holes of different diameters (1 mm, 2 mm, 3 mm and 4 mm) and filled with iron powder. A schematic drawing and the 3D design of the phantom are shown in Figure 3.1.

3.2.2 Data acquisition at the IMAT beamline

Neutron images of the phantom were acquired at the IMAT beamline [8, 9], ISIS neutron spallation source, Rutherford Appleton Laboratory, UK.

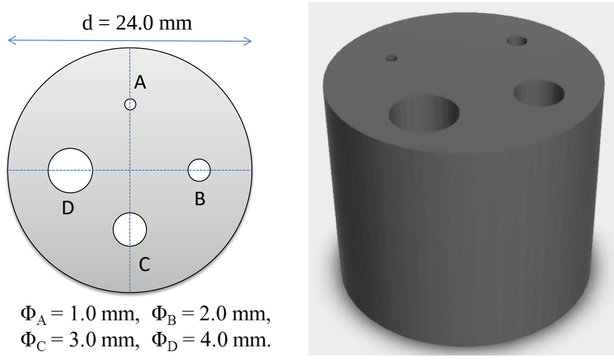

(a) (b)

Figure 3.1: Cross section layout (a) and 3D representation (b) of the phantom analysed

The sample was fixed on the rotating platform using double-sided tape and placed at the distance $L = 10$ m from the beam aperture and at the distance $d = 17$ mm from the scintillator screen. The selected diameter of the beam aperture was $D = 40$ mm that defines an L/D ratio of 250 and ensures a neutron flux of $6 \cdot 10^6$ n cm^{-2} s^{-1} [10]. The detection system consisted of a 16-bit sCMOS camera (ZYLA 4.2 Plus) with 2048×2048 pixels coupled with optical lenses and two ^{6}LiF/ZnS based scintillators with thickness 50 μm and 150 μm, respectively. The focal length was 135 mm and the aperture $f = 2$. The field-of-view was set to 59.5×59.5 mm^2 in order to image the whole phantom. The resulting pixel size was 29 μm. A set of tomograms were collected by performing uniformly spaced angular scan of 1125, 563, 375, 225, 125 and 75 projections in the range [0°, 360°) by alternating the two scintillators. The use of different scintillator thicknesses allows to acquire projection data characterized by different spatial resolutions and Signal-to-Noise Ratios (SNRs). The datasets with number of projections $N = 1125$ satisfy the Nyquist-Shannon condition, since the widest horizontal dimension of the sample is 708 pixels long. A stack of 100 open beam and 100 dark field images were taken as well before and after each tomographic scan for normalization purposes. The exposure time for each projection was 30 s.

3.3 Data processing and CT reconstruction

The normalization of the data was performed by using the log-transformation, the flat fielding and the dark subtraction procedure with the correction of the neutron dose

[11]. In fact, the flux of the beam on a neutron spallation source is rarely constant, therefore the projections are exposed at variable neutron dose. The normalization was performed by using the formula:

$$p = -\log\left(\frac{D_{\text{flat}}}{D} \cdot \frac{I - I_{\text{dark}}}{I_{\text{flat}} - I_{\text{dark}}}\right) \tag{3.1}$$

where I is the raw projection image, I_{dark} and I_{flat} are the mean of the dark and flat images, respectively, while D and D_{flat} are the median computed within a region of interest (ROI) free of sample in the projections and flat images, respectively. Afterwards, the normalized data were pre-processed by removing dead-pixels and gamma-spots, while ring artifacts were suppressed by means of a filter based on combined wavelet and Fourier analysis [12]. Finally, several reconstruction algorithms were performed on such pre-processed data. The CT reconstruction methods considered in this study are: Filtered Back Projection (FBP) [1], Simultaneous Algebraic Reconstruction Technique (SART) [13], Simultaneous Iterative Reconstruction Technique (SIRT) [14] and Conjugate Gradient Least Squares (CGLS) [15]. Pre-processing, reconstruction and analysis steps were performed by means of the NeuTomPy toolbox, a new Python package for tomographic data processing described in detail in Chapter 5.

3.4 Image quality assessment

The quality of a CT image is determined by several factors such as spatial resolution, image contrast, noise and artefacts. In order to assess these factors and compare the reconstructed images quantitatively we used *full-reference* and *no-reference* image quality indexes [16]. In the first class of quality metrics, the original image, free of any noise or distortions, is assumed to be known and used as reference image to make a comparison with an input image. Conversely, *no-reference* quality metrics can be computed also when the reference image is not available.

In this work, we regarded as reference image the reconstructed slice obtained by applying a 3D median filter to the FBP reconstruction of the dataset with $N = 1125$ projections acquired with the scintillator 50 μm thick. In this case, the median filter reduces the noise present in the FBP reconstructed slice and at the same time preserves the edges, as shown in Figure 3.2.

In the following paragraphs we provide a description of the relevant image quality indexes for tomography. Subsequently, the performances of the FBP, SIRT, SART and CGLS reconstruction algorithm were tested as a function of the scintillator thickness and the number of projections, by means of the image quality indexes described.

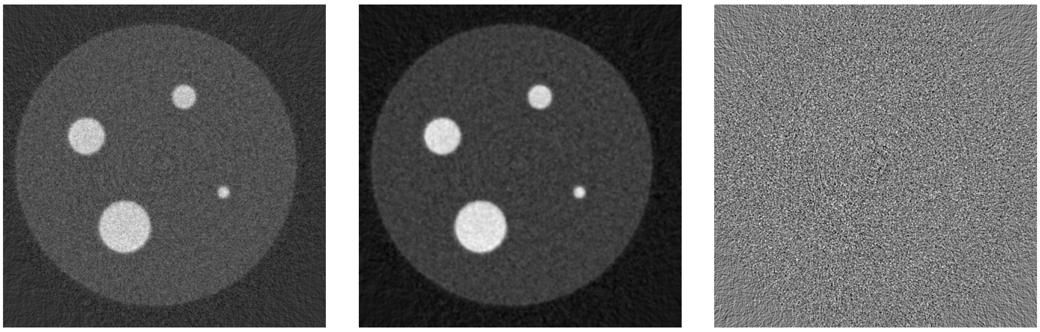

(a) Original **(b)** Filtered **(c)** Original - Filtered

Figure 3.2: A reconstructed slice obtained by applying the FBP reconstruction algorithm to the dataset characterized by 1125 projections and scintillator thickness = 50 μm (a), and the corresponding image obtained by applying a 3D median filter (b). The difference image (c) shows that the filter removes the noise and CT artifacts while it preserves the edges. The filtered image (b) was used as reference image for the computation of the *full-reference* quality metrics.

3.4.1 Full Width at Half Maximum (FWHM)

The edge quality in an image can be estimated by taking into account the steepness of a strong edge profile [17]. The latter can be fitted by a generic sigmoid function:

$$f(x) = \frac{p_0}{2}\left\{\mathrm{Erf}\left[p_1(x-p_2)\right]+1\right\}+p_3 \tag{3.2}$$

where p_0, p_1, p_2 and p_3 are fitting parameters and $\mathrm{Erf}(x)$ is the Gauss error function defined as:

$$\mathrm{Erf}(x) := \frac{2}{\sqrt{\pi}}\int_0^x e^{-t^2}\,\mathrm{d}t\,. \tag{3.3}$$

The derivative of Eq. 3.2 returns a Gaussian function with standard deviation:

$$\sigma = \frac{1}{\sqrt{2}p_1}\,. \tag{3.4}$$

The Full Width at Half Maximum (FWHM) of the resulting Gaussian function can be used to quantitatively assess the edge quality. Recalling the relation FWHM $= 2\sqrt{2\ln 2}\sigma$, the FWHM and its uncertainty (σ_{FWHM}) can be evaluated from the parameter p_1:

$$\text{FWHM} = \frac{2\sqrt{\ln 2}}{p_1}\,, \qquad \sigma_{\text{FWHM}} = \frac{2\sqrt{\ln 2}}{p_1^2}\sigma_{p_1}\,. \tag{3.5}$$

We remind that lower FWHM values indicate sharper edges.

In our study, 60 line profiles in the radial direction with respect to the centre of the hole B (Figure 3.3) were tracked and evaluated. These data were averaged and the resulting profile was fitted with the function given in Eq. 3.2, as shown in Figure 3.4.

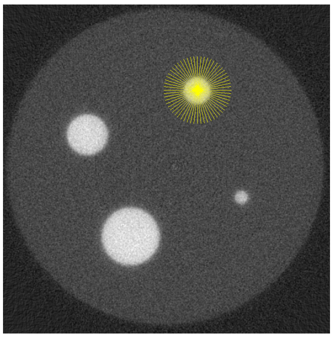

Figure 3.3: Line profiles tracked for the evaluation of the FWHM.

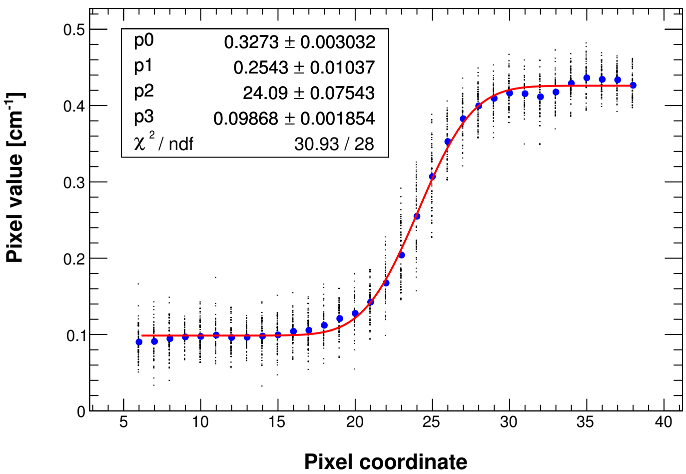

Figure 3.4: Edge quality measurement. The figure shows 60 individual line profiles (black dots), the resulting average profile (blue dots) and the fitted sigmoid function of Eq. 3.2 (red line) obtained from a FBP reconstruction ($N = 1125$, scintillator thickness $= 150$ μm). The FWHM of the Gaussian function obtained by computing the derivative of the fitting function was used as edge quality metric.

3.4.2 Contrast-to-Noise Ratio (CNR)

The Contrast-to-Noise Ratio measures the detectability of a feature in an image. One way to define the CNR [18, 19] is the following:

$$\mathrm{CNR} = \frac{\mu_{\text{sign}} - \mu_{\text{bg}}}{\sigma_{\text{bg}}} \tag{3.6}$$

where μ_{sign} and μ_{bg} are the average pixel value of the feature and background area, respectively, and σ_{bg} is the standard deviation of the background area. The CNR is a *no-reference* image quality index.

In our analysis, we consider the area containing the iron as the feature area (red circle in Figure 3.5), whereas the area outside the sample as background (yellow rectangle in Figure 3.5).

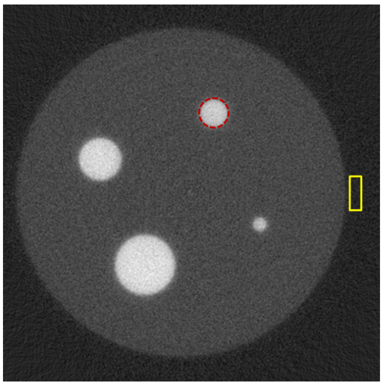

Figure 3.5: The signal area (red circle) and the background area (yellow rectangle) used for the computation of the CNR.

3.4.3 Normalized Root Mean Square Error (NRMSE)

The Normalized Root Mean Square Error (NRMSE) quantifies the reconstruction error with respect to a reference image. The NRMSE index is defined as:

$$\mathrm{NRMSE} = \frac{\|\boldsymbol{I}_{\text{test}} - \boldsymbol{I}_{\text{ref}}\|_2}{\|\boldsymbol{I}_{\text{ref}}\|_2} \tag{3.7}$$

where $\boldsymbol{I}_{\text{test}}$ and $\boldsymbol{I}_{\text{ref}}$ are the test and reference images and $\|\cdot\|_2$ is the Euclidean norm. Generally, the smaller NRMSE values indicate better image quality.

In our analysis, the NRMSE was computed by using the whole reconstructed images.

3.4.4 Structural Similarity Index (SSIM)

The Structural Similarity Index (SSIM) [16] is a metric based on the human visual system. The underlying model of the method assumes that the image degradation is perceived as change in structural information. The latter is given by inter-dependencies between pixels close together. The SSIM is a *full-reference* image quality index and evaluates the similarity between two images comparing luminance, contrast and structure information. The SSIM index for a pair of windows x and y, with same size taken from a reference image and a test image, is defined as:

$$\mathrm{SSIM}(x,y) = \left[l(x,y)^{\alpha} \cdot c(x,y)^{\beta} \cdot s(x,y)^{\gamma}\right] \tag{3.8}$$

where $l(x,y)$, $c(x,y)$ and $s(x,y)$ are the luminance, contrast and structure term, respectively, and $\alpha > 0$, $\beta > 0$ and $\gamma > 0$ are parameters used to adjust the relative importance of the three components. The luminance, contrast and structure terms are defined as follows:

$$l(x,y) = \frac{2\mu_x\mu_y + C_1}{\mu_x^2 + \mu_y^2 + C_1} \tag{3.9}$$

$$c(x,y) = \frac{2\sigma_x\sigma_y + C_2}{\sigma_x^2 + \sigma_y^2 + C_2} \tag{3.10}$$

$$s(x,y) = \frac{\sigma_{xy} + C_3}{\sigma_x\sigma_y + C_3} \tag{3.11}$$

where μ_x, μ_y, σ_x, σ_y, and σ_{xy} are the local means, standard deviations and cross-covariance for windows x, y, while C_1 and C_2 are constants to stabilize the divisions. A common choice of the parameters is the following:

$$C_3 = \frac{C_2}{2}\ , \quad \alpha = \beta = \gamma = 1 \tag{3.12}$$

hence the SSIM reduce to the following form:

$$\mathrm{SSIM}(x,y) = \frac{(2\mu_x\mu_y + C_1)(2\sigma_{xy} + C_2)}{(\mu_x^2 + \mu_y^2 + C_1)(\sigma_x^2 + \sigma_y^2 + C_2)}\ . \tag{3.13}$$

A global SSIM is given by the average of the SSIM values computed for each pair of windows. The SSIM value ranges from -1 to 1, a higher value indicates superior image quality.

In our analysis, the SSIM was computed by using the whole reconstructed images and we set $C_1 = 10^{-4}$ and $C_2 = 9 \cdot 10^{-4}$.

3.5 Results and Discussion

In our analysis, all FBP reconstructions were performed with the Ram-Lak filter. We have chosen for algebraic reconstruction algorithms the optimal number of iterations which gives the lowest NRMSE and the lowest FWHM jointly, in order to maximize the image sharpness and contrast. It was observed that this condition is achieved with about 100 iterations for SART and SIRT algorithms, whereas about 10 iterations are required in the case of the CGLS algorithm.

In Figure 3.6 we show a comparison of the reconstructed images, representing the hole B (Figure 3.1a), obtained by means of the FBP, SIRT, SART and CGLS reconstruction algorithms for different number of projections and scintillator thicknesses. The pixel values histogram is represented below each image. We note from a visual inspection that the image quality of the FBP reconstructions becomes very poor by reducing the number of projections. The pixel values histogram tends to be unimodal and the resulting image noise makes the segmentation not feasible. On the other hand, in the case of limited data reconstruction, SIRT, SART and CGLS algorithms provide clearer images and higher contrast than the FBP method. When all projections are available ($N = 1125$) the FBP reconstructions outperforms SART ones. The SIRT and CGLS algorithms, in the case $N = 1125$, gives reconstructed images characterized by higher image contrast than FBP algorithm. However, some unwanted blurring is visible in such SIRT and CGLS images if compared with FBP ones.

The image contrast and the edge quality were quantitatively evaluated by means of the CNR and FWHM. Such indexes are represented as a function of the number of projections and for different scintillator thicknesses in Figure 3.7 and Figure 3.8.

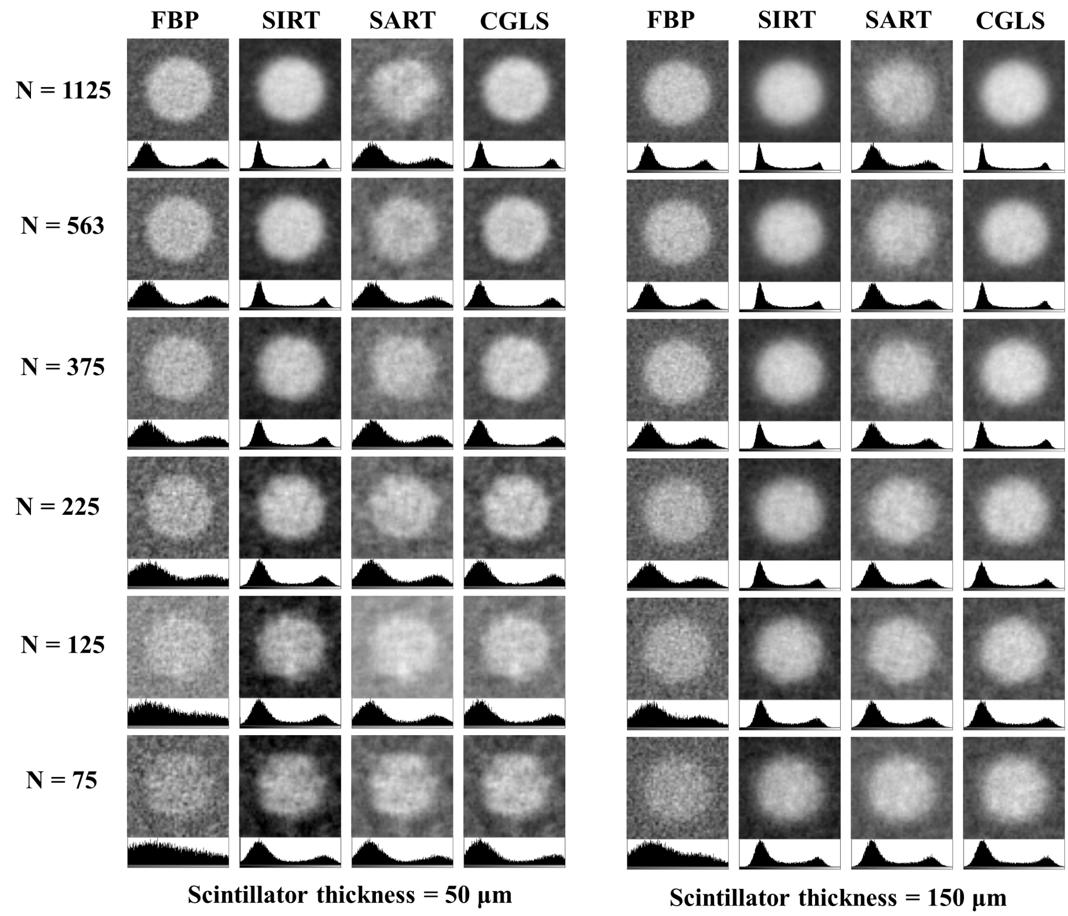

Figure 3.6: A comparison of reconstructed images, representing a slice of the hole B (with diameter $\Phi_B = 2$ mm, see Figure 3.1a), obtained using FBP, SIRT, SART and CGLS reconstruction algorithms, as a function of the number of projections N and for different scintillator thicknesses. Below each image, the grey value histogram is represented in the range $[0, 0.54]$ cm^{-1}.

As expected we observe that higher CNR and FWHM values were obtained with the thicker scintillator, regardless of the reconstruction algorithm performed. Hence, by increasing the scintillator thickness the CNR becomes higher, due to increased conversion efficiency, but there is a loss of spatial resolution. We note that the standard deviation of FWHM of the FBP images increases when the number of projections is reduced. This occurs because the noise and the aliasing artefacts cause an increase of the fitting parameters variance. The CNR of FBP reconstructions drops down and becomes inadequate for analysis when the number of projections is low. Conversely, SART, SIRT and CGLS show better image contrast than the FBP algorithm for lower number of projections. In particular, the SIRT and CGLS reconstructions have

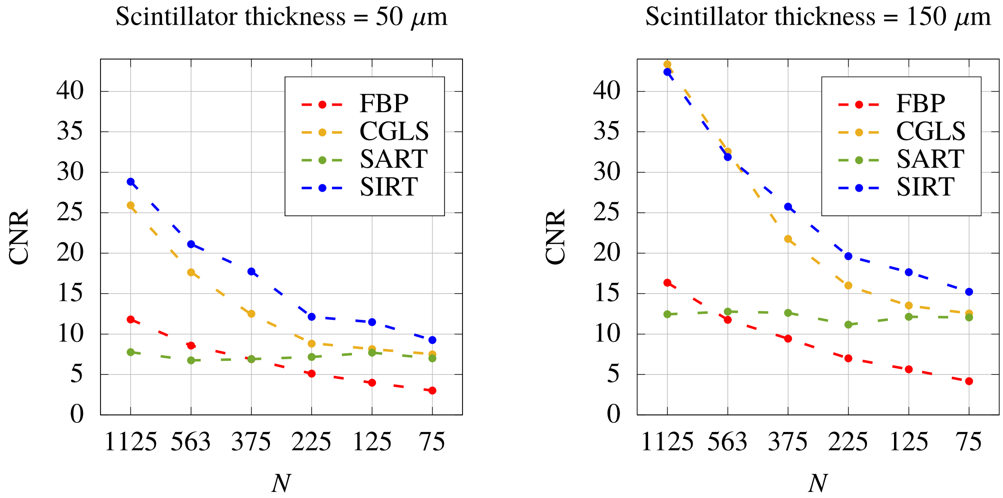

Figure 3.7: Comparison of the CNR values computed from the ROIs (Figure 3.5) of the reconstructed images obtained using FBP, SIRT, SART and CGLS algorithms, as a function of the number of projections N and for different scintillator thicknesses.

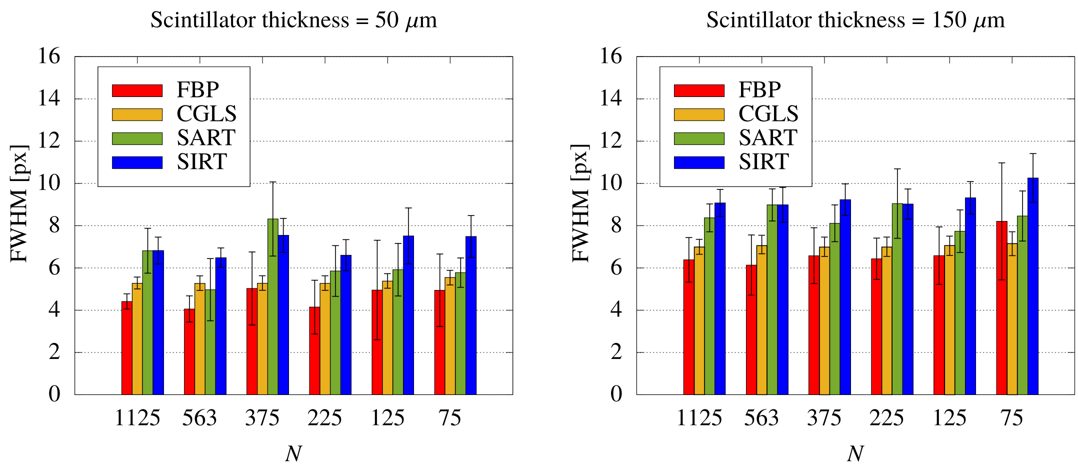

Figure 3.8: Comparison of the FWHM values computed from the reconstructed images obtained with FBP, SIRT, SART and CGLS algorithms, as a function of the number of projections N and for different scintillator thicknesses.

always higher CNR values than FBP, also in the case where the Nyquist condition is satisfied (Figure 3.7). However, FWHM plots in Figure 3.8 show that the edge quality for the SIRT algorithm is lower than FBP, but the standard deviation of FWHM is quite constant when the number of projections is reduced. On the other hand, the FWHM values of CGLS images is slightly higher than the values of FBP images (Figure 3.8). Consequently, we observe that the CGLS algorithm provides the better compromise between contrast and resolution, since it produces images with high CNR and edge quality comparable to FBP.

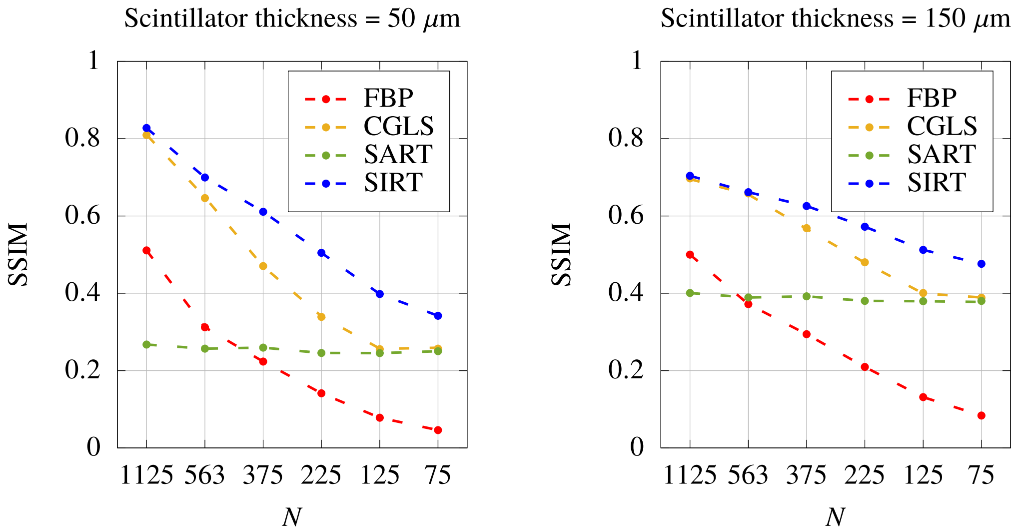

Figure 3.9: Comparison of the SSIM values computed from the reconstructed images obtained using FBP, SIRT, SART and CGLS algorithms with respect to the reference image (Figure 3.2b), as a function of the number of projections N and for different scintillator thicknesses.

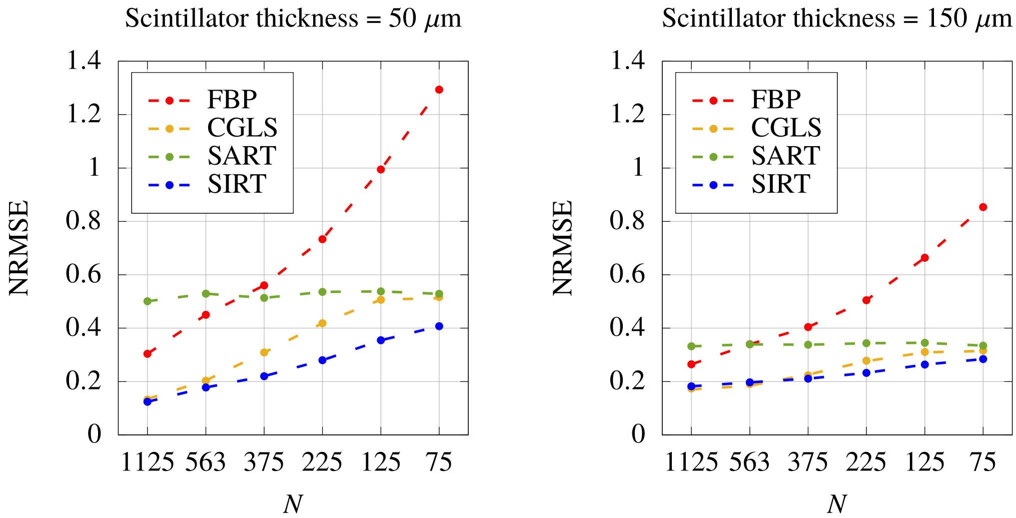

Figure 3.10: Comparison of the NRMSE values computed from the reconstructed images obtained using FBP, SIRT, SART and CGLS algorithms with respect to the reference image (Figure 3.2b), as a function of the number of projections N and for different scintillator thicknesses.

In Figure 3.9 and Figure 3.10 the SSIM and the NRMSE indexes are represented, respectively, as a function of the number of projections and for different scintillator thicknesses. We remind that lower NRMSE and higher SSIM indicate superior image quality. It is clear that iterative reconstruction algorithms outperform the FBP method also in terms of the SSIM and NRMSE indexes when the number of projection is reduced.

To better understand the quality of the reconstructed images in terms of the edge quality and image contrast, we provide in Figure 3.11 and Figure 3.12 the CNR as a function of the FWHM for different number of projections and scintillator thicknesses.

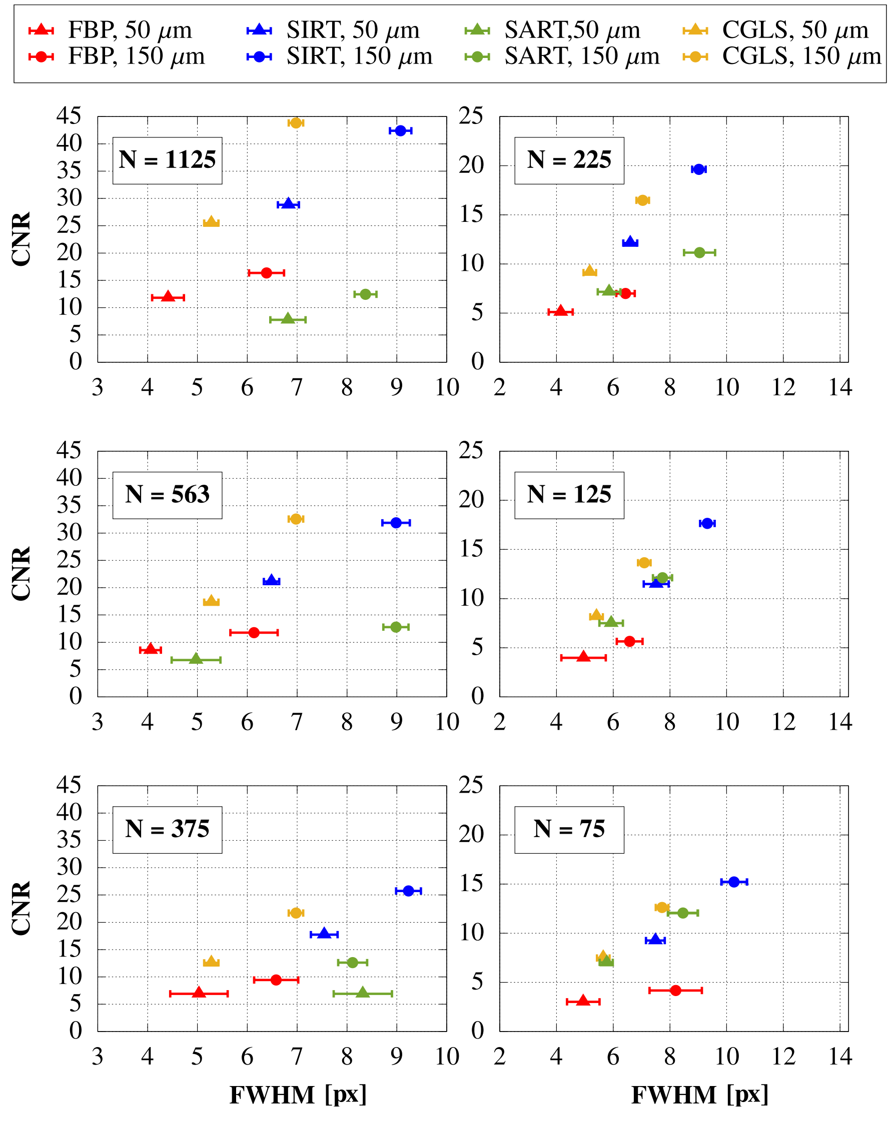

Figure 3.11: CNR as a function of the FWHM for different number of projections and for the scintillator thicknesses of 50 μm and 150 μm.

For few projections ($N = 75$ and $N = 125$) the CGLS and SART with the scintillator 50 μm thick (yellow and green triangle, respectively, in Figure 3.11) gives the better results in terms of spatial resolution and image contrast.

Furthermore, we observe from Figure 3.12 that the CGLS reconstruction with $N =$

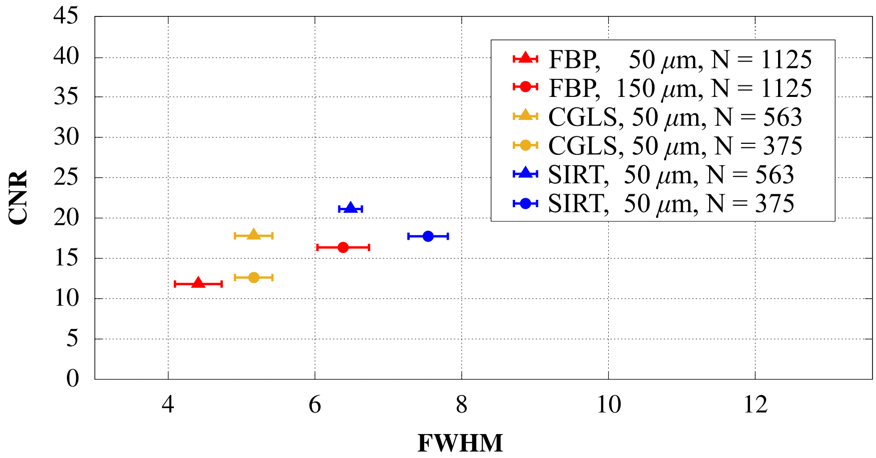

Figure 3.12: CNR as a function of the FWHM for particular FBP, SIRT and CGLS reconstructions.

563 and scintillator 50 μm thick (yellow triangle) outperforms the FBP reconstruction with $N = 1125$ and scintillator 150 μm thick (red circle) in terms of CNR and FWHM indexes. In addition, the SIRT reconstruction with $N = 563$ and scintillator 50 μm thick (blue triangle) has comparable edge quality and better contrast with respect to the FBP reconstruction with $N = 1125$ and scintillator 150 μm thick (red circle). Consequently, we can state that better image quality with respect to standard FBP reconstruction of a complete dataset ($N = 1125$) with scintillator 150 μm thick can be achieved by using the thinner scintillator (50 μm) and exploiting CGLS and SIRT algorithms with half of the projections. With 1/3 of projections and scintillator 50 μm thick, the CGLS reconstruction (yellow circle in Figure 3.12) shows comparable image contrast to FBP reconstruction of 1125 projections with scintillator 50 μm thick (red triangle) but slightly lower edge quality.

Finally, we performed two experiments with simulated data in order to compare the FBP, SIRT, SART and CGLS algorithms in terms of the reconstruction time. In the first experiment, we generated projections of a simulated phantom image and we evaluated the reconstruction time per slice as a function of the number of projections and for each reconstruction algorithm. The size of reconstructed slices was set to 1500×1500, hence we fixed side length to $n_d = 1500$ in order to study the reconstruction time as a function of the number of projections N. We performed 100 iterations for each

N	Reconstruction time [s]			
	FBP	CGLS	SART	SIRT
100	0.014	0.459	0.114	0.355
300	0.024	0.975	0.119	0.883
500	0.038	1.497	0.124	1.424
700	0.055	2.016	0.128	1.963
900	0.069	2.555	0.133	2.524
1100	0.088	3.099	0.140	3.068
1300	0.106	3.645	0.142	3.645
1500	0.121	4.207	0.151	4.235

Table 3.1: Reconstruction time as a function of the number of projections and for different reconstruction algorithms. The size of the reconstructed images is set to 1500×1500 pixels. These results are obtained by performing 100 iterations of each algebraic reconstruction algorithm.

n_d	Reconstruction time [s]			
	FBP	CGLS	SART	SIRT
100	0.043	0.165	0.042	0.118
300	0.053	0.311	0.046	0.263
500	0.056	0.586	0.052	0.537
700	0.070	0.982	0.0604	0.931
900	0.075	1.641	0.0831	1.581
1100	0.101	2.359	0.0995	2.539
1300	0.116	3.261	0.127	3.512
1500	0.114	4.258	0.149	4.492

Table 3.2: Reconstruction time as a function of image size n_d and for different reconstruction algorithms. The number of projections is set to 1500. These results are obtained by performing 100 iterations of each algebraic reconstruction algorithm.

algebraic reconstruction algorithm. The results are given in Table 3.1 and illustrated in Figure 3.13 (left). We observe that the reconstruction time increases linearly with the number of projections for each algorithm considered. As expected, the FBP outperforms the algebraic methods in the reconstruction time comparison. However, SART is the best algebraic algorithm in terms of computational efficiency, ensuring reconstruction time per slice of the order of tenths of a second. Conversely, CGLS and SIRT are more time-consuming, since reconstruction times are of the order of seconds. In the second experiment, we evaluated the reconstruction time per slice as a function of the image side length n_d and for each reconstruction algorithm. The number of projections (N) was set to 1500. Also in this case, 100 iterations were performed

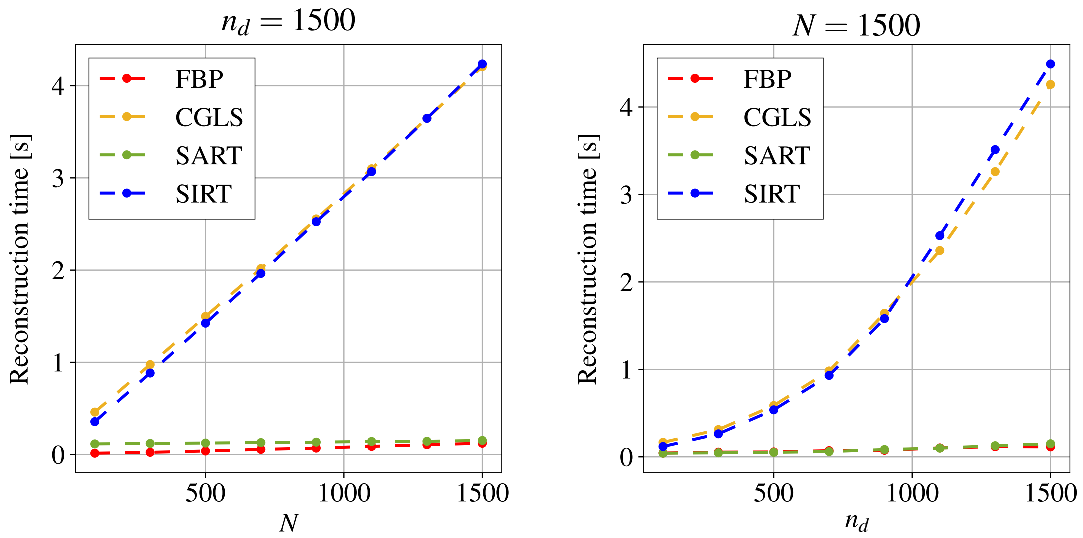

Figure 3.13: (left) Reconstruction time as a function of the number of projections for FBP, CGLS, SART and SIRT reconstruction methods. The size of the reconstructed images is set to 1500 × 1500 pixels ($n_d = 1500$). (right) Reconstruction time as a function of the image size for FBP, CGLS, SART and SIRT reconstruction methods. The number of projections N is set to 1500. These results are obtained by performing 100 iterations of each algebraic reconstruction algorithm.

for each algebraic reconstruction algorithm. The results are given in Table 3.2 and illustrated in Figure 3.13 (right). We observe that the reconstruction time increases with n_d faster than with N. However, the remarks inferred by these results are similar to the observations made for the first experiment.

The CGLS algorithm has lower computational efficiency than FBP and SART, but we underline that it provides faster convergence than SART and SIRT. In fact, we observed in our analysis that the CGLS algorithm converges with a tenth of iterations, i.e. one order of magnitude less than the iterations required by SART and SIRT. Hence, the CGLS algorithm provides sharp images with reconstruction time of the order of tenths of a second.

3.6 Conclusions

In this work the performances of different algebraic reconstruction methods (SIRT, SART and CGLS) have been tested for neutron data, and studied as a function of the number of projections and for different setups of the imaging system. The reconstructed images were quantitatively compared in terms of the image quality indexes CNR, FWHM, NRMSE and SSIM. In addition, the reconstruction times were evaluated for each algorithm.

We observe that algebraic methods provide better contrast detectability than the FBP algorithm in the case of sparse-view datasets.

The CGLS algorithm is the best compromise between spatial resolution, image contrast and reconstruction time. We demonstrated that for moderate under-sampling the CGLS and SIRT algorithms, combined with the use of thinner scintillators, provide high reconstructed image quality so much that the time of a neutron CT scan could be halved. For higher under-sampling (i.e. for datasets with less than 1/9 of the projections required by the Nyquist-Shannon condition), CGLS and SART show the best performances in terms of reconstructed image quality.

The SIRT algorithm provides reconstructions with highest image contrast in general, but at the expense of lower spatial resolution. In addition, SIRT is the slowest reconstruction algorithm, due to slow convergence and low computational efficiency. Conversely, the SART algorithm is the fastest algebraic reconstruction method and the CGLS reconstructs data with timing of the same order of magnitude, due the high convergence of such iterative algorithm.

References

[1] A. C. Kak and M. Slaney. *Principles of computerized tomographic imaging*. Society for Industrial and Applied Mathematics, 2001.

[2] Marcel Beister, Daniel Kolditz, and Willi A. Kalender. "Iterative reconstruction methods in X-ray CT". In: *Physica Medica* 28.2 (2012), pp. 94–108. ISSN: 1120-1797. DOI: 10.1016/j.ejmp.2012.01.003.

[3] Fang Xu and K. Mueller. "Accelerating popular tomographic reconstruction algorithms on commodity PC graphics hardware". In: *IEEE Transactions on Nuclear Science* 52.3 (2005), pp. 654–663. ISSN: 0018-9499. DOI: 10.1109/TNS.2005.851398.

[4] Vikas Singh, Lopamudra Mukherjee, Petru M Dinu, Jinhui Xu, and Kenneth R Hoffmann. "Limited view CT reconstruction and segmentation via constrained metric labeling". In: *Computer Vision and Image Understanding* 112.1 (2008), pp. 67–80. ISSN: 1077-3142. DOI: 10.1016/j.cviu.2008.06.005.

[5] Bruce F. McEwen, Kenneth H. Downing, and Robert M. Glaeser. "The relevance of dose-fractionation in tomography of radiation-sensitive specimens". In: *Ultramicroscopy* 60.3 (1995), pp. 357–373. ISSN: 0304-3991. DOI: 10.1016/0304-3991(95)00082-8.

[6] Heikki Sipila. "Moving-object computer tomography for luggage inspection". In: *Proc. SPIE* 1824 (1993), pp. 39–40. DOI: 10.1117/12.142902.

[7] Sherman J. Kisner, Eri Haneda, Charles A. Bouman, Sondre Skatter, Mikhail Kourinny, and Simon Bedford. "Limited view angle iterative CT reconstruction". In: *Proc. SPIE* 8296 (2012). DOI: 10.1117/12.917781.

[8] T. Minniti, W. Kockelmann, G. Burca, J.F. Kelleher, S. Kabra, S.Y. Zhang, D.E. Pooley, E.M. Schooneveld, Q. Mutamba, J. Sykora, N.J. Rhodes, F.M. Pouzols, J.B. Nightingale, F. Aliotta, L.M. Bonaccorsi, R. Ponterio, G. Salvato, S. Trusso, C. Vasi, A.S. Tremsin, and G. Gorini. "Materials analysis opportunities on the new neutron imaging facility IMAT@ISIS". In: *Journal of Instrumentation* 11.03 (2016). DOI: 10.1088/1748-0221/11/03/C03014.

[9] Winfried Kockelmann, Genoveva Burca, Joe F. Kelleher, Saurabh Kabra, Shu-Yan Zhang, Nigel J. Rhodes, Erik M. Schooneveld, Jeff Sykora, Daniel E. Pooley, Jim B. Nightingale, Francesco Aliotta, Rosa C. Ponterio, Gabriele Salvato, Dario Tresoldi, Cirino Vasi, Jason B. McPhate, and Anton S. Tremsin. "Status of the Neutron Imaging and Diffraction Instrument IMAT". In: *Physics Procedia* 69.Supplement C (2015). Proceedings of the 10th World Conference on Neutron Radiography (WCNR-10) Grindelwald, Switzerland October 5–10, 2014, pp. 71–78. ISSN: 1875-3892. DOI: 10.1016/j.phpro.2015.07.010.

[10] Triestino Minniti, Kenichi Watanabe, Genoveva Burca, Daniel E. Pooley, and Winfried Kockelmann. "Characterization of the new neutron imaging and materials science facility IMAT". In: *Nuclear Instruments and Methods in Physics Research Section A: Accelerators, Spectrometers, Detectors and Associated Equipment* 888 (2018), pp. 184–195. ISSN: 0168-9002. DOI: 10.1016/j.nima.2018.01.037.

[11] A. P. Kaestner. "MuhRec - A new tomography reconstructor". In: *Nuclear Instruments and Methods in Physics Research, Section A: Accelerators, Spectrometers, Detectors and Associated Equipment* 651.1 (2011), pp. 156–160. ISSN: 01689002. DOI: 10.1016/j.nima.2011.01.129.

[12] B. Münch, P. Trtik, F. Marone, and M. Stampanoni. "Stripe and ring artifact removal with combined wavelet-Fourier filtering". In: *Optics Express* 17.10 (2009), p. 8567. ISSN: 1094-4087. DOI: 10.1364/OE.17.008567.

[13] A. H. Andersen and A. C. Kak. "Simultaneous Algebraic Reconstruction Technique (SART): A Superior Implementation of the Art Algorithm". In: *Ultrasonic Imaging* 6.1 (1984), pp. 81–94. DOI: 10.1177/016173468400600107.

[14] Peter Gilbert. "Iterative methods for the three-dimensional reconstruction of an object from projections". In: *Journal of Theoretical Biology* 36.1 (1972), pp. 105–117. ISSN: 10958541. DOI: 10.1016/0022-5193(72)90180-4.

[15] John a. Scales. "Tomographic inversion via the conjugate gradient method". In: *Geophysics* 52.2 (1987), p. 179. ISSN: 1070485X. DOI: 10.1190/1.1442293.

[16] Zhou Wang, Alan C. Bovik, Hamid R. Sheikh, and Eero P. Simoncelli. "Image Quality Assessment: From Error Visibility to Structural Similarity". In: *IEEE Transactions on Image Processing* 13.4 (2004), pp. 600–612. DOI: 10.1109/TIP.2003.819861.

[17] Sara Mohammadi, Emanuel Larsson, Frauke Alves, Simeone Dal Monego, Stefania Biffi, Chiara Garrovo, Andrea Lorenzon, Giuliana Tromba, and Christian Dullin. "Quantitative evaluation of a single-distance phase-retrieval method applied on in-line phase-contrast images of a mouse lung". In: *Journal of Synchrotron Radiation* 21.4 (2014), pp. 784–789. DOI: 10.1107/S1600577514009333.

[18] Marijke Welvaert and Yves Rosseel. "On the Definition of Signal-To-Noise Ratio and Contrast-To-Noise Ratio for fMRI Data". In: *PLoS ONE* 8.11 (Nov. 2013). Ed. by Essa Yacoub, e77089. DOI: 10.1371/journal.pone.0077089.

[19] Tao Wu, Richard H. Moore, Elizabeth A. Rafferty, and Daniel B. Kopans. "A comparison of reconstruction algorithms for breast tomosynthesis". In: *Medical Physics* 31.9 (Aug. 2004), pp. 2636–2647. DOI: 10.1118/1.1786692.

Dolcemente viaggiare, rallentando per poi accelerare...

— Lucio Battisti, from the song "Sì, viaggiare"

4

Artificial Neural Network based reconstruction for Neutron Tomography

Contents

This chapter is based on:

D. Micieli, T. Minniti, Ll. M. Evans and G. Gorini. "Accelerating Neutron Tomography experiments through Artificial Neural Network based reconstruction". In: *Scientific Reports* 9 (Feb. 2019). DOI: 10.1038/s41598-019-38903-1.

4.1 Introduction

NT is a useful tool for evaluating the structural integrity of objects but it is very time-consuming, so scanning a set of similar objects during a beamtime leads to data redundancy and long acquisition times. Nowadays NT is unfeasible for quality checking study of large quantities of similar objects. Hence, in the NI field there is great interest in the optimization of time usage at neutron beamlines, motivated also by the high neutrons production cost.

One way to reduce the CT scan time is to limit the number of projections. In Chapter 3 we demonstrated that conventional algebraic methods better handle sparse-view neutron datasets with respect to the widely used FBP algorithm. In addition, a wide variety of *regularized iterative methods* have been proposed in literature [1–5]. This class of reconstruction algorithms involve additional regularizing terms in the objective function. The prior knowledge about the scanned sample is embedded in a regularizing term, providing accurate reconstruction from high under-sampled datasets. Although regularized iterative methods generally outperform analytical ones to handle limited-data problems, they present two major drawbacks. The first is the high computational cost, several order of magnitude greater than analytical methods and even higher than algebraic methods. For example, a Total Variation (TV) minimization based reconstruction of a 1024^3 volume performed on GPU it would take more than a day of computation. The second disadvantage is the limited variety of samples that can be reconstructed, due the constrain imposed by the specific prior knowledge. For example, TV minimization based methods can be used only to accurately reconstruct objects with sparse gradient. For this reasons, the application of regularized iterative methods to large-scale tomographic data is still limited.

Nowadays, Deep Learning [6] (DL) has reached state-of-the-art performance for image classification [7–9], segmentation [10–12], image denoising [13–15], deconvolution [16] and artifact reduction [17, 18]. Recently, new Machine Learning (ML) based methods were introduced to improve low-dose and Sparse-View X-ray tomography

[19–26]. These methods are data-driven, i.e. they learn the image features from training data providing more accurate reconstructions than analytical methods.

In this work we propose the recently introduced Neural Network Filtered Back-Projection (NN-FBP) method [27] to reduce the acquisition time in NT experiments. At the best of our knowledge, this is the first study which proposes and tests a ML based reconstruction method for NT. The NN-FBP method avoids to a degree the aforementioned problems of analytical and iterative reconstruction algorithms. In fact, NN-FBP is faster than iterative methods, since it has similar computation complexity to FBP, and learns how to use problem specific knowledge, providing high image quality even for limited datasets. We demonstrate that this method is suitable for neutron data and outperforms conventional reconstruction methods used in NT. Furthermore, the NN-FBP method can reliably reduce the scan time, reconstruction time and the amount of data storage. As case study, we chose to inspect part of a monoblock (Figure 4.1) from the divertor region of a fusion energy device by means of sparse-view NT and the NN-FBP reconstruction algorithm. The main motivation of employing the fusion divertor monoblock as a specimen is because of the large number of armour that will be required for the divertor assembly within the ITER project [28] and consequently matches the need of a quality check technique. The structural integrity of these samples subjected to high thermal loads is fundamental within a tokamak fusion energy device. A comparative study between X-ray CT and NT has been recently carried out [29] to inspect the quality of manufactured monoblocks.

In our work, simulated and real neutron data were used to assess the performances of the NN-FBP, FBP and SIRT [30] methods as a function of the number of projections. The reconstructed images were quantitatively compared in terms of several image quality indexes.

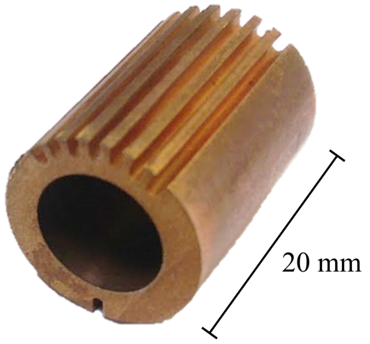

Figure 4.1: The sample inspected using NT. The Cu-CuCrZr pipe is the central section of the Culham Centre for Fusion Energy thermal break concept monoblock.

4.2 Methods

4.2.1 Overview of the approach

The NN-FBP method is based on a nonlinear weighted sum of different FBP reconstructions, each of these with a specific filter. An Artificial Neural Network (ANN) model is exploited to train these custom filters. The type of network used for the NN-FBP is the multilayer perceptron [31]. This network has three layers: the input layer, the hidden layer and the output layer, each of them composed of n, N_h and m nodes, respectively. In a multilayer perceptron, each input node is connected to all hidden nodes with a weight w_{ij}, and each hidden node to all output nodes with a weight q_{ij}. Hence, the connections between the input layer and the hidden layer is described by the $n \times N_h$ matrix $\boldsymbol{W}$, containing the w_{ij} weights. The $m \times N_h$ matrix $\boldsymbol{Q}$ containing the weights q_{ij} represents the connections between the hidden nodes and the output nodes. Scalar values are subtracted from the output of each hidden and output node. Moreover, a logistic function $\sigma(t) = \frac{1}{1+e^{-t}}$ is applied as activation function to the output of each hidden and output node, making the neural network a nonlinear model. The number of hidden nodes N_h is a free parameter, to be determined for each specific problem. The output vector $\boldsymbol{O}$ of a multilayer perceptron, with N_h number of hidden nodes, for the input vector $\boldsymbol{z}$ can be expressed as:

$$\boldsymbol{O}_{\boldsymbol{Q},\boldsymbol{W},\boldsymbol{b},\boldsymbol{b}_0}(\boldsymbol{z}) = \sigma\left(\sum_{i=1}^{N_h} \boldsymbol{q}_i \sigma(\boldsymbol{w}_i \cdot \boldsymbol{z} - \boldsymbol{b}_i) - \boldsymbol{b}_0\right) \tag{4.1}$$

where $\boldsymbol{w_i}$ and $\boldsymbol{q_i}$ are single columns of the matrices $\boldsymbol{W}$ and $\boldsymbol{Q}$ respectively, while $\boldsymbol{b_i}$ and $\boldsymbol{b_0}$ are the bias weights. According to supervised learning approach, an unknown function can be approximated by an ANN if the output values $\boldsymbol{f_i}$ are known for a particular set of T input vectors $\boldsymbol{z_i}$. Hence, the network weights are found in a training task that consists in minimize the cost function:

$$e(\boldsymbol{Q}, \boldsymbol{W}, \boldsymbol{b}, \boldsymbol{b}_0) = \sum_{i=1}^{T} (\boldsymbol{O}(\boldsymbol{z}_i) - \boldsymbol{f}_i)^2. \tag{4.2}$$

In the case of the NN-FBP, the input vector has the same size of the detector array, composed of N_d elements each with coordinate τ_d. The input vector components can be expressed as follows:

$$z(\tau_d) = \sum_{k=1}^{N_{\text{proj}}} P_{\theta_k}(x_i \cos\theta_k + y_i \sin\theta_k - \tau_d) \tag{4.3}$$

while output layer is composed of a single node and described by the formula:

$$O_{\boldsymbol{Q},\boldsymbol{W},\boldsymbol{b},b_0}(\boldsymbol{z}) = \sigma\left(\sum_{j=1}^{N_h} q_j \sigma(FBP_{\boldsymbol{w}_j}(x_i, y_i) - \boldsymbol{b}_j) - b_0\right). \tag{4.4}$$

The output of this neural network can be viewed as weighted sum of N_h FBP reconstructions with custom filters and specific biases. Hence, the computational complexity of the NN-FBP method depends on the number of hidden nodes N_h, but is comparable to the FBP method.

4.2.2 Sample

Fabrication of the Cu-CuCrZr pipe, shown in Figure 4.1, was carried out in the following way. Firstly, the inner CuCrZr pipe with a thickness of 1 mm was wrapped in three turns of a 25 μm thick braze foil to a total thickness of 75 μm. The braze foil is a 50:50 copper-gold mix known commercially as Orobraze™. Next, two half copper pipe ‘sleeves’ were placed around the inner pipe. The sleeves were held in place by tying them with a molybdenum wire in several locations along the length of the pipe. This assembly was heated in a vacuum furnace to perform the brazing cycle and join the inner and outer pipes. Finally, the molybdenum wire was removed, and 1 mm wide grooves were machined along the length of the copper pipe; one groove along one side and seven equidistant grooves on the opposing side. For the purpose of this investigation, a length of 20 mm pipe was cut from a longer part.

4.2.3 Data acquisition at the IMAT beamline

The data acquisition was carried out at the IMAT beamline [32–34], ISIS neutron spallation source, Rutherford Appleton Laboratory, U.K. The sample was placed on the rotating platform at the distance $L = 10$ m from the beam aperture and at the distance $d = 25$ mm from the scintillator screen. The diameter of the beam aperture was $D = 40$ mm, resulting in a L/D ratio of 250. The neutron flux for this setup is $5.9 \cdot 10^6$ n/cm^2/s [33]. The imaging system consisted of a CMOS camera with 2048 $\times$ 2048 pixels coupled with optical lenses and a scintillator ^{6}LiF/ZnS with thickness 50 μm. The FOV was set to 59.5 $\times$ 59.5 mm^2 and the resulting pixel size was 29 μm. Each tomographic scan was performed by collecting a set of 1335 radiographs in the angular range [0°, 360°), with an exposure time of 30 s per projection (the maximum allowed by the used camera) and an overall scan time of approximately 11 hours. Open beam and dark field images were taken as well in order to perform the data normalization. Our setup provides a number of neutrons per pixel equals to $1.5 \cdot 10^3$.

4.2.4 Data processing and reconstruction

The acquired raw projections were normalized respect to the dark images, open beam images and to the neutron dose. Afterwards, the normalized projections were pre-processed by removing dead-pixels and gamma-spots, while ring artifacts were suppressed by means of a filter based on combined wavelet and Fourier analysis [35].

In the simulation experiment, we generated images of 3480$\times$3480 pixels representing a slice of the sample (Figure 4.2). We evaluated equispaced projections in the angular range $[0, 2\pi)$ for a detector with 3480 pixels. We assumed a parallel beam geometry which is a fair approximation for neutron beams characterized by an L/D ratio of 250. Afterwards, we rebinned the projected data to 870 pixels and we added Poisson noise assuming 5000 counts as background intensity. The reconstruction was done on a 870 $\times$ 870 pixels grid. Pre-processing, reconstruction and analysis of simulated

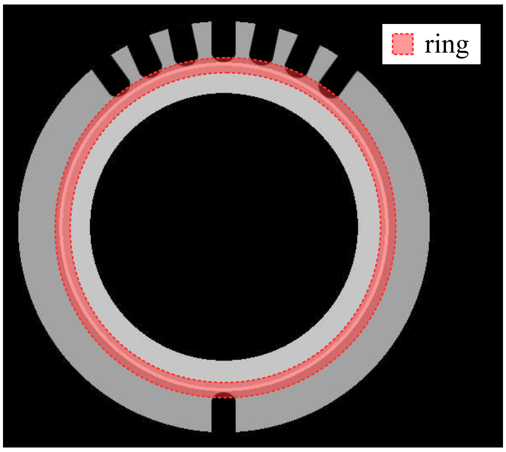

Figure 4.2: Diagram showing a slice of the simulated phantom and the ring-shaped ROI (red area) used for the computation of the NRMSE.

and real data were carried out by means of the NeuTomPy toolbox, a new Python package for tomography, which is presented in Chapter 5.

All reconstructions and simulations were performed on a Linux workstation equipped with an Intel Core i7-6700HQ CPU @ 3.40GHz CPU, 64 GB of system RAM and a NVIDIA GTX TITAN X GPU.

4.3 Results

The NN-FBP method combines different FBP reconstructions, each with a custom filter, to produce a single image. The filters are determined by training an ANN. The network input is a vector that contains the projection data and the network output is a single reconstructed pixel. The intermediate hidden layer of the network consists of N_h hidden nodes. This parameter can be chosen freely and, in the NN-FBP implementation, represents the number of different FBP reconstructions to compute and combine in a single image. We used simulated data to find the optimal value of N_h which ensures the best balance between reconstructed image quality and reconstruction time. We underline that the network must be re-trained to change the number of hidden nodes.

Afterwards, we quantitatively compared the NN-FBP, FBP and SIRT methods as a function of the number of projections using both simulated and real data. The evaluation of the image quality was carried out by computing the Normalized Root

Mean Square Error (NRMSE), the Structural Similarity Index (SSIM) [36], the Feature Similarity Index (FSIM) [37] and the Gradient Magnitude Similarity Deviation (GMSD) [38]. The NRMSE is a measure of the reconstruction error and it was computed by using the following definition:

$$\mathrm{NRMSE} = \frac{||I_{\mathrm{rec}} - I_{\mathrm{gt}}||_2}{||I_{\mathrm{gt}}||_2} \tag{4.5}$$

where I_{rec} and I_{gt} are vectors containing pixel values of the reconstructed and ground truth image, respectively, $||\cdot||_2$ is the Euclidean norm. In our analysis, the NRMSE was computed both on the sample (NRMSE sample) and on a ring-shaped region of interest (NRMSE ring) shown in Figure 4.2 in order to evaluate the reconstruction accuracy of a particular thin feature of the sample. The sample mask was computed using the Otsu's thresholding method [39]. The SSIM index quantifies the structural similarity between two images by comparing the luminance, the contrast and the structure information. The SSIM value ranges from -1 to 1, a higher value indicates superior image quality. The FSIM is an image quality index that better reflects the perception of the human visual system evaluating salient low-level image features. In fact, FSIM index exploits the phase congruency and the image gradient magnitude, which are complementary features in characterizing the image quality. The FSIM value ranges from 0 to 1, a higher value indicates superior image quality. The GMSD index measures the variation in the similarity of gradient maps between two images. We used this metric to assess the quality of the edges. GMSD values lie between 0 and 1, a value closer to 0 indicates better similarity in the gradient maps.

4.3.1 Simulation study

A numerical phantom, which mimics the Cu-CuCrZr pipe (Figure 4.1), was generated to find optimal parameters for the reconstruction and to test the NN-FBP method. A slice of the numerical phantom is shown in Figure 4.2. Simulated projections were obtained by computing the Radon Transform of the phantom image, assuming a parallel beam geometry. First, we reconstruct images from an over-sampled dataset of 1335 projections using the SIRT method with 400 iterations. The over-sampled dataset contains twice the number of projections required by the Nyquist-Shannon condition. In fact, the sampling theorem is exactly satisfied for 668 projections (the widest horizontal dimension of the sample is ~ 430 pixels long). We then train the ANN to mimic the reconstructed images obtained from the oversampled dataset, using a subset of the available projections. The network was trained on 10^5 pixels/slice from 10 training images and 10^5 pixels/slice from 10 validation images. The image quality indexes were evaluated on 30 reconstructed images of a numerical phantom that differs from spatial orientation from the one used for training. We used the original phantom images as ground truth image.

Firstly, we evaluated the quality of the NN-FBP reconstruction for different number of hidden nodes (N_h). Figure 4.3 shows the NRMSE computed over the whole image and the reconstruction time as a function of the number of projections (N_{proj}). Each line represents reconstructions with 1, 2, 4 and 8 hidden nodes. It is clear that in general higher reconstructed image quality is achieved by increasing the number of hidden nodes, but at the expense of a longer reconstruction time. Hence, we chose to use 4 hidden nodes in both simulated and experimental study, since it ensures a good balance between image quality and short reconstruction time (less than 300 ms for under-sampled datasets).

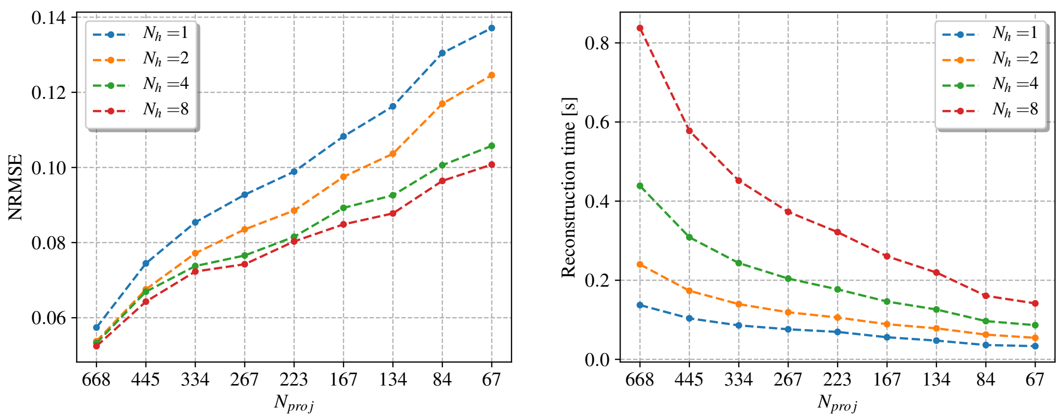

Figure 4.3: (left) The NRMSE values and (right) the reconstruction time for the number of hidden nodes 1,2,4 and 8, as a function of the number of projections.

Afterwards, we compared the reconstruction quality of the NN-FBP with respect to the quality of conventional algorithms SIRT and FBP, in terms of the aforementioned

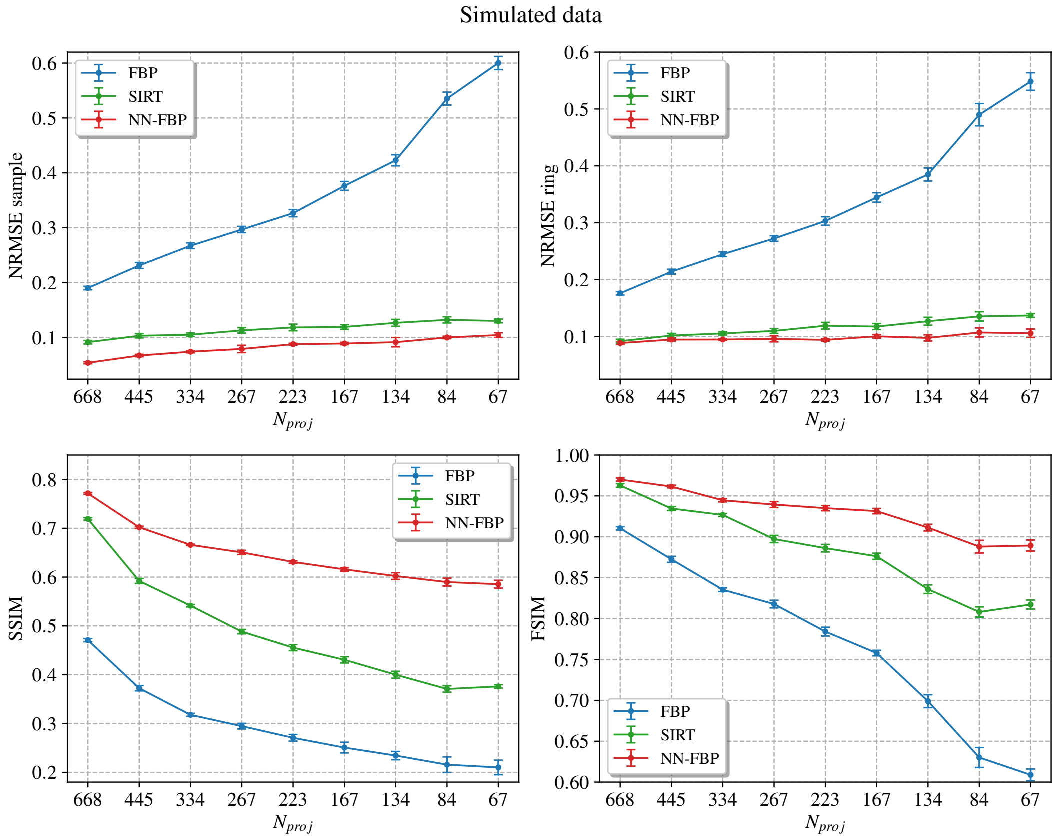

Figure 4.4: Comparison of different image quality indexes computed from FBP, SIRT and NN-FBP reconstructions of simulated data, as a function of the number of projections N_{proj}. (top-left) The NRMSE evaluated over the sample mask, (top-right) the NRMSE evaluated within the ring-shaped ROI, (bottom-left) the SSIM index and (bottom-right) the FSIM index. The error bars indicate three standard deviations.

indexes. In our analysis, all FBP reconstructions were performed with the Ram-Lak filter. Figure 4.4 shows the NRMSE sample (top-left), the NRMSE ring (top-right), the SSIM (bottom-left) and the FSIM (bottom-right) evaluated from FBP, SIRT and NN-FBP reconstructions of simulated data as a function of the number of projections.

It is clear that NN-FBP method outperforms significantly the FBP and SIRT. In fact, the indexes related to NN-FBP reconstructions indicate better image quality than conventional algorithms for all number of projections considered. The FSIM turns out to be the most significant image quality index. It is evident from the FSIM plot in Figure 4.4 that the number of projections can be reduced using the NN-FBP method to 134, i.e. 1/8 of the over-sampled dataset and 1/4 of the projections required by the sampling theorem, ensuring image quality comparable to FBP reconstruction for $N_{proj} = 668$.

4.3.2 Experimental study

We performed tomographic scans of two similar samples by collecting over-sampled datasets of 1335 projections in the angular range [0°, 360°). Also in this case, oversampled datasets contains twice the number of projections required by the sampling theorem. The first sample was used to train the ANNs, the latter to evaluate the image quality of the NN-FBP reconstructions. The network was trained to mimic images obtained from 1335 projections of the first sample using the SIRT method with 400 iteration. In particular, 10^5 pixels/slice from 10 training images and 10^5 pixels/slice from 10 validation images of the first sample were used to train the ANNs. We evaluated the image quality indexes on 30 reconstructed images of the second sample for each reconstruction method. At this stage, we regard as ground truth images the SIRT reconstruction of the oversampled dataset ($N_{proj} = 1335$) with 400 iterations.

Figure 4.5 shows the NRMSE sample (top-left), the NRMSE ring (top-right), the SSIM (bottom-left) and the FSIM (bottom-right) evaluated from FBP, SIRT and NN-FBP reconstructions of real data as a function of the number of projections. In general, the trend of each index obtained in the experimental study is quite similar to the results of the simulation study. In fact, the NN-FBP shows higher image quality than FBP and SIRT in terms of the NRMSE sample, SSIM and FSIM for all numbers of projections. From the NRMSE ring plot, we deduce that NN-FBP method provides at worst reconstruction comparable for accuracy to the SIRT. From the FSIM plot in Figure 4.5 we conclude that the number of projections can be reduced using the NN-FBP method to 223, i.e. 1/6 of the over-sampled dataset and 1/3 of the projections required by the sampling theorem, ensuring image quality comparable to standard FBP reconstruction for $N_{proj} = 668$.

In Figure 4.6 we show a comparison of different reconstructed slices: the ground truth image, the FBP and SIRT reconstruction of 668 projection, matching exactly the Nyquist condition, and the FBP, SIRT and NN-FBP reconstruction for 223 and 67 projections. Below each image is shown the intensity profile along a line segment marked

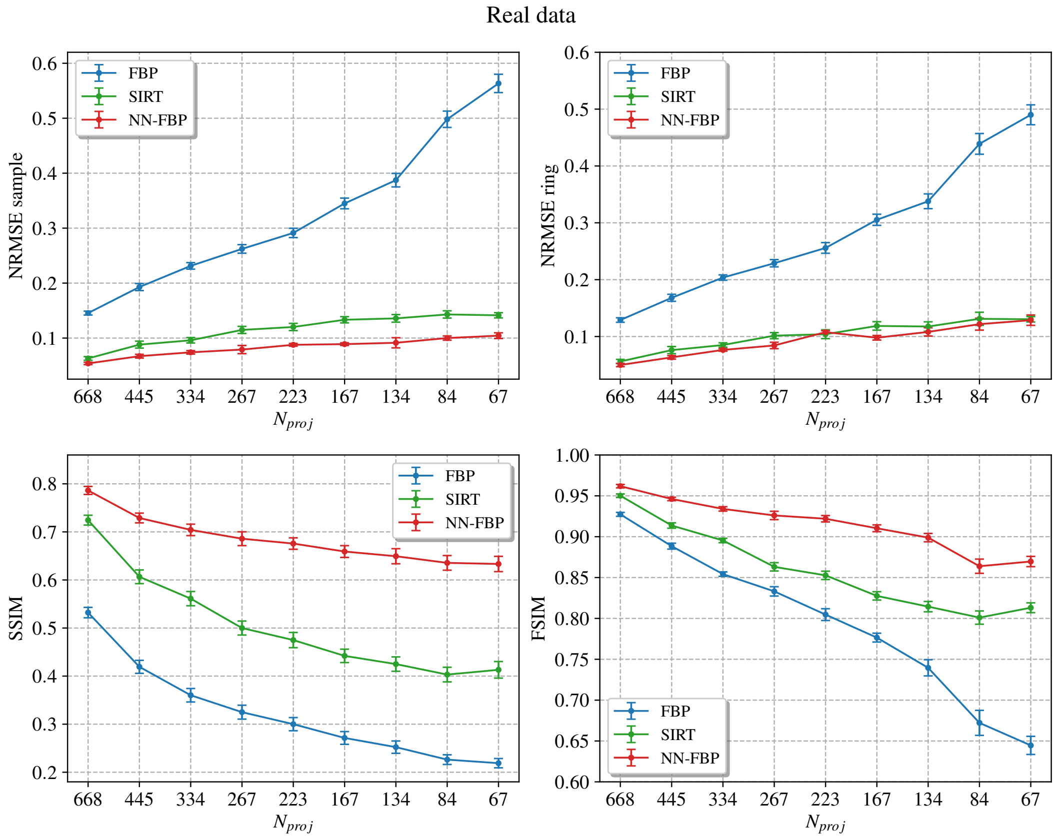

Figure 4.5: Comparison of different image quality indexes computed from FBP, SIRT and NN-FBP reconstructions of real data, as a function of the number of projections N_{proj}. (top-left) The NRMSE evaluated over the sample mask, (top-right) the NRMSE evaluated within the ring-shaped ROI, (bottom-left) the SSIM index and (bottom-right) the FSIM index. The error bars indicate three standard deviations.

in each CT slice with a red dashed line. Furthermore the histogram of attenuation coefficients within the sample mask is represented below each intensity profile plot. We note from a visual inspection that for 223 projections the FBP reconstruction is affected by high noise dose which makes the segmentation not feasible. On the other hand, the NN-FBP method with 223 projection provides high contrast images and less noise than conventional algorithms. Furthermore, we note that the NN-FBP for $N_{proj} = 223$ is the only one method able to reconstruct images with a multimodal distribution of the pixel values. The edges and the sample features are accurately reconstructed. This result indicates that segmentation and analysis can be actually performed on a NN-FBP reconstruction of a limited dataset with 223 projections. When the number of projection is reduced to 67 (1/10 of the required one by the

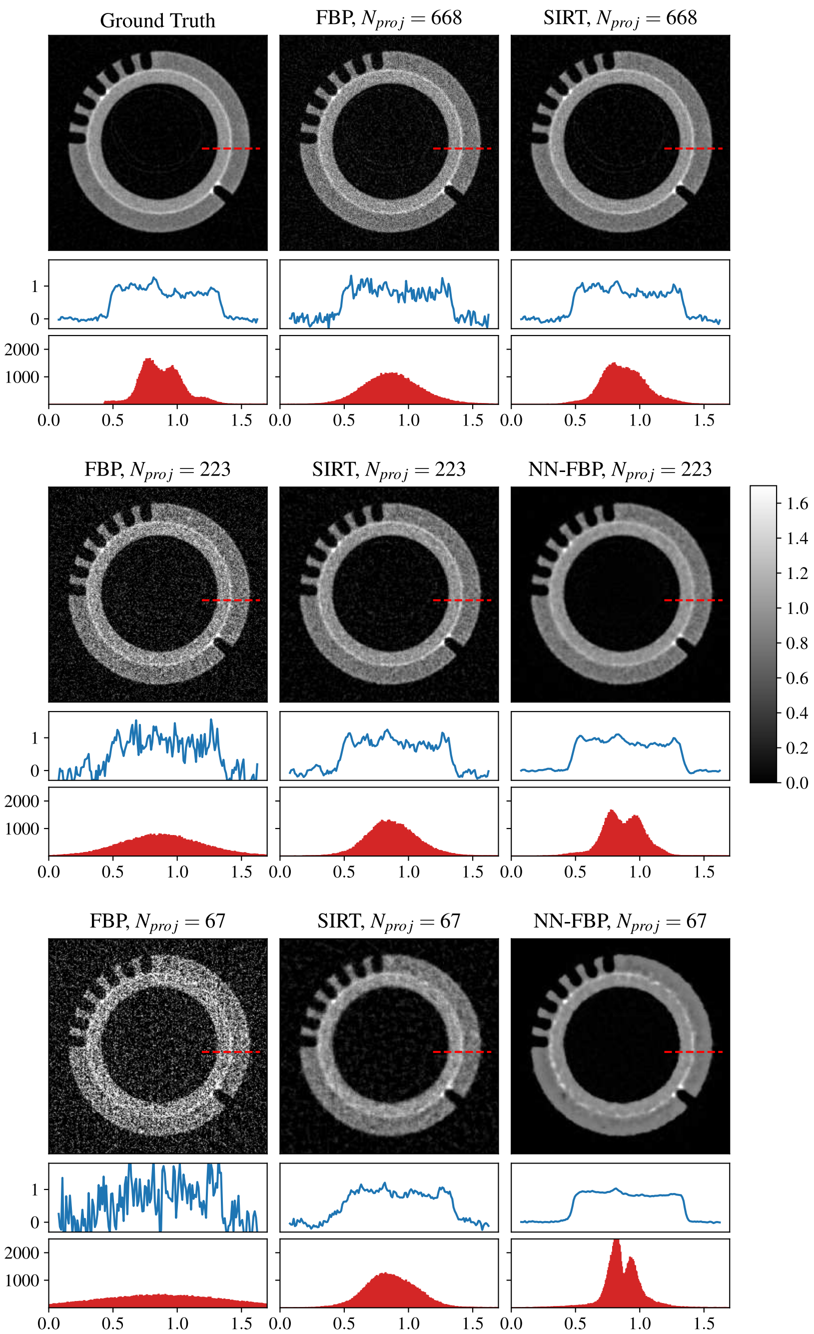

Figure 4.6: A comparison of CT reconstructed images of real data obtained using FBP, SIRT and NN-FBP methods for different number of projections. In the reading order: the ground truth image obtained with SIRT algorithm ($N_{proj} = 1335$ and 400 iterations), the FBP reconstruction for $N_{proj} = 668$ (matching exactly the Nyquist condition), the SIRT reconstruction for $N_{proj} = 668$ and 400 iterations, the FBP reconstruction for $N_{proj} = 223$, the SIRT reconstruction for $N_{proj} = 223$ and 400 iterations, the NN-FBP reconstruction for $N_{proj} = 223$, the FBP reconstruction for $N_{proj} = 67$, the SIRT reconstruction for $N_{proj} = 67$ and 400 iterations, the NN-FBP reconstruction for $N_{proj} = 67$. Below each image is shown the intensity profile along a line segment marked in each CT slice with a red dashed line. The intensity values are represented in the range [-0.3, 1.8] cm^{-1} and the segment length is 160 pixels. Below each intensity profile the histogram of the attenuation coefficient values within the sample is represented in the range [0, 1.7] cm^{-1}.

sampling theorem) the NN-FBP reconstructs well the strong edges but with an over-smoothing which suppresses low contrast structure. Hence the severe under-sampling in NN-FBP method leads to low-noise images but with a loose of image features.

To assess the local structural similarity of the reconstructed images with respect to the ground truth image we computed the local SSIM map. In Figure 4.7 we show the SSIM maps related to the FBP and SIRT reconstruction of 668 projections, the FBP, SIRT and NN-FBP reconstruction of 223 projections. The histogram of local SSIM values is represented below each image and the global SSIM is also reported.

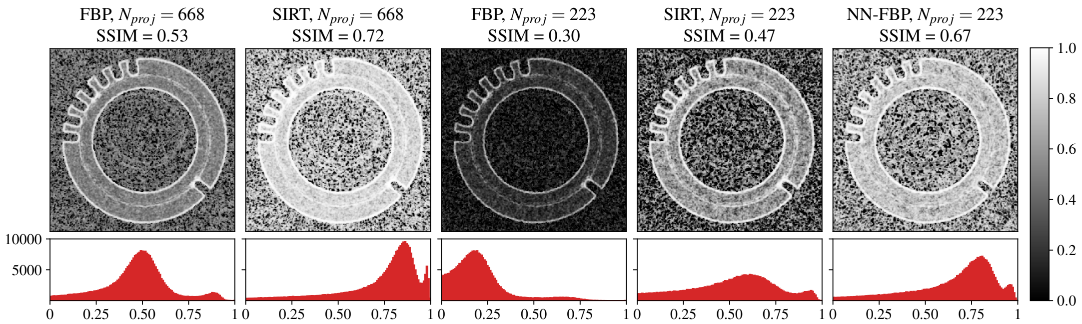

Figure 4.7: The SSIM maps computed from FBP, SIRT and NN-FBP reconstructions of real data for $N_{proj} = 668$ and $N_{proj} = 223$ with respect to the ground truth image. Below each image the histogram of local SSIM values is represented, while above the global SSIM value is reported.

We observe that in the case of the NN-FBP method with 223 projection the majority of local SSIM values range from 0.7 to 1 and globally around 0.67. This result is significantly better than the results obtained from FBP and SIRT for the same number of projections (i.e. global SSIM 0.30 and 0.47 for FBP and SIRT and majority of local SSIM values < 0.7). Furthermore, the NN-FBP reconstruction of 223 projections outperforms the standard FBP reconstruction of 668 projections in terms of local and global SSIM values. However, the SIRT reconstruction of 668 projections shows slightly better structural similarity with respect to the ground image than the NN-FBP reconstruction for 223 projections. In fact, the global SSIM for the SIRT image is 0.72 while for NN-FBP image is 0.67.

In Figure 4.8 we show a comparison of the GMSD values computed with respect to the ground truth image for each reconstruction algorithm as a function of the number of

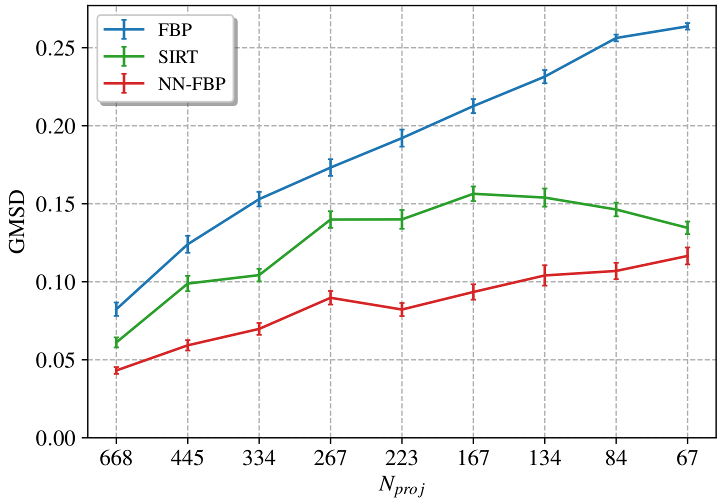

Figure 4.8: Comparison of the GMSD values computed with respect to the ground truth image from FBP, SIRT and NN-FBP reconstructions of real data as a function of the number of projections. The error bars indicate three standard deviations.

projections. We observe that for each reconstruction method the edge quality decreases when the number of projections is reduced. However, the NN-FBP outperforms SIRT and FBP in terms of the GMSD values for each number of projections considered. Furthermore, the edge quality of the NN-FBP reconstruction of 223 projections is comparable to the standard FBP reconstruction of 668 projections.

Finally, we evaluated the average reconstruction time per slice of the FBP, SIRT and NN-FBP methods as a function of the number of projections. The results are shown in Figure 4.9. The FBP method is the fastest reconstruction algorithm. However, NN-FBP is in general one order of magnitude faster than SIRT and one order of magnitude slower than FBP, ensuring reconstruction time per slice of the order of tenths of a second.

In Table 4.1 we report the training time of the NN-FBP method as a function of the number of projections and for different number of hidden nodes. Obviously the training time increases with the amount of training and validation data and in our analysis we fixed them. For each training stage we used 10^5 pixels/slice from 10 training images and 10^5 pixels/slice from 10 validation images. We observe from Table 4.1 that the training time increases with the N_h value but does not strictly depend on the

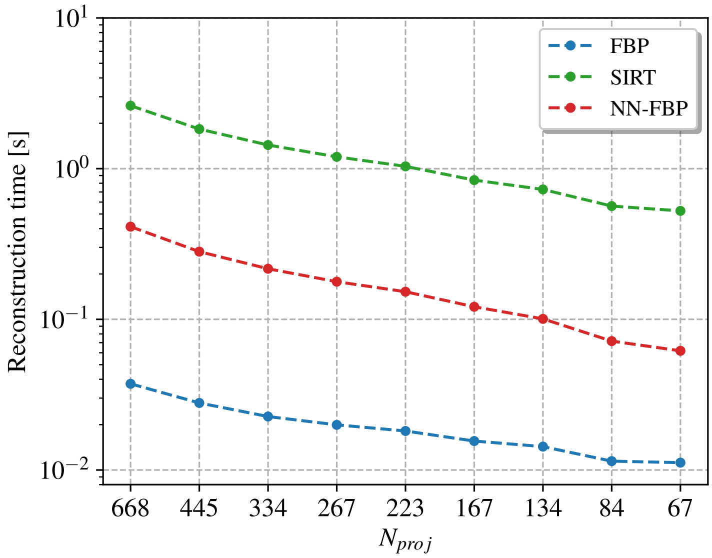

Figure 4.9: The average reconstruction time per slice of the FBP, SIRT and NN-FBP method as a function of the number of projections. All reconstructions were performed on GPU.

N_{proj}	$N_h = 1$	$N_h = 4$	$N_h = 16$
668	155 s	358 s	898 s
445	150 s	260 s	555 s
334	71 s	187 s	594 s
267	136 s	451 s	656 s
223	97 s	307 s	551 s
167	95 s	384 s	420 s
134	90 s	321 s	1209 s
84	100 s	317 s	915 s
67	94 s	402 s	857 s

Table 4.1: Training time of the NN-FBP method as a function of the number of projections and for different number of hidden nodes.

number of projections. In general, the training task requires tens of minutes which is a reasonable time with respect to the acquisition time of a tomographic scan.

4.4 Discussion

We have studied for the first time the performance of the NN-FBP method with neutron data and compared to conventional reconstruction algorithms used in NT in terms of different image quality metrics. We demonstrate that NN-FBP method outperforms the FBP and SIRT with respect to image quality. Furthermore, the computation complexity of NN-FBP method is lower than SIRT. Hence, NN-FBP method provides reconstructions in shorter times with respect to iterative methods. We conclude that the NN-FBP can reliably reduce scan time, reconstruction time and data storage providing high image quality for sparse-view NT. Specific prior knowledge is not explicitly moulded in the NN-FBP method, as opposed to advanced iterative reconstruction algorithms. In fact the method learns the features of the training images by tuning the neural network's weights appropriately. Hence the NN-FBP method can be implemented with high computational efficiency at neutron imaging facilities for the broader applicability than regularized iterative reconstruction algorithms.

The main requirement of the NN-FBP method is that the scanned objects should consist only of the same materials present in the training samples. When this prerequisite is satisfied the NN-FBP method is able to reconstruct accurately objects with different shape and size of the training samples [40].

Our experimental study demonstrates that using the NN-FBP method, the number of projections can be reduced to 1/3 of the projections required by the sampling theorem, ensuring image quality comparable to standard FBP reconstruction. Hence, the acquisition time can be reduced to 1/3 of the time requested by a standard CT scan. However, the reconstruction quality of the NN-FBP is highly dependent on the quality of the projections and reconstructed images used in the training stage. In principle, better results can be obtained by optimizing the imaging setup to increase the signal-to-noise ratio of neutron projections.

4.5 Outlooks

In this study, we focused on the application of the NN-FBP method to sparse-view CT reconstruction of objects similar to a training sample, which was scanned over a large number of view angles. The NN-FBP was trained on the SIRT reconstruction of the over-sampled training dataset. However, several experimental situations limit the angles for which projection data can be acquired. The NN-FBP method can be used in these cases to emulate an advanced but slow regularized iterative method to produce reconstructions from limited projection data. In particular, this can be of great interest for spatio-temporal reconstruction of dynamic systems. For example, the NN-FBP method could be used to study the dynamics of slow periodic phenomena with stroboscopic and acquiring projections according to a Golden ratio based sequence [41]. The training should be performed on high-quality reconstruction of the system at particular time instant. The temporal evolution can be reconstructed with NN-FBP if the aforementioned prerequisite is satisfied during the experiment. However the feasibility of these applications in NT remains subject of further research.

The NN-FBP can be used to reconstruct also *truncated data*, occurring when the scanned object is larger than the field-of-view (FOV) of the imaging system. Truncated sinograms can lead to strong artifacts in the reconstructed images. When using the FBP method with truncated data, the artifacts can be reduced by replicating the projection boundary values to form a larger virtual detector [42]. This method cannot be applied to iterative algorithms, which require projections of the entire sample. Conversely, the padding approach can be used with the NN-FBP method since it is based on FBP reconstructions with custom filters.

We think that the NN-FBP could be improved by using deeper networks with the aim of learning more features of the sample. Deep learning and machine learning in general are promising and innovative approaches for image reconstruction. This field of research nowadays is of interest in medical and X-ray imaging [43], but we think that also NI community should take into account new ML based reconstruction theories and techniques.

References

[1] Wei Yu, Chengxiang Wang, Xiaoying Nie, Min Huang, and Limin Wu. "Image Reconstruction for Few-view Computed Tomography Based on ℓ_0 Sparse Regularization". In: *Procedia Computer Science* 107 (2017). Advances in Information and Communication Technology: Proceedings of 7th International Congress of Information and Communication Technology (ICICT2017), pp. 808–813. ISSN: 1877-0509. DOI: 10.1016/j.procs.2017.03.178.

[2] Muhammad Abir, Fahima Islam, Daniel Wachs, and Hyoung-Koo Lee. "Sparse-view neutron CT reconstruction of irradiated fuel assembly using total variation minimization with Poisson statistics". In: *Journal of Radioanalytical and Nuclear Chemistry* 307.3 (Mar. 2016), pp. 1967–1979. ISSN: 1588-2780. DOI: 10.1007/s10967-015-4542-2.

[3] Yan Liu, Jianhua Ma, Yi Fan, and Zhengrong Liang. "Adaptive-weighted total variation minimization for sparse data toward low-dose x-ray computed tomography image reconstruction". In: *Physics in Medicine & Biology* 57.23 (2012), p. 7923.

[4] Y. Liu, Z. Liang, J. Ma, H. Lu, K. Wang, H. Zhang, and W. Moore. "Total Variation-Stokes Strategy for Sparse-View X-ray CT Image Reconstruction". In: *IEEE Transactions on Medical Imaging* 33.3 (Mar. 2014), pp. 749–763. ISSN: 0278-0062. DOI: 10.1109/TMI.2013.2295738.

[5] Xiao Han, Junguo Bian, Erik L Ritman, Emil Y Sidky, and Xiaochuan Pan. "Optimization-based reconstruction of sparse images from few-view projections". In: *Physics in Medicine & Biology* 57.16 (2012), p. 5245.

[6] Yann Lecun, Yoshua Bengio, and Geoffrey Hinton. "Deep learning". In: *Nature* 521.7553 (2015), pp. 436–444. ISSN: 14764687. DOI: 10.1038/nature14539.

[7] Alex Krizhevsky, Ilya Sutskever, and Geoffrey E Hinton. "ImageNet Classification with Deep Convolutional Neural Networks". In: *Advances in Neural Information Processing Systems 25*. Ed. by F. Pereira, C. J. C. Burges, L. Bottou, and K. Q. Weinberger. Curran Associates, Inc., 2012, pp. 1097–1105.

[8] C. Szegedy, Wei Liu, Yangqing Jia, P. Sermanet, S. Reed, D. Anguelov, D. Erhan, V. Vanhoucke, and A. Rabinovich. "Going deeper with convolutions". In: *2015 IEEE Conference on Computer Vision and Pattern Recognition (CVPR)*. June 2015, pp. 1–9. DOI: 10.1109/CVPR.2015.7298594.

[9] Olga Russakovsky, Jia Deng, Hao Su, Jonathan Krause, Sanjeev Satheesh, Sean Ma, Zhiheng Huang, Andrej Karpathy, Aditya Khosla, Michael Bernstein, Alexander C. Berg, and Li Fei-Fei. "ImageNet Large Scale Visual Recognition Challenge". In: *International Journal of Computer Vision (IJCV)* 115.3 (2015), pp. 211–252. DOI: 10.1007/s11263-015-0816-y.

[10] Yanming Guo, Yu Liu, Theodoros Georgiou, and Michael S. Lew. "A review of semantic segmentation using deep neural networks". In: *International Journal of Multimedia Information Retrieval* 7.2 (June 2018), pp. 87–93. ISSN: 2192-662X. DOI: 10.1007/s13735-017-0141-z.

[11] J. Long, E. Shelhamer, and T. Darrell. "Fully convolutional networks for semantic segmentation". In: *2015 IEEE Conference on Computer Vision and Pattern Recognition (CVPR)*. June 2015, pp. 3431–3440. DOI: 10.1109/CVPR.2015.7298965.

[12] Olaf Ronneberger, Philipp Fischer, and Thomas Brox. "U-Net: Convolutional Networks for Biomedical Image Segmentation". In: *Medical Image Computing and Computer-Assisted Intervention – MICCAI 2015*. Ed. by Nassir Navab, Joachim Hornegger, William M. Wells, and Alejandro F. Frangi. Cham: Springer International Publishing, 2015, pp. 234–241. ISBN: 978-3-319-24574-4.

[13] Michał Koziarski and Bogusław Cyganek. "Deep Neural Image Denoising". In: *Computer Vision and Graphics*. Ed. by Leszek J. Chmielewski, Amitava Datta, Ryszard Kozera, and Konrad Wojciechowski. Cham: Springer International Publishing, 2016, pp. 163–173. ISBN: 978-3-319-46418-3.

[14] Junyuan Xie, Linli Xu, and Enhong Chen. "Image Denoising and Inpainting with Deep Neural Networks". In: *Advances in Neural Information Processing Systems 25*. Ed. by F. Pereira, C. J. C. Burges, L. Bottou, and K. Q. Weinberger. Curran Associates, Inc., 2012, pp. 341–349.

[15] H. C. Burger, C. J. Schuler, and S. Harmeling. "Image denoising: Can plain neural networks compete with BM3D?" In: *2012 IEEE Conference on Computer Vision and Pattern Recognition*. June 2012, pp. 2392–2399. DOI: 10.1109/CVPR.2012.6247952.

[16] Li Xu, Jimmy SJ Ren, Ce Liu, and Jiaya Jia. “Deep Convolutional Neural Network for Image Deconvolution”. In: *Advances in Neural Information Processing Systems 27.* Ed. by Z. Ghahramani, M. Welling, C. Cortes, N. D. Lawrence, and K. Q. Weinberger. Curran Associates, Inc., 2014, pp. 1790–1798.

[17] Jun Guo and Hongyang Chao. “Building Dual-Domain Representations for Compression Artifacts Reduction”. In: *Computer Vision – ECCV 2016.* Ed. by Bastian Leibe, Jiri Matas, Nicu Sebe, and Max Welling. Cham: Springer International Publishing, 2016, pp. 628–644. ISBN: 978-3-319-46448-0.

[18] Chao Dong, Yubin Deng, Chen Change Loy, and Xiaoou Tang. “Compression Artifacts Reduction by a Deep Convolutional Network”. In: *The IEEE International Conference on Computer Vision (ICCV).* Dec. 2015.

[19] Hu Chen, Yi Zhang, Weihua Zhang, Peixi Liao, Ke Li, Jiliu Zhou, and Ge Wang. “Low-dose CT via convolutional neural network”. In: *Biomed. Opt. Express* 8.2 (Feb. 2017), pp. 679–694. DOI: 10.1364/BOE.8.000679.

[20] Xiaogang Yang, Vincent De Andrade, William Scullin, Eva L. Dyer, Narayanan Kasthuri, Francesco De Carlo, and Doga Gursoy. “Low-dose x-ray tomography through a deep convolutional neural network”. In: *Scientific Reports* 8.1 (Feb. 2018). DOI: 10.1038/s41598-018-19426-7.

[21] *Sparse-view CT reconstruction with improved GoogLeNet.* Vol. 10578. 2018, pp. 10578 - 10578 - 7. DOI: 10.1117/12.2295345.

[22] H. Gupta, K. H. Jin, H. Q. Nguyen, M. T. McCann, and M. Unser. “CNN-Based Projected Gradient Descent for Consistent CT Image Reconstruction”. In: *IEEE Transactions on Medical Imaging* 37.6 (June 2018). ISSN: 0278-0062. DOI: 10.1109/TMI.2018.2832656.

[23] K. H. Jin, M. T. McCann, E. Froustey, and M. Unser. “Deep Convolutional Neural Network for Inverse Problems in Imaging”. In: *IEEE Transactions on Image Processing* 26.9 (Sept. 2017), pp. 4509–4522. ISSN: 1057-7149. DOI: 10.1109/TIP.2017.2713099.

[24] Kerstin Hammernik, Tobias Würfl, Thomas Pock, and Andreas Maier. “A Deep Learning Architecture for Limited-Angle Computed Tomography Reconstruction”. In: *Bildverarbeitung für die Medizin 2017.* Ed. by Klaus Hermann Maier-Hein geb. Fritzsche, Thomas Martin Deserno geb. Lehmann, Heinz Handels, and Thomas Tolxdorff. Berlin, Heidelberg: Springer Berlin Heidelberg, 2017, pp. 92–97.

[25] T. Würfl, M. Hoffmann, V. Christlein, K. Breininger, Y. Huang, M. Unberath, and A. K. Maier. “Deep Learning Computed Tomography: Learning Projection-Domain Weights From Image Domain in Limited Angle Problems”. In: *IEEE Transactions on Medical Imaging* 37.6 (June 2018), pp. 1454–1463. ISSN: 0278-0062.

[26] J. Adler and O. Öktem. “Learned Primal-Dual Reconstruction”. In: *IEEE Transactions on Medical Imaging* 37.6 (June 2018), pp. 1322–1332. ISSN: 0278-0062. DOI: 10.1109/TMI.2018.2799231.

[27] D. M. Pelt and K. J. Batenburg. “Fast Tomographic Reconstruction From Limited Data Using Artificial Neural Networks”. In: *IEEE Transactions on Image Processing* 22.12 (Dec. 2013), pp. 5238–5251. ISSN: 1057-7149. DOI: 10.1109/TIP.2013.2283142.

[28] O. Motojima. “The ITER project construction status”. In: *Nuclear Fusion* 55.10 (2015), p. 104023. DOI: 10.1088/0029-5515/55/10/104023.

[29] Ll. M. Evans, T. Minniti, M. Fursdon, M. Gorley, T. Barrett, F. Domptail, E. Surrey, W. Kockelmann, A. v. Müller, F. Escourbiac, and A. Durocher. “Comparison of X-ray and neutron tomographic imaging to qualify manufacturing of a fusion divertor tungsten monoblock”. In: *Fusion Engineering and Design* 134 (2018), pp. 97–108. ISSN: 0920-3796. DOI: 10.1016/j.fusengdes.2018.06.017.

[30] Peter Gilbert. "Iterative methods for the three-dimensional reconstruction of an object from projections". In: *Journal of Theoretical Biology* 36.1 (1972), pp. 105–117. ISSN: 0022-5193. DOI: 10.1016/0022-5193(72)90180-4.

[31] Simon Haykin. *Neural Networks: A Comprehensive Foundation*. 1st. Prentice Hall PTR, 1994. ISBN: 0023527617.

[32] T. Minniti, W. Kockelmann, G. Burca, J.F. Kelleher, S. Kabra, S.Y. Zhang, D.E. Pooley, E.M. Schooneveld, Q. Mutamba, J. Sykora, N.J. Rhodes, F.M. Pouzols, J.B. Nightingale, F. Aliotta, L.M. Bonaccorsi, R. Ponterio, G. Salvato, S. Trusso, C. Vasi, A.S. Tremsin, and G. Gorini. "Materials analysis opportunities on the new neutron imaging facility IMAT@ISIS". In: *Journal of Instrumentation* 11.03 (2016), p. C03014. DOI: 10.1088/1748-0221/11/03/C03014.

[33] Triestino Minniti, Kenichi Watanabe, Genoveva Burca, Daniel E. Pooley, and Winfried Kockelmann. "Characterization of the new neutron imaging and materials science facility IMAT". In: *Nuclear Instruments and Methods in Physics Research Section A: Accelerators, Spectrometers, Detectors and Associated Equipment* 888 (2018), pp. 184–195. ISSN: 0168-9002. DOI: 10.1016/j.nima.2018.01.037.

[34] Winfried Kockelmann, Triestino Minniti, Daniel E. Pooley, Genoveva Burca, Ranggi Ramadhan, Freddie A. Akeroyd, Gareth D. Howells, Chris Moreton-Smith, David P. Keymer, Joe Kelleher, Saurabh Kabra, Tung Lik Lee, Ralf Ziesche, Anthony Reid, Giuseppe Vitucci, Giuseppe Gorini, Davide Micieli, Raffaele G. Agostino, Vincenzo Formoso, Francesco Aliotta, Rosa Ponterio, Sebastiano Trusso, Gabriele Salvato, Cirino Vasi, Francesco Grazzi, Kenichi Watanabe, Jason W. L. Lee, Anton S. Tremsin, Jason B. McPhate, Daniel Nixon, Nick Draper, William Halcrow, and Jim Nightingale. "Time-of-Flight Neutron Imaging on IMAT@ISIS: A New User Facility for Materials Science". In: *Journal of Imaging* 4.3 (2018). ISSN: 2313-433X. DOI: 10.3390/jimaging4030047.

[35] B. Münch, P. Trtik, F. Marone, and M. Stampanoni. "Stripe and ring artifact removal with combined wavelet-Fourier filtering". In: *Optics Express* 17.10 (2009), p. 8567. ISSN: 1094-4087. DOI: 10.1364/OE.17.008567.

[36] Zhou Wang, A. C. Bovik, H. R. Sheikh, and E. P. Simoncelli. "Image quality assessment: from error visibility to structural similarity". In: *IEEE Transactions on Image Processing* 13.4 (Apr. 2004), pp. 600–612. ISSN: 1057-7149. DOI: 10.1109/TIP.2003.819861.

[37] L. Zhang, L. Zhang, X. Mou, and D. Zhang. "FSIM: A Feature Similarity Index for Image Quality Assessment". In: *IEEE Transactions on Image Processing* 20.8 (Aug. 2011), pp. 2378–2386. ISSN: 1057-7149. DOI: 10.1109/TIP.2011.2109730.

[38] W. Xue, L. Zhang, X. Mou, and A. C. Bovik. "Gradient Magnitude Similarity Deviation: A Highly Efficient Perceptual Image Quality Index". In: *IEEE Transactions on Image Processing* 23.2 (Feb. 2014), pp. 684–695. ISSN: 1057-7149. DOI: 10.1109/TIP.2013.2293423.

[39] N. Otsu. "A Threshold Selection Method from Gray-Level Histograms". In: *IEEE Transactions on Systems, Man, and Cybernetics* 9.1 (Jan. 1979), pp. 62–66. ISSN: 0018-9472. DOI: 10.1109/TSMC.1979.4310076.

[40] Eva Bladt, Daniël M. Pelt, Sara Bals, and Kees Joost Batenburg. "Electron tomography based on highly limited data using a neural network reconstruction technique". In: *Ultramicroscopy* 158 (2015), pp. 81–88. ISSN: 0304-3991. DOI: 10.1016/j.ultramic.2015.07.001.

[41] Pavel Trtik Anders P. Kaestner Beat Munch. "Spatiotemporal computed tomography of dynamic processes". In: *Optical Engineering* 50 (2011), pp. 50 - 50 - 10. DOI: 10.1117/1.3660298.

[42] A. Kyrieleis, V. Titarenko, M. Ibison, T. Connolley, and P.J. Withers. “Region-of-interest tomography using filtered backprojection: assessing the practical limits”. In: *Journal of Microscopy* 241.1 (2010), pp. 69–82. DOI: 10.1111/j.1365-2818.2010.03408.x.

[43] G. Wang. “A Perspective on Deep Imaging”. In: *IEEE Access* 4 (2016), pp. 8914–8924. DOI: 10.1109/ACCESS.2016.2624938.

Computer science is not as old as physics; it lags by a couple of hundred years. However, this does not mean that there is significantly less on the computer scientist's plate than on the physicist's: younger it may be, but it has had a far more intense upbringing!

— Richard P. Feynman

Computers themselves, and software yet to be developed, will revolutionize the way we learn.

— Steve Jobs

5 NeuTomPy, a new Python package for CT reconstruction

Contents

This chapter is based on:

D. Micieli, T. Minniti and G. Gorini. "NeuTomPy Toolbox, a Python package for tomographic data processing and reconstruction". In: *SoftwareX* 9 (Mar. 2019), pp. 260-264. DOI: 10.1016/j.softx.2019.01.005.

5.1 Introduction and motivation

Neutron Tomography (NT) has become a routine method for users at many neutron sources to non-destructively investigate the inner structure of a wide range of objects. The commercial software Octopus [1] by Inside Matters is a well established tool for reconstruction of tomographic data at neutron imaging beamlines. However, this software requires a significant investment and generally users can perform a preliminary data processing with Octopus only at the imaging facility. Data analysis is a crucial step for the output of an experiment, so users usually spend time to optimize the data processing mainly at home. This poses a strong demand of freeware and powerful tools to perform data processing of neutron data.

Image acquisition in NT is very time-consuming with respect to X-ray Computed Tomography (CT) and, in several cases, under-sampled datasets are acquired to reduce the scan time and optimize beamtime usage during an experiment. The Filtered Back Projection (FBP) algorithm is regarded as a standard reconstruction method for neutron data. However, as we have already discussed in the previous chapters, FBP generates reconstructed images affected by aliasing artifacts when the number of projections does not satisfy the Nyquist-Shannon condition (Eq. 1.43) [2]. In addition, the image quality of FBP reconstructions highly depends on the amount of noise in projection data. Iterative reconstruction methods outperform FBP, and more generally analytical methods, to handle under-sampled or noisy datasets [3]. Octopus software provides only two reconstruction methods: the FBP and the Simultaneous Algebraic Reconstruction Technique (SART). Modern reconstruction methods are not implemented. On the other hand, several open source tools for tomographic reconstruction are available nowadays but they are mainly developed for X-ray CT and they are not ready to handle neutron data. Some image pre-processing algorithms are mandatory in NT to obtain accurate reconstruction, i.e. the estimation of the rotation axis tilt and the related registration of the projections, the suppression of gamma-spots and the data normalization with respect to the radiation dose. Reconstruction tools for X-ray CT generally include some, but not all of such correction algorithms. For

Figure 5.1: The NeuTomPy logo.

example, the ASTRA toolbox [4] is a Matlab and Python package that provides highly efficient implementation of iterative methods for CPUs and GPUs. ASTRA toolbox is only focused on the reconstruction step and it does not include any pre-processing, post-processing algorithms or functions to read and write data. On the other hand, the Python package TomoPy [5] includes several pre-processing and post-processing algorithms and provides implementation for CPUs of a wide range of iterative reconstruction methods. Moreover TomoPy is not ready to handle neutron data, since it does not include functions to estimate the rotation axis tilt and to compute the related correction on projection data. Furthermore, TomoPy is available only for Linux and Mac OS operating systems. MuhRec [6] is the only free software that was conceived for NT. It includes several filters and pre-processing algorithms and it is currently the main free alternative to Octopus for data processing of neutron data. However, at time of writing, MuhRec does not provide any iterative reconstruction method support.

In this chapter we present the NeuTomPy Toolbox, a new Python package for tomographic data processing, that is specifically designed to compensate the shortcomings of the aforementioned software tools. The NeuTomPy toolbox was conceived primarily for NT and developed to support the need of users and researchers to compare state-of-the-art reconstruction methods and choose the optimal data processing workflow for their data. The toolbox has a modular design, multi-threading capabilities and it supports Windows, Linux and Mac OS operating systems. The NeuTomPy toolbox (logo shown in Figure 5.1) is open source and it is released under the GNU General Public License v3, allowing users to freely use it and encouraging researchers and developers to contribute. Previously, this package has been developed and used for data analysis of the comparative study described in Chapter 3 and Chapter 4 and now is freely distributed to the neutron imaging community.

5.2 Software description

Here we describe the architecture of NeuTomPy Toolbox and present its main functionalities.

5.2.1 Software Architecture

The NeuTomPy toolbox is written in Python. We chose this programming language because it is open-source, cross-platform, human-readable and allows researchers to use and contribute to it easily. The toolbox is divided into several sub-modules, each of these represents a particular phase of a typical CT reconstruction pipeline. The entire chain is represented in Figure 5.2. The NeuTomPy toolbox exploits several Python libraries for scientific computing and image processing, i.e. NumPy [7], NumExpr [8], SciPy [9], scikit-image [10], OpenCV [11] and SimpleITK [12]. In particular, the CT reconstruction step is powered by the ASTRA Toolbox. NeuTomPy combined with ITK-SNAP [13], tomviz [14] or 3D Slicer [15] turns out to be a complete open-source software suite for CT.

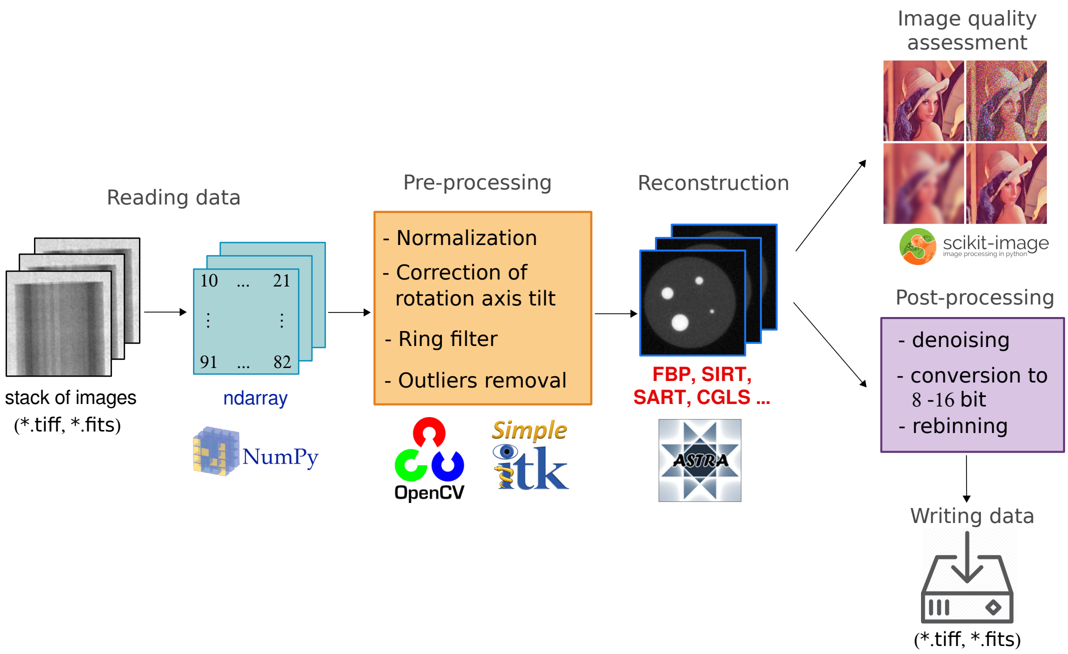

Figure 5.2: Diagram representing the typical CT data processing steps that can be performed by NeuTomPy toolbox. The package has a modular structure that follows the data processing chain.

Specifications	Octopus	MuhRec	NeuTomPy
Operating systems	Windows	Windows, Mac OS Linux	Windows, Mac OS, Linux
Reconstruction algorithms	FBP, SART	FBP	FBP, ART, SART, SIRT, CGLS, NN-FBP, MR-FBP
GPU-based reconstruction	Yes	No	Yes
Image Quality Assessment	No	No	Yes
GUI	Yes	Yes	No
Batch Processing	No	Yes	Yes
License	Proprietary	GPLv3	GPLv3

Table 5.1: Comparative table between Octopus, MuhRec (the leading reconstruction software for NT) and NeuTomPy toolbox.

In Table 5.1 we show a comparison between the leading reconstruction software for NT, i.e. Octopus and MuhRec, and NeuTomPy Toolbox. It is worth noting that at time of writing our software has no a global GUI, but some functions enable user interactions via graphic interface.

The documentation of each NeuTomPy's function and several example scripts are available on ReadtheDocs website[1]. The source code is available on a GitHub repository[2].

5.2.2 Installation

NeuTomPy toolbox supports Windows, Linux and Mac OS operating systems. It is recommended to use a Conda[3] environment with Python 3.5 or 3.6 and install the following dependencies:

```
$ conda install -c simpleitk simpleitk
$ conda install -c astra-toolbox astra-toolbox
$ conda install -c conda-forge numexpr matplotlib astropy tifffile
                   opencv scikit-image read-roi tqdm pywavelets
```

then NeuTomPy toolbox can be installed via `pip`:

```
$ pip install neutompy
```

[1] https://neutompy-toolbox.readthedocs.io
[2] https://github.com/dmici/NeuTomPy-toolbox
[3] https://www.anaconda.com/download

5.2.3 Main functionalities and code snippets

The NeuTomPy toolbox allows to perform the steps of a typical CT reconstruction workflow (Figure 5.2). The first task is represented by the reading of a raw dataset. The implemented reader handles TIFF and FITS files and converts a stack of images into a numpy array. A dataset containing raw projections, dark-field, flat-field images and the projection at 180° can be read by:

```
import neutompy as ntp
proj,dark,flat,proj_180 = ntp.read_dataset(proj_180=True)
```

hence the user can select the data to read from a dialog box. Subsequently, the projection data must be normalized with respect to dark-field and flat-field images to compute the transmission images. If the source intensity is not stable the images can be normalized with respect to the radiation dose [3]. In this case, the user must specify a region of interest (ROI) which corresponds to a background area not covered by the specimen in all the projections (we called it the dose ROI). It can be specified in three different ways: drawing interactively a rectangular selection, specifying the ROI' s coordinates or reading an ImageJ .roi file. For example, to normalize data and select interactively the dose ROI, the Python instruction is:

```
norm, norm_180 = ntp.normalize_proj(proj,dark,flat,proj_180=proj_180,
                                    dose_draw=True)
```

where the function `normalize_proj` returns a 3D array containing the stack of normalized projections (`norm`) and a 2D array representing the normalized radiograph at 180° (`norm_180`).

A common experimental issue in NT is the misalignment of the rotation axis with respect to the vertical axis of the detector. The function `correction_COR` evaluates the horizontal offset and the tilt angle by minimizing the squared error between two opposite radiographs computed at different vertical positions, as described in [6], and finally it registers all the projections. The Python instruction for this task is:

```
norm = ntp.correction_COR(norm, proj_0, proj_180)
```

where `proj_0` and `proj_180` are the projections (raw or normalized) at 0° and 180°, respectively. The user selects interactively different ROIs where the sample is visible.

Subsequently the results and some information about the evaluation of the rotation axis are shown. We report in Figure 5.3 an example for the rotation axis correction: the difference of the projections at 0° (P_0) and the mirrored projection at 180° ($P_\pi^{flipped}$) before and after the correction are shown in the left and right side, respectively.

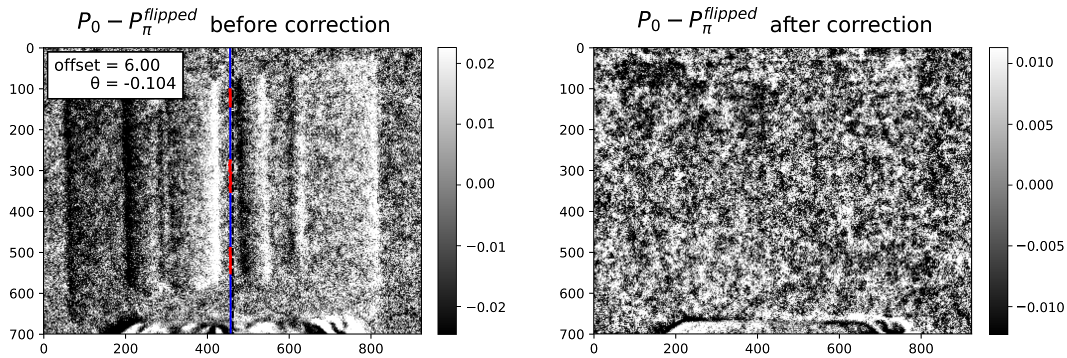

Figure 5.3: Results of the rotation axis correction: the difference $P_0 - P_\pi^{flipped}$ before (left) and after (right) the correction. The rotation axis is determined correctly if the difference image $P_0 - P_\pi^{flipped}$ after correction does not contain sample features.

The NeuTomPy toolbox includes an outlier removal which replaces a pixel value by the median of the neighbourhood pixels if it deviates from the median by more than a certain value. This threshold value can be specified by the user as a global value or proportional to the local standard deviation. It is provided also a de-striping filter, based on combined wavelet and Fourier analysis, to suppress the ring artifacts [16].

The reconstruction module includes all CPU- and GPU-based algorithms for 2D parallel beam geometry implemented in the ASTRA toolbox and some additional reconstruction methods distributed as ASTRA plugins. The available algorithms are summarized in Table 5.2.

method	CPU	GPU
BP [2]	x	x
FBP [2]	x	x
ART [2]	x	
SART [2]	x	x
CGLS [17]	x	x
SIRT [18]	x	x
NN-FBP [19]	x	x
MR-FBP [20]	x	x

Table 5.2: List of the CT reconstruction methods included in NeuTomPy Toolbox for two-dimensional parallel-beam geometries.

The instruction to perform a CT reconstruction is the following:

```
rec = ntp.reconstruct(norm,angles,method,parameters)
```

where `rec` is the reconstructed volume, `angles` is one-dimensional array containing the view angles in radians, `method` is a string which indicates the algorithm to use and `parameters` is a Python dictionary that contains specific settings of the reconstruction algorithm. The allowed values for `method` and `parameters` follow the convention of the ASTRA toolbox, reported in the documentation [21]. For example, the following instruction is used to compute with GPU support a FBP reconstruction with the Hamming filter:

```
rec = ntp.reconstruct(norm,angles,method="FBP_CUDA",
                      parameters={"FilterType":"hamming"})
```

while a SIRT reconstruction with 100 iterations and pixel values limited in the range [0, 2] can be performed by:

```
rec = ntp.reconstruct(norm,angles,method="SIRT_CUDA",
                      parameters={"iterations":100,"MinConstraint":0.0,
                                  "MaxConstraint"=2.0})
```

In addition, the NeuTomPy toolbox allows to compare and evaluate the performance of different reconstruction algorithms in terms of several image quality indexes. The metrics implemented are the Contrast-to-Noise-Ratio (CNR) [3], the Normalized Root Mean Square Error (NRMSE) [3], an edge quality metric [3], the Structural Similarity Index (SSIM) [22] and the Gradient Magnitude Similarity Deviation (GMSD) [23].

5.3 Illustrative Examples

In this section we show some examples of data processing and reconstruction using NeuTomPy toolbox. Firstly, we give in Code 5.1 an example of a full CT processing workflow which includes data reading, normalization, COR registration, outliers and ring removals, SIRT reconstruction with GPU support and finally the data writing. It is worth noting that with about ten lines of code a full CT processing workflow is performed.

Code 5.1: A complete SIRT reconstruction workflow.

```
# -------------------------------------------------------------------
# This script performs a complete reconstruction workflow.
# The reconstruction algorithm used is the SIRT performed on a GPU.
# -------------------------------------------------------------------
import numpy as np
import neutompy as ntp
# set pixel size in cm
pixel_size  = 0.0029
# set the last angle value of the CT scan: np.pi or 2*np.pi
last_angle = 2*np.pi
# read dataset containing projection, dark-field, flat-field images and
# the projection at 180 degree
proj, dark, flat, proj_180 = ntp.read_dataset()
# normalize the projections to dark-field, flat-field images and
# neutron dose
norm, norm_180 = ntp.normalize_proj(proj, dark, flat,proj_180=proj_180,
                                    dose_draw=True, crop_draw=True)
# rotation axis tilt correction
norm = ntp.correction_COR(norm, norm[0], norm_180)
# clean up memory
del dark; del flat; del proj; del proj_180
# remove outliers, set the optimal radius and threshold
norm = ntp.remove_outliers_stack(norm, radius=1, threshold=0.018,
                                 outliers='dark', out=norm)
norm = ntp.remove_outliers_stack(norm, radius=3, threshold=0.018,
                                 outliers='bright', out=norm)
# perform minus-log transform
norm = ntp.log_transform(norm, out=norm)
# remove stripes in sinograms
norm = ntp.remove_stripe_stack(norm, level=4, wname='db30', sigma=1.5,
                               out=norm)
# define the array of the angle views in radians
angles = np.linspace(0, last_angle, norm.shape[0], endpoint=False)
# SIRT reconstruction with 100 iterations using GPU
print('> Reconstruction...')
rec = ntp.reconstruct(norm, angles, 'SIRT_CUDA',
                parameters={"iterations":100},pixel_size=pixel_size)
# select the directory and the prefix file name of the reconstructed
# images to save.
recon_dir = ntp.save_filename_gui('', message = 'Select the folder and
   the prefix name for the reconstructed images...')
# write the reconstructed images to disk
ntp.write_tiff_stack(recon_dir, rec)
```

The NeuTomPy toolbox includes some reconstruction methods distributed as ASTRA plugins. Hence, we illustrate an usage example of the NN-FBP method [19], which was discussed in Chapter 4 for the application to NT. The Code 5.2 performs a FBP reconstruction of a complete dataset and then trains the NN-FBP to reconstruct some slices using less projections. Finally, the trained NN-FBP reconstructs other slices of the same sample using under-sampled data.

Code 5.2: An usage example of the NN-FBP training and reconstruction.

```
# -----------------------------------------------------------------------
# This script shows an usage example of the NN-FBP method.
# A complete dataset is reconstructed via FBP and the NN-FBP is
# trained to reconstruct some reconstructed slices using a sparse-view
# dataset. Then different slices are reconstructed via NN-FBP.
# -----------------------------------------------------------------------
import numpy as np
import neutompy as ntp
import os

pixel_size  = 0.0029 # set pixel size in cm
hqrec_folder = 'hqrecs/'  # folder to save high quality reconstuction
nnfbp_rec_folder = 'recon-nnfbp/' # output folder of nnfbp recon
conf = {}
# number of hidden nodes
conf['hidden_nodes']  = 3
#high-quality reconstruction
conf['hqrecfiles']=hqrec_folder+'sample*.tiff'
# folder where training files are stored
conf['traindir'] = 'trainfiles/'
# number of random pixels to pick per slice
conf['npick'] = 10000
# file to store trained filters
conf['filter_file'] ='filters.mat'
last_angle = 2*np.pi # last angle of the CT scan: np.pi or 2*np.pi

# read dataset containing projection, dark-field, flat-field images and
# the projection at 180 degree
proj, dark, flat, proj_180 = ntp.read_dataset()
# define the array of the angle views in radians
angles = np.linspace(0, last_angle, proj.shape[0], endpoint=False)

# normalize the projections to dark-field, flat-field images and
# neutron dose
norm, norm_180 = ntp.normalize_proj(proj,dark,flat,proj_180=proj_180,
                            dose_draw=True, crop_draw=True, log=True)

# rotation axis tilt correction
norm = ntp.correction_COR(norm, norm[0], norm_180)

# high-quality reconstruction
train_slice_start = 100
train_slice_end   = 120
rechq = ntp.reconstruct(norm[:,train_slice_start:train_slice_end+1, :],
               angles, 'FBP_CUDA', parameters={"FilterType":"hamming"},
               pixel_size=pixel_size)

# write the high-quality reconstructed images to disk
ntp.write_tiff_stack(hqrec_folder + 'sample', rechq)

# NN-FBP training
# reduction factor of the full dataset to obtain the
# sparse-view dataset
skip  = 3
norm_train = norm[::skip,train_slice_start:train_slice_end+1, :]
ntp.reconstruct(norm_train,angles[::skip],'NN-FBP-train',
                parameters=conf)
```

```
# NN-FBP reconstruction of noisy projections
test_slice_start = 180
test_slice_end   = 200
norm_test = norm[::skip,test_slice_start:test_slice_end+1, :]
rec_nnfbp = ntp.reconstruct(norm_test, angles[::skip], 'NN-FBP',
                            parameters=conf)

# write NN-FBP reconstructed images
ntp.write_tiff_stack(nnfbp_rec_folder + 'sample', rec_nnfbp)
```

Finally, we demonstrate the possibility to perform several reconstruction algorithms and compare them quantitatively using the NeuTomPy toolbox. We used neutron images of the phantom sample already described in Chapter 3. We remind that such phantom is an aluminium cylinder containing four holes of different diameters and filled with iron powder. Neutron images were acquired at the IMAT beamline [24]. We used for CT reconstruction an under-sampled dataset with 1/3 of the number of projections required by the Nyquist-Shannon condition. We performed FBP, SIRT and CGLS reconstructions and we compare them in terms of the image quality indexes NRMSE, SSIM and CNR. We consider the SIRT reconstruction (200 iterations) of a full-view dataset, which is sampled to fulfill the Nyquist-Shannon condition, as the reference image for the computation of the NRMSE and SSIM. The CNR was computed considering a ROI that includes one iron rod and with the second ROI outside the sample. The results are shown in Figure 5.4. It is clear that the two iterative algorithms outperform the FBP method. In fact, the CGLS and the SIRT reconstructions have higher CNR and SSIM, and lower NRMSE than the FBP, which indicate better image quality. In general, the under-sampling and the noise in the projection data cause in the reconstructed images a broadening of the attenuation coefficients distribution. However, unlike FBP reconstruction, the CGLS and the SIRT images are characterized by a bimodal distribution of the grey values, which reflects the composition of the sample. The source code of this analysis is omitted here for brevity. However, the source code for this and other examples can be found in the GitHub repository.

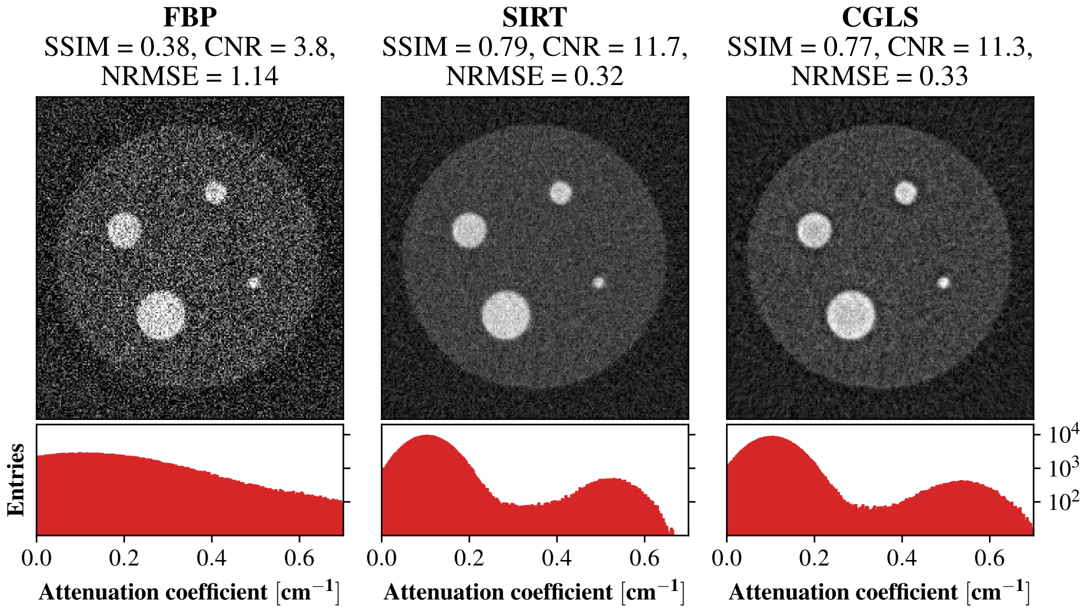

Figure 5.4: A comparison of reconstructed images of a phantom sample, obtained using FBP, SIRT (200 iterations) and CGLS (10 iterations). Below each image the histogram of the attenuation coefficient values within the sample is represented in the range [0, 0.7] cm^{-1}

5.4 Impact

Data processing is the last step of a NT experiment but it is crucial for the interpretation of the results. Advanced image processing algorithms can extract hidden information from data and reduce the tomographic scan time. Hence new software tools, specifically designed for neutron data, are required to compare state-of-the-art image processing algorithms. Working on robust methods and tools to improve image quality means get better output from NT experiments. However, state-of-the-art iterative reconstruction methods are not implemented in Octopus and MuhRec, which are the leading software for NT reconstruction. The NeuTomPy toolbox solves this shortcoming because it is ready to work with neutron data and allows to perform and compare several iterative reconstruction methods. Researchers can define the optimal data processing workflow for their specific problem using the NeuTomPy toolbox. The code is open-source, hence developers and researchers are invited to contribute.

5.5 Conclusions

In this chapter we presented the NeuTomPy Toolbox, a new Python package for tomographic data processing. We demonstrated that the toolbox is ready to work with neutron data and allows researchers to state the optimal data processing workflow for their specific investigation. The first release includes pre-processing algorithms, artifacts removal and a wide range of classical and state-of-the-art reconstruction methods. The NeuTomPy toolbox supports Windows, Linux and Mac OS operating systems and it is released as open source. Researchers can freely use it and contribute to the project.

The future development will involve improvement of pre-processing algorithms (e.g. scattering correction), addition of new reconstruction methods and finally the implementation of a Graphical User Interface (GUI).

References

[1] Inside Matters. *Octopus Imaging Software*. 2018.

[2] A. C. Kak and M. Slaney. *Principles of computerized tomographic imaging*. Society for Industrial and Applied Mathematics, 2001.

[3] D. Micieli, T. Minniti, V. Formoso, W. Kockelmann, and G. Gorini. "A comparative study of reconstruction methods applied to Neutron Tomography". In: *Journal of Instrumentation* 13.06 (2018), p. C06006.

[4] Wim van Aarle, Willem Jan Palenstijn, Jeroen Cant, Eline Janssens, Folkert Bleichrodt, Andrei Dabravolski, Jan De Beenhouwer, K. Joost Batenburg, and Jan Sijbers. "Fast and flexible X-ray tomography using the ASTRA toolbox". In: *Opt. Express* 24.22 (2016), pp. 25129–25147. DOI: 10.1364/OE.24.025129.

[5] Doğa Gürsoy, Francesco De Carlo, Xianghui Xiao, and Chris Jacobsen. "TomoPy: a framework for the analysis of synchrotron tomographic data". In: *Journal of Synchrotron Radiation* 21.5 (Sept. 2014), pp. 1188–1193. DOI: 10.1107/S1600577514013939.

[6] Anders P. Kaestner. "MuhRec—A new tomography reconstructor". In: *Nuclear Instruments and Methods in Physics Research Section A: Accelerators, Spectrometers, Detectors and Associated Equipment* 651.1 (2011), pp. 156–160. ISSN: 0168-9002. DOI: 10.1016/j.nima.2011.01.129.

[7] S. van der Walt, S. C. Colbert, and G. Varoquaux. "The NumPy Array: A Structure for Efficient Numerical Computation". In: *Computing in Science Engineering* 13.2 (Mar. 2011), pp. 22–30. ISSN: 1521-9615. DOI: 10.1109/MCSE.2011.37.

[8] *NumExpr documentation*. 2018. URL: https://numexpr.readthedocs.io/.

[9] Eric Jones, Travis Oliphant, Pearu Peterson, et al. *SciPy: Open source scientific tools for Python*. 2001.

[10] Stéfan van der Walt, Johannes L. Schönberger, Juan Nunez-Iglesias, François Boulogne, Joshua D. Warner, Neil Yager, Emmanuelle Gouillart, and Tony and Yu. "scikit-image: image processing in Python". In: *PeerJ* 2 (June 2014), e453. ISSN: 2167-8359. DOI: 10.7717/peerj.453.

[11] G. Bradski. “The OpenCV Library”. In: *Dr. Dobb’s Journal of Software Tools* (2000).

[12] Ziv Yaniv, Bradley C. Lowekamp, Hans J. Johnson, and Richard Beare. “SimpleITK Image-Analysis Notebooks: a Collaborative Environment for Education and Reproducible Research”. In: *Journal of Digital Imaging* 31.3 (June 2018), pp. 290–303. ISSN: 1618-727X. DOI: 10.1007/s10278-017-0037-8.

[13] Paul A. Yushkevich, Joseph Piven, Heather Cody Hazlett, Rachel Gimpel Smith, Sean Ho, James C. Gee, and Guido Gerig. “User-Guided 3D Active Contour Segmentation of Anatomical Structures: Significantly Improved Efficiency and Reliability”. In: *Neuroimage* 31.3 (2006), pp. 1116–1128.

[14] Barnaby D.A. Levin, Yi Jiang, Elliot Padgett, Shawn Waldon, Cory Quammen, Chris Harris, Utkarsh Ayachit, Marcus Hanwell, Peter Ercius, David A. Muller, and Robert Hovden. “Tutorial on the Visualization of Volumetric Data Using tomviz”. In: *Microscopy Today* 26.1 (Jan. 2018), pp. 12–17. DOI: 10.1017/s1551929517001213.

[15] Andriy Fedorov, Reinhard Beichel, Jayashree Kalpathy-Cramer, Julien Finet, Jean-Christophe Fillion-Robin, Sonia Pujol, Christian Bauer, Dominique Jennings, Fiona Fennessy, Milan Sonka, John Buatti, Stephen Aylward, James V. Miller, Steve Pieper, and Ron Kikinis. “3D Slicer as an image computing platform for the Quantitative Imaging Network”. In: *Magnetic Resonance Imaging* 30.9 (2012), pp. 1323–1341. ISSN: 0730-725X. DOI: 10.1016/j.mri.2012.05.001.

[16] B. Münch, P. Trtik, F. Marone, and M. Stampanoni. “Stripe and ring artifact removal with combined wavelet-Fourier filtering”. In: *Optics Express* 17.10 (2009), p. 8567. ISSN: 1094-4087. DOI: 10.1364/OE.17.008567.

[17] John a. Scales. “Tomographic inversion via the conjugate gradient method”. In: *Geophysics* 52.2 (1987), p. 179. ISSN: 1070485X. DOI: 10.1190/1.1442293.

[18] Peter Gilbert. “Iterative methods for the three-dimensional reconstruction of an object from projections”. In: *Journal of Theoretical Biology* 36.1 (1972), pp. 105–117. ISSN: 0022-5193. DOI: 10.1016/0022-5193(72)90180-4.

[19] D. M. Pelt and K. J. Batenburg. “Fast Tomographic Reconstruction From Limited Data Using Artificial Neural Networks”. In: *IEEE Transactions on Image Processing* 22.12 (Dec. 2013), pp. 5238–5251. ISSN: 1057-7149. DOI: 10.1109/TIP.2013.2283142.

[20] Daniel M. Pelt and Kees Joost Batenburg. “Improving filtered backprojection reconstruction by data-dependent filtering”. In: *IEEE Transactions on Image Processing* 23.11 (2014), pp. 4750–4762. ISSN: 10577149. DOI: 10.1109/TIP.2014.2341971.

[21] *ASTRA toolbox documentation*. 2018. URL: https://www.astra-toolbox.com/docs/algs/index.html.

[22] Zhou Wang, Alan C. Bovik, Hamid R. Sheikh, and Eero P. Simoncelli. “Image Quality Assessment: From Error Visibility to Structural Similarity”. In: *IEEE Transactions on Image Processing* 13.4 (2004), pp. 600–612. DOI: 10.1109/TIP.2003.819861.

[23] Wufeng Xue, Lei Zhang, Xuanqin Mou, and Alan C. Bovik. “Gradient Magnitude Similarity Deviation: A Highly Efficient Perceptual Image Quality Index”. In: *IEEE Transactions on Image Processing* 23.2 (Feb. 2014), pp. 684–695. DOI: 10.1109/tip.2013.2293423.

[24] Triestino Minniti, Kenichi Watanabe, Genoveva Burca, Daniel E. Pooley, and Winfried Kockelmann. “Characterization of the new neutron imaging and materials science facility IMAT”. In: *Nuclear Instruments and Methods in Physics Research Section A: Accelerators, Spectrometers, Detectors and Associated Equipment* 888 (2018), pp. 184–195. ISSN: 0168-9002. DOI: 10.1016/j.nima.2018.01.037.

6
Conclusions

In this thesis, we addressed the problem of scan time reduction in neutron tomography experiments by using sparse-view datasets. We have studied the data processing procedures which allow to reduce the number of radiographs without any loss of the reconstructed image quality. For this purpose, we have developed a free and open source software called `NeuTomPy`, which allows to perform and compare several classical and state-of-the-art reconstruction methods. In what follows, the main conclusions for each chapter are drawn.

In Chapter 1 and Chapter 2 we introduced the tomography and the neutron imaging technique by recalling background arguments supporting this thesis. In particular, we focused our attention on the mathematical formulation of the main reconstruction algorithms and on the features and the main issues related to neutron tomography.

In Chapter 3 the performances of FBP and different algebraic reconstruction methods (SIRT, SART and CGLS) have been tested for neutron data and studied as a function of the number of projections and for different setups of the imaging system. The reconstruction algorithms were quantitatively compared in terms of the reconstructed image quality and computation time. We have observed that algebraic methods provide better contrast detectability than the FBP algorithm in the case of sparse-view datasets. We proved that the CGLS algorithm is the best compromise between spatial resolution, image contrast and reconstruction time. For moderate under-sampled datasets, the CGLS and SIRT algorithms combined with the use of thinner scintillators provided high reconstructed image quality so much that the time of a neutron CT scan could be halved. For higher under-sampled datasets (i.e. with less than 1/9 of the projections required by the Nyquist-Shannon condition), CGLS and SART showed the best performances in terms of reconstructed image quality. The SIRT algorithm provides reconstructions with highest image contrast in general, but at the expense of lower spatial resolution and lower computational efficiency. Conversely, the SART algorithm is the fastest among the algebraic reconstruction methods tested in this work; however, the CGLS method, thanks to its high convergence, provides reconstructions with timing of the same order of magnitude.

In Chapter 4 we proposed the recently introduced NN-FBP method to reduce the acquisition time in NT experiments. At the best of our knowledge, this is the first study which proposes and tests a machine learning based reconstruction method for NT. As a case study, we chose to inspect part of a monoblock from the divertor region of a fusion energy device by means of sparse-view NT. In our work, simulated and real neutron data were used to assess the performance of the NN-FBP, FBP and SIRT methods as a function of the number of projections. The reconstruction algorithms were quantitatively compared in terms of several image quality indexes and computation time. Our experimental study demonstrates that with the use of the NN-FBP method the number of projections can be reduced to 1/3 of the projections required by the sampling theorem, ensuring image quality comparable to standard FBP reconstruction. Hence, the acquisition time can be reduced to 1/3 of the time requested by a standard CT scan. However, the reconstruction quality of the NN-FBP is highly dependent on the quality of the projections and reconstructed images used in the training stage. Hence better results can be obtained by optimizing the imaging setup to increase the signal-to-noise ratio of neutron projections. The NN-FBP method avoids a number of disadvantages of analytical and iterative reconstruction algorithms.

In fact, NN-FBP is faster than iterative methods, since it has similar computation complexity to FBP. In addition, specific prior knowledge is not explicitly moulded in the NN-FBP method, unlike regularized iterative algorithms which need a proper model describing the prior knowledge. Hence the NN-FBP method can be implemented with high computational efficiency at neutron imaging facilities for the broader applicability than regularized iterative reconstruction algorithms.

We think that the NN-FBP could be improved by using deeper neural networks with the aim of learning more features of the sample. Deep learning and machine learning in general are promising and innovative approaches for image reconstruction. We believe that the neutron imaging community should take into account such new techniques.

In Chapter 5 we have presented `NeuTomPy`, a new Python package for tomographic data processing and reconstruction. We showed in detail the architecture, the main functionalities and some usage examples of `NeuTomPy`.

Such toolbox was developed in order to support the demand of users to have free software suitable for neutron datasets, allowing to perform and compare different reconstruction methods. In fact, state-of-the-art iterative reconstruction methods are not implemented in Octopus and MuhRec, which are the leading data processing software for NT. On the other hand, software for X-ray CT generally include several iterative reconstruction methods, but not all correction algorithms required by NT. The `NeuTomPy` toolbox solves this shortcoming because it is ready to work with neutron data and allows to perform and compare several reconstruction methods. Researchers can define the optimal data processing workflow for their specific problem using the `NeuTomPy` toolbox.

The first release includes pre-processing algorithms, a wide range of classical and state-of-the-art reconstruction methods and several image quality indexes, in order to evaluate the reconstruction quality. The toolbox has a modular design, multi-threading capabilities and it supports Windows, Linux and Mac OS operating systems. The code is open-source, hence users can freely use it while developers and researchers are invited to contribute to the project.

The package has been used for data analysis of the comparative studies presented in this thesis and now is freely distributed to the neutron imaging community.

The future development will include improvement of pre-processing algorithms (e.g. scattering correction), addition of new reconstruction methods and finally the implementation of a Graphical User Interface (GUI).